ISBN 978-82-326-4548-0 (printed version)
ISBN 978-82-326-4549-7 (electronic version)
ISSN 1503-8181

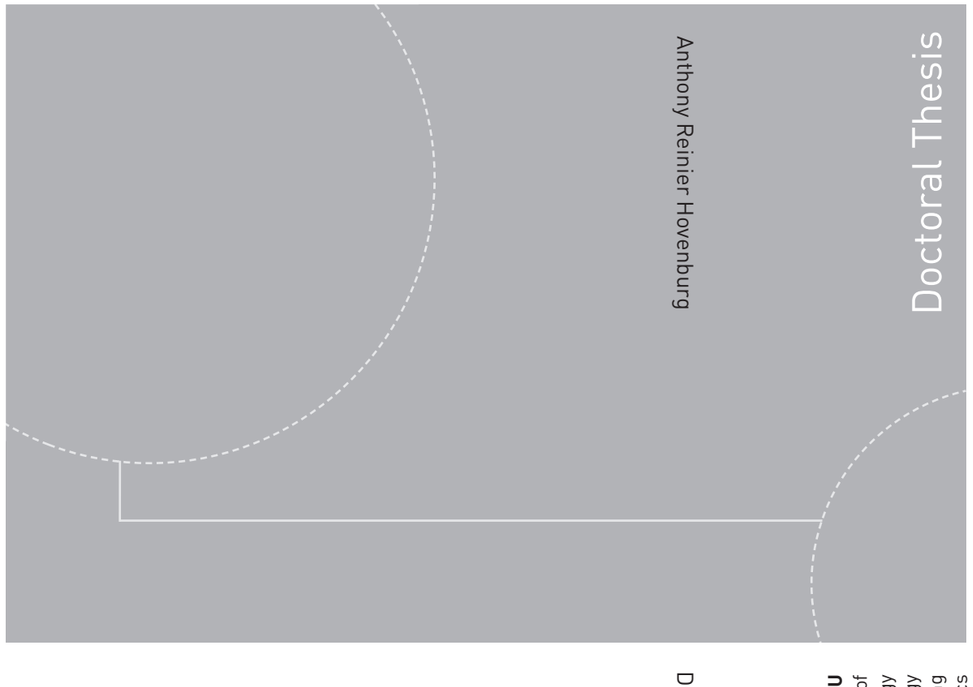

Doctoral theses at NTNU, 2020:98

Anthony Reinier Hovenburg

Flight Performance Optimization for Small Unmanned Aerial Vehicles Using Path Planning Methods

NTNU
Norwegian University of
Science and Technology

NTNU
Norwegian University of
Science and Technology

Doctoral theses at NTNU, 2020:98

NTNU
Norwegian University of
Science and Technology
Faculty of Information Technology
and Electrical Engineering
Department of Engineering Cybernetics

Anthony Reinier Hovenburg

Flight Performance Optimization for Small Unmanned Aerial Vehicles Using Path Planning Methods

Thesis for the degree of Philosophiae Doctor

Trondheim, March 2020

Norwegian University of Science and Technology
Faculty of Information Technology
and Electrical Engineering
Department of Engineering Cybernetics

NTNU
Norwegian University of Science and Technology

Thesis for the degree of Philosophiae Doctor

Faculty of Information Technology
and Electrical Engineering
Department of Engineering Cybernetics

ISBN 978-82-326-4548-0 (printed version)
ISBN 978-82-326-4549-7 (electronic version)
ISSN 1503-8181

Doctoral theses at NTNU, 2020:98

Printed by Skipnes Kommunikasjon as

Voor mijn vader.

Summary

The presented research topics were selectively chosen in an effort to fill specific knowledge gaps within the unmanned aircraft industry. The researcher conducted his work at the company Maritime Robotics, which is a international operator of small unmanned aerial systems.

The overall goal of the work was to provide methods for an increased operational envelope of fixed-wing small unmanned aircraft systems (sUAS), in an attempt to advance the possible applications. In particular by providing the industry with beyond-state-of-the-art methods for optimizing the in-flight performance through intelligent path planning. Recent advancements in unmanned aerial technology have made professional operations accessible to a wider audience, with a variety of mission types. The methods have been applied to several typical unmanned operations, including maximizing the range in A-to-B flights and cooperative Search and Rescue (SAR) missions.

This thesis proposes and demonstrates through simulations methods for integrating relevant aircraft performance models into the path planning algorithms while considering information on en-route meteorological information, such as horizontal winds and potential icing conditions. Similarly, opportunities are demonstrated for increasing the operational safety of small unmanned aircraft through path planning optimization by utilizing redundant propulsion systems. Finally, methods for the performance optimization of cooperative UAS is presented. The paper concludes by providing suggestions for airframe design optimization.

The most important contribution to existing path planning models is the level of integration of fixed-wing aircraft performance models, in conjunction with relevant environmental parameters, such as en-route wind and icing conditions.

Contents

List of figures

List of tables

Preface

This monograph was submitted in partial fulfilment of the degree of Philosophiae Doctor (PhD) of the Department of Engineering Cybernetics of the Norwegian University of Science and Technology (NTNU). The work presented in this thesis has a large industrial component, as the work was carried out as part of an industrial PhD program under the Marie Sklodowska-Curie Actions' support for *Innovative Training Network*, Horizon 2020 initiative, funded by the European Commission (agreement number 642153). The research was conducted at the company Maritime Robotics AS, located in Trondheim, Norway, in colllaboration with the centre for Autonomous Marine Operations and Systems (NTNU AMOS) at the department of Engineering Cybernetics of NTNU. The scientific work was supervised by Professor Rune Storvold (NTNU & NORCE Research Centre) and Professor Tor Arne Johansen (AMOS), while the industrial work was supervised by Vegard Evjen Hovstein & Tørbjørn Houge (Maritime Robotics AS).

Acknowledgments

This thesis signifies an amazing chapter of my life. I imagined Trondheim to be a cold, dark and distant city. Which it is, but only geographically. Because here I met some of the warmest and kindest people I have ever known. For this amazing experience I want to thank my supervisors Tor Arne Johansen and Rune Storvold from NTNU, for their great supervision which made my PhD candidacy so much more enjoyable. Also I would like to thank my former colleagues at Maritime Robotics AS for welcoming me into their company and making me feel at home. Everyone showed great character, for which I am thankful.

The MarineUAS programme was a rich experience, both educationally and emotionally. Here I have met great researchers-in-training, who I wish all the best in their future careers. I also found two good friends in Fabio Andrade and Christopher Dahlin, with who I am sure our journey has just begun.

I want to thank Sunniva for her love and companionship during my candidacy.

Not only did she manage to keep up with my stress and irregular working hours, she also brought our two beautiful children into this world: Andreas and Linde. I was able to get this far in my PhD candidacy only because of her sacrifice. I am grateful, impressed and humbled by her perseverance.

Finally, and most importantly, I want to thank my dear father Reinier B. Hovenburg for always believing in me. My father is, without a doubt, the most important figure in my life. He worked hard, so that I could focus on my education and spend my time on things I liked to do. I know that my father is proud of me. And I am proud of him. My mother Michaela de Paauw has always supported me in whatever choice I made. It was not easy for her when I decided to move to Norway. But as always in her life she sacrificed her happiness for my own, which I will never forget.

Writing an acknowledgement that does justice to all that contributed to my successful stay in Trondheim would be a thesis by itself. Forgive me for those that I have forgotten to mention. Gratitude is in the heart.

Anthony Reinier Hovenburg

Chapter 1

Introduction

1.1 Background and Motivation

Over the last decade small unmanned aerial vehicles (sUAS) have increasingly found their ways into industrial applications. Unmanned aircraft are becoming more capable and more reliable, resulting in a broader search for applications. Reasons for applying professional unmanned aircraft vary, and include supporting jobs that are typically dirty, dull or dangerous, such as surveillance in remote areas or agricultural crop inspections [145]. Additionally, unmanned aircraft offer the potential to cost savings, for example in the case of power-line inspection where sUAS enable rapid inspections and eliminate the need for personnel to climb up hazardous structures [146].

The industry is developing rapidly, while fundamental problems still exist that are yet to be solved. Among these problems is the limited range of battery-powered unmanned aircraft. Current battery-powered propulsion systems have a relatively high power-to-weight ratio compared to traditional internal combustion engines (ICE). This makes it particularly suitable for aerospace applications. Additionally, battery-powered aircraft produce significantly less noise and produce no direct exhaust fumes which are harmful to the local environment [120]. Battery-powered aircraft also offer practical advantages, as the system requires less maintenance [86]. For maritime, off-shore and other fire-critical applications, it is a relevant advantage that such systems do not rely on flammable liquid fuels.

However, current commercial unmanned battery technology, typically Lithium-based variants, have a low energy density when compared to common fossil fuels, such as methanol and gasoline [123] [48]. Battery-powered unmanned aircraft that are being equipped for long-range missions typically result in a high system weight. This reduces the operational capabilities of such systems. Additionally, new tech-

nologies are being developed, such as hydrogen fuel cells that offer an increased energy density. However, the technology has not yet matured due to obstacles in unit-pricing and reliability [3]. More recently hybrid-electric propulsion systems (HEPS) for manned and unmanned aircraft have received increased scientific and industrial interest [30]. Such systems aim to combine the advantages of high-torque found in electric propulsion with the advantages of high energy density of ICE fuels.

Regardless of the chosen propulsion method, optimization of the in-flight mission performance of small unmanned aircraft is believed to be a fundamental exercise in maturing the technology within industrial applications. Allowing unmanned aircraft to fly longer, further, cheaper and safer, adds to the use case, which competes with its manned counterpart. Considering the potential benefits of unmanned aircraft to the industry, it is considered warranted to perform research on finding methods that increase the in-flight performance of small unmanned aircraft.

An obstacle in the safe application of small unmanned aircraft is the potential presence of harsh environmental conditions. Depending on geographical location it is not uncommon for aircraft to encounter wind speeds ranging 20-50% of the aircraft's airspeed [8]. Depending on the wind direction in relation to the aircraft's trajectory this may constitute a significant positive or negative effect on the aircraft performance. Other extreme weather conditions, such as wing icing, also induce a substantial reduction in flight performance by reducing lift, increasing drag, weight and resulting energy consumption [128]. Moreover, in-flight icing constitutes a large risk for operational safety [149].

An essential component in effective path planning is optimization with a thorough integration of these environmental effects on the aircraft performance in order to compute an optimal trajectory. Finally, as some missions rely on in-flight communication, such as during search-and-rescue missions, it is warranted to optimize the path of the aircraft considering aircraft performance, environment and communication constraints. The research presented in this work suggests methods for small unmanned aircraft to optimize these operational parameters that influence the aircraft range, endurance, communication and operational safety.

The highlighted novelty of the research presented in this thesis resides in the strong incorporation of aircraft performance models into sophisticated path planning algorithms in relation to environmental conditions – and the practical value that follows from such methods. The researcher aims to contribute to science and industry by providing an increased understanding of the optimal use of small unmanned aircraft that are operating in varying weather conditions. Finally, the researcher was responsible for the conceptual and aerodynamic design of the battery-powered fixed-wing sUAS PX-31, which is produced today by the company Maritime Robotics AS.

1.2 Structure of the Thesis and Main Contribution

The main input for this thesis are several published and submitted papers. The total content is divided into five parts that each contribute to the main objective of an increased understanding and optimizing the use of fixed-wing small unmanned aircraft in long-range missions.

Part I: Long-range Flight Performance and Environment

This part contains two chapters describing in-flight performance and path planning methods for small unmanned aircraft considering environmental parameters such as wind and icing conditions.

- **Chapter 2 - Inclusion of horizontal wind maps in path planning optimization of UAS:** This chapter present a method for optimizing the planned path of a small unmanned aircraft through inclusion of publicly available horizontal wind maps. It starts off by describing and quantifying the effects of horizontal wind on the aircraft flight performance by analysing the power requirements with varying en-route horizontal wind speeds and wind directions. By modelling these effects, the opportunity is created for path planning algorithms to take such effects into account. It allows for the aircraft to optimize its commanded airspeed and the chosen path of the aircraft. Several optimization goals can be set, though in this chapter it was chosen to demonstrate the methods and benefits through a simulation of a typical A-to-B mission at fixed cruising altitude, which is set up to minimize the total energy consumption, using Particle Swarm Optimization (PSO) path planning techniques.
- **Chapter 3 - Long range path planning using an aircraft performance model for battery powered sUAS equipped with icing protection system:** This chapter presents a method for long range path planning optimization for battery-powered small unmanned aircraft that are equipped with an icing protection system. The chapter builds on top of the methods described in the previous chapter, and expands this to a multi-altitude optimization, which also takes into account broader environmental conditions - primarily the effects of potential in-flight icing. To achieve such an optimization the aircraft performance model is upgraded to include climb and descent performance, as well as including a model that quantifies the performance degradation due to in-flight wing icing. Finally, battery discharge characteristics are included in the performance model. Similar to the previous chapter the benefits of such methods are demonstrated through a simulation of a

typical A-to-B mission using PSO techniques, which is set up to minimize the total energy consumption.

Part II: Long-range Flight Performance and Safety

Mission robustness is a prerequisite for safe operations. One method to increase the operational robustness is to utilize available redundant propulsion systems. This part contains one chapter addressing methods for optimizing the in-flight safety using advanced path planning in conjunction with aircraft performance models and en-route environmental conditions.

- **Chapter 4 - Contingency path planning for hybrid-electric UAS:** This chapter presents a path planning method for optimizing the in-flight safety of hybrid-electrically powered small unmanned aircraft. A hybrid-electric propulsion system (HEPS) typically contains an internal combustion engine, complemented by a battery-powered electric motor. In case of a critical engine failure, the electric motor might still be able to fly the aircraft to a safe landing spot. By modelling the aircraft performance in conjunction with the remaining battery capacity, paths can be calculated that guarantees the aircraft to always remain within range of a safe landing spot. This chapter demonstrates these advantages by simulating a typical A-to-B mission that is set up to find a route which guarantees (or increases the time) being in range of a safe landing spot in the event of an engine failure. Similar to the previous chapters, the path is chosen to minimize the energy consumption, while taking in to account en-route winds, using PSO techniques.

Part III: In-flight Performance and Airframe Design Considerations

Previous parts focused on environmental factors and path planning methods in an effort to increase the operational envelope of small unmanned aircraft. This assumed an airframe with pre-defined performance characteristics, including its consequent aerodynamic model and propulsion efficiency. However, to increase the operational envelope it is considered relevant to also explore the design of the aircraft, and to review the opportunities to optimize the inherent aerodynamic behaviour. This part will focus on several methods aiding in airframe design optimization and efficient mission planning.

- **Chapter 5 - Mission performance trade-offs of battery-powered sUAS:** This chapter provides an increased understanding of the mission weight, flight altitude and airspeed and the penalty on the the performance

of battery-powered aircraft. In particular the mission range, endurance and aircraft stall speed. This is demonstrated by performing a sensitivity study. An additional dimension added to the research is the inclusion of battery discharge effects, including Peukert's effect.

Part IV: Discussion and recommendation for future work

Appendices

- **Appendix A - Path planning of Multi-UAS communication relay by decentralized MPC:** A notable example application of unmanned aircraft technology is the ability to function as airborne communication relay system. The rapid deployment and surface-independent operations contribute to its use case. This is especially relevant for communication relaying of moving objects, such as boats or unmanned surface vehicles (USV), which may continuously reposition itself. This work demonstrates the possibilities and advantages of such applications by simulating a mission where multiple unmanned aircraft relay the communication between a moving USV and a land-based base station. A complexity in this application is that the optimal location of the airborne relay stations dynamically changes based on the USV's location in relation to the base station. Moreover, in the context of this thesis' topic, the planned path is dynamically chosen to optimize while guaranteeing communication range while guaranteeing a predefined minimum level of signal quality. This is done by taking into account the aircraft performance (in particular maneuvering) and the influence of en-route horizontal winds.

- **Appendix B - Autonomous unmanned aerial vehicles in search and rescue missions using real-time cooperative model predictive control:** This Appendix provides a work on the advantages of deploying multiple unmanned aircraft in Search and Rescue (SAR) missions is compared to deployment of a single system. The main parameter to optimize is the time it takes to locate a missing person. This is explored by simulating SAR missions with one, two or three cooperative airborne systems. The operational performance of these aircraft are integrated through inclusion of the performance model into the simulations. This includes the effects of wind. The probability of success is examined for different operational scenarios.

- **Appendix C - Survey of design considerations of optical image stabilization systems for small unmanned aerial systems:** This Appendix

provides a work on increasing the insight in the design considerations of camera gimbal systems, which are commonly found on small unmanned aircraft. In context of this thesis, this chapter discusses the relevance of including the aerodynamic considerations into the design and placement of the camera gimbal system on the aircraft.

1.3 Publications

The findings presented in this thesis have been previously published and/or submitted to scientific outlets. These consist of scientific conferences and journals. The following works have been included in this thesis:

- [73] A. R. Hovenburg, F. A. A. Andrade, C. D. Rodin, T. A. Johansen, and R. Storvold. Inclusion of horizontal wind maps in path planning optimization of UAS. In *2018 International Conference on Unmanned Aircraft Systems (ICUAS)*, pages 513–520. IEEE, 2018.

- [70] A. R. Hovenburg, F. A. A. Andrade, R. Hann, C. D. Rodin, T. A. Johansen, and R. Storvold. Long range path planning using an aircraft performance model for battery powered sUAS equipped with icing protection system. Submitted for publication.

- [71] A. R. Hovenburg, F. A. de Alcantara Andrade, C. D. Rodin, T. A. Johansen, and R. Storvold. Contingency path planning for hybrid-electric UAS. In *2017 Workshop on Research, Education and Development of Unmanned Aerial Systems (RED-UAS)*, pages 37–42. IEEE, 2017.

- [72] A.R. Hovenburg, T. A. Johansen and R. Storvold. Mission performance trade-offs of battery-powered sUAS. In *2017 International Conference on Unmanned Aircraft Systems (ICUAS)*, pages 601-608. IEEE, 2017.

- [24] F. A. A. Andrade, C. D. Rodin, A. R. Hovenburg, T. A. Johansen, and R. Storvold. Path planning of multi-UAS communication relay by decentralized MPC. In *2018 OCEANS-MTS/IEEE Kobe Techno-Oceans (OTO)*,pages 1–8. IEEE, 2018.

- [5] F. A. A. Andrade, A. R. Hovenburg, L. N. Lima, C. D. Rodin, T. A. Johansen, R. Storvold, C. A. B. Correia, and D. B. Haddad. Autonomous

unmanned aerial vehicles in search and rescue missions using real-time cooperative model predictive control. Submitted for publication.

- [114] C. D. Rodin, F. A. A. Andrade, A. R. Hovenburg, T. A. Johansen, and R. Storvold. A survey of design considerations of optical imaging stabilization systems for small unmanned aerial systems. Submitted for publication.

Part I

Long-range Flight Performance and Environment

Chapter 2

Inclusion of Horizontal Wind Maps in Path Planning Optimization of UAS

Earlier studies demonstrate that en-route atmospheric winds significantly affect the in-flight performance of unmanned aircraft. Nevertheless today the inclusion of wind is not common practise in determining the optimal flight path. This chapter aims to contribute with an accessible method that includes forecast horizontal wind maps which are commonly available, and discuss the methods on how these maps can be integrated in order to obtain the most energy efficient horizontal path of fixed-wing aircraft. The benefits of including horizontal wind maps into the path planning optimization are demonstrated through a simulation, which utilizes Particle Swarm Optimization to find the optimal cost-beneficial path.

2.1 Introduction

Atmospheric winds pose constraints on the operations of unmanned aircraft. This holds especially true for smaller aircraft, as here it is common for wind speeds to constitute 20-50% of the airspeed [8]. This has a substantial effect on the mission safety and the aircraft's in-flight performance. It is therefore considered to be warranted to account for atmospheric winds in the planning of the aircraft's flight path. As the unmanned aircraft industry is maturing, a growing scientific search towards in-flight performance optimization is noticed. Accurate estimations of the aircraft's in-flight performance allow for optimal utilization of the system within its specified mission objectives.

Early studies demonstrate the advantages of utilizing atmospheric winds in the

aircraft's route optimization [20]. More recently efforts have been made to include the complete wind field in the optimization, such as found in [47], and more recently in [42], which utilize the Ordered Upwind Method and the stochastic Dijkstra algorithms, respectively, for determining the optimal flight path.

The study of path planning optimization in the context of *unmanned* aircraft is relatively new but abundant. Most notably, in [102] a method is presented that successfully incorporates wind fields in path following methods utilizing straight-line and circular arc paths. In [117] a sophisticated method was described where Model Predictive Control (MPC) methods were employed for path planning optimization, while including the effects of wind. However, neither studies included the effects of wind on the aircraft performance within the optimization, such as was the case in [42], which describes a method for the incorporation of weather uncertainty for manned aircraft in long-distance flights. In [23] the aircraft performance was successfully included, with the assumption of a constant wind field.

More recent sophisticated wind-energy harvesting methods have received increased scientific interest. Most notably in [54] two refined methods are described which utilize updraft winds from locally observed wind-fields in order to extend the aircraft's range and endurance. Considering such complex wind fields offers the potential of effective path optimization. However, the limitation of such methods in context of the study presented in this chapter is that it relies on the availability of detailed local wind measurements and terrain observations or maps. In practise the extraction of lift due to *vertical* winds over terrain, known as orographic lift, is relatively complex to obtain [97]. This is in contrast to forecast horizontal wind gradients which are relatively well described, and are commonly obtainable through meteorological institutions.

The study presented in this chapter positions itself in the current literature by describing an accessible method that includes forecast horizontal wind maps, and discuss the methods on how these maps can be integrated in order to obtain the most energy efficient horizontal flight path of fixed-wing unmanned aircraft. To achieve this, it specifies and includes the effects of horizontal winds on the in-flight performance of the aircraft. In this chapter the Particle Swarm Optimization (PSO) technique is applied, such as described in Appendix D, in order to simulate how the inclusion of wind affects the flight performance. PSO was chosen because it is easy to implement, there are few parameters to adjust and it uses global and local performance, which is advantageous in this type of problem where it is expected that the optimal solution is likely to be a relatively small deviation from the known solution candidate - the straight path.

The goal of the developed algorithm is to find the path which minimizes the total

energy consumption from origin to destination by using a forecast wind map and by optimizing the path and airspeed of the aircraft. Minimizing the energy consumption results in a lighter aircraft as battery-powered aircraft are required to carry fewer on-board batteries, while fuel-powered aircraft require to carry less block fuel. Alternatively, one could consider the reduction in required fuel/batteries to increase the cargo capacity of the aircraft, or to offer a larger safety margin through energy reserves.

2.2 Aircraft dynamic model

The aircraft's kinematic model is described through the North-East-Down (NED) inertial reference frame. As the aim is to optimize the energy consumption per distance travelled, it is necessary to describe the wind field in a similar way. Because in this study horizontal wind maps are used, the wind field is being described in a two-dimensional plane.

When assuming a flat, non-rotating earth then x aligns north, y aligns east, and z is pointing down to earth as positive direction. Relating to the wind navigation triangle, as shown in figure 2.1, the aircraft's inertial velocity in a coordinated flight can be described as a function of the aircraft's ground course χ and ground speed v_g. Similarly, this can be described as a function of the true airspeed v_a, heading ψ, wind speed v_w and wind speed direction ψ_w. These relations are found through:

$$\begin{bmatrix} \dot{x} \\ \dot{y} \end{bmatrix} = v_g \begin{bmatrix} \cos\chi \\ \sin\chi \end{bmatrix} = v_a \begin{bmatrix} \cos\psi \\ \sin\psi \end{bmatrix} + v_w \begin{bmatrix} \cos\psi_w \\ \sin\psi_w \end{bmatrix} \tag{2.1}$$

The relation between heading and course angle is conveniently described using the law of sines, resulting in [117]:

$$\psi = \chi - \arcsin\frac{v_w}{v_a}\ \sin\left(\psi_w - \chi\right) \tag{2.2}$$

In aviation the wind maps and directional indications are often expressed in the navigation representation, rather than the mathematical representation. Therefore it is considered convenient to apply the same standards here. Here the directional indications are related to x (true north), where the clockwise rotation is positive. Note that wind maps commonly indicate the direction where the wind is coming from, rather than where it is going towards.

In an attempt to more accurately determine the aircraft's in-flight performance, one may consider including the parallel wind speed along the aircraft's heading $v_{w\psi\parallel}$.

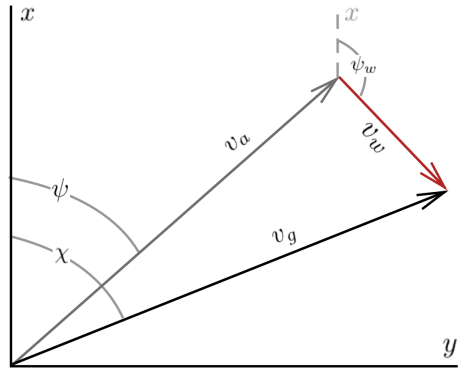

Figure 2.1: Wind Navigation Triangle in Coordinated Flight

When the wind components are decomposed as demonstrated in equation (2.1), then the wind speed $v_{w\parallel}$ can be found through:

$$v_{w\parallel} = v_{wx} \cos\psi + v_{wy} \sin\psi. \tag{2.3}$$

2.3 Effects of wind on in-flight performance

Depending on the magnitude and direction of the wind in relation to the aircraft's desired ground path, the presence of wind has an effect on the in-flight performance. In a typical mission considered in this study most in-flight time will be spend during the cruise phase. In the context of path planning optimization it is therefore the cruise phase that is considered most relevant. The remainder of the study shall consider path planning optimization methods and considerations for the cruise phase of fixed-wing unmanned aircraft.

The basis of the optimization methods presented in this chapter relies on the trade-off between energy consumption and distance covered. To illustrate; when flying an A-to-B mission with a fixed distance, then the optimization goal considered in this study is to minimize the energy consumption during the execution of this mission. It is therefore required to express the aircraft's energy consumption as a function of distance covered. The required power (P_r in Watts) of propeller-driven aircraft is found through [3]:

$$P_r = D\, v_a = \sqrt{\frac{2\, W^3}{\rho_\infty\, S}\frac{C_D^2}{C_L^3}} \tag{2.4}$$

Where W is the aircraft weight in [N], C_L and C_D are the aircraft's aerodynamic lift and drag coefficients respectively, ρ_∞ is the air density in [kg/m^3], and S is the aircraft's effective wing surface in [m^2].

The aircraft's in-flight performance can be optimized for different mission scenarios. The best range airspeed is found by flying at the airspeed where the energy consumption per travelled distance is minimized. Considering that:

$$v_a = \sqrt{\frac{2}{\rho_\infty}\left(\frac{W}{S}\right)\frac{1}{C_L}} \tag{2.5}$$

Then, when substituting equation (5.4) in (5.6) we find:

$$\left(\frac{P_r}{v_a}\right) = W\left(\frac{C_D}{C_L}\right) \tag{2.6}$$

This expression shows that the condition for maximum range occurs at the airspeed where C_L/C_D is maximized. However, as this expression relates travelled distance solely to airspeed rather than ground track speed, this does not necessarily hold true in the presence of en-route winds.

The specific energy consumption SEC is defined as the consumed energy per distance travelled. This can be expressed in unit Newtons (N), Joule per meter (J/m), or alternatively Watt-second per meter (Ws/m). Here the latter is chosen since manufacturers of batteries often express the energy capacity in Watt-hour. By plotting the specific energy consumption (obtained from equation 2.6) as a function of v_w and ψ_{wr} (obtained from equation 2.1 and 5.6), the effects of wind on the in-flight performance can be visualized. Here ψ_{wr} is the wind direction relative to the aircraft's course.

In Figure 2.2A such a plot is illustrated which holds valid for the aerodynamic model of the P31016 unmanned aircraft, flying at a ground velocity of 28.8 meters per second and an altitude of 1500 meters under ISA conditions. The P31016 is the unmanned platform used in the path planning scenario, which is specified further in section 2.4.2.

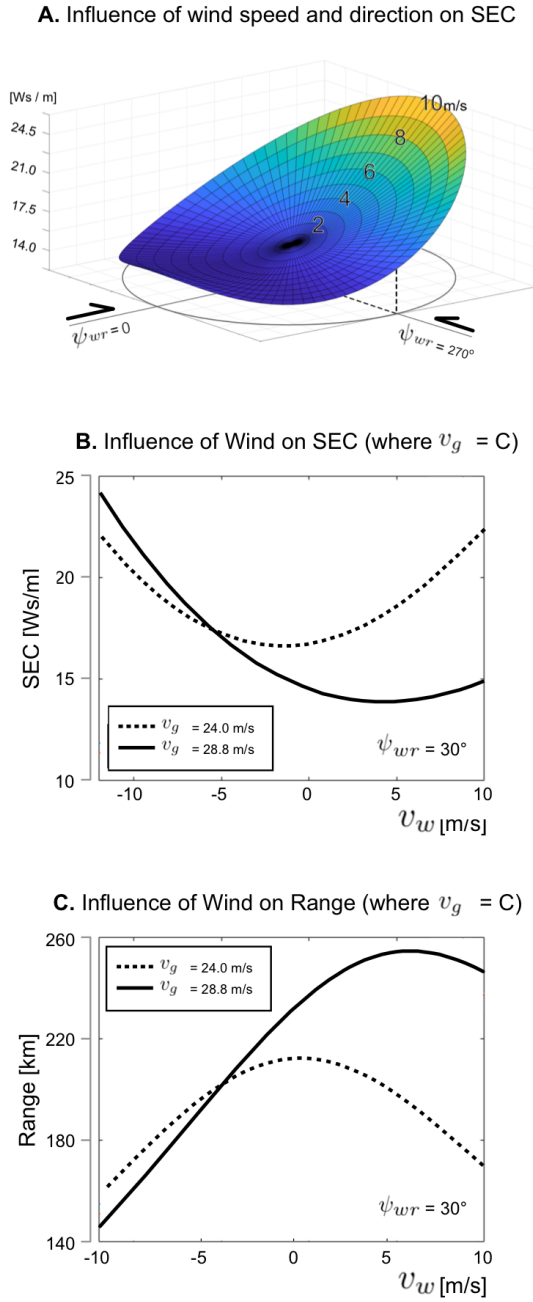

Figure 2.2: A: Energy consumption of the P31016 per distance travelled as a function of wind speed, and the wind direction relative to the aircraft's course ψ_{wr}. B: SEC for different wind speed components, valid for ψ_{wr} of 30 degrees with fixed ground speeds. C: Flight range for different wind speed components, valid for ψ_{wr} of 30 degrees with fixed ground speeds. ($v_w > 0$ is a tail wind, while $v_w < 0$ is a head wind)

Figure 2.2B shows the performance penalty of the presence of wind at the commanded ground speed of 24.0 and 28.8 meters per second, for the arbitrarily chosen ψ_{wr} of 30 degrees. This figure illustrates that for one given wind speed and direction the maximum range may be obtained by changing the commanded ground speed accordingly. Note that without the presence of wind flying at an airspeed of 24.0 meters per second requires less power per unit *time* compared to flying at 28.8 meters per second. However, as this figure illustrates the energy consumption per unit *length* is found to be lower when flying at 28.8 meters per second. This balance changes depending on the present wind. This is further demonstrated in 2.2C where the resulting obtainable in-flight range is illustrated for both ground speeds.

Path planning optimization algorithms that are set up so that the cost-function optimization considers the energy consumption as a function of covered ground distance in the presence of wind will inherently optimize the commanded airspeed to give the best range. In other cases where the cost function algorithm is set up to command the desired airspeed independently of ground speed, methods such as described by [61] can be applied. In [61] it is suggested that the best-range airspeed can be approximated through:

$$m_{br} = \left[\frac{2\, m_{br} \pm \left(\frac{v_{wp}}{v_{md}} \right)}{2\, m_{br} \pm 3 \left(\frac{v_{wp}}{v_{md}} \right)} \right]^{\frac{1}{4}} \tag{2.7}$$

Here v_{md} is the minimum drag airspeed, v_{wp} is the wind speed along the commanded heading of the aircraft. By solving for m_{br} the ratio between the best-range airspeed in the presence of wind, and the airspeed that gives the best-range without the presence of wind can be found. The symbol $\pm$ indicates a head- or tailwind, where positive values are considered a tailwind.

Missions that require the longest flight endurance, such as observation missions, ought to optimize the airspeed so that the energy consumption per unit time is minimized. Observing equation (2.4) it becomes clear that when the air density, aircraft weight, and wing surface are constant, the total energy consumption becomes a sole function of C_L and C_D. The minimum power consumption, and thus the maximum endurance, is found at the v_a where C_L^3/C_D^2 is maximized. Note that the presence of wind does not change the optimum value for v_a to achieve the maximum endurance.

Similarly, path planning optimization algorithms where the cost-function considers the energy consumption as a function of time will inherently optimize the airspeed

to obtain the best flight time.

2.4 Path-Planning

In this section the path-planning solution with the inclusion of the horizontal wind maps is presented. The results are shown after describing the optimization problem formulation, the parameters of the aircraft used for this simulation and how the wind map was obtained to perform the wind interpolation.

2.4.1 Optimization Problem Formulation

An area north of Trondheim, Norway, was chosen for this study. The objective of the optimization is to fly from A to B while using as little energy as possible, while taking the wind into consideration. To achieve this the mission waypoints and the airspeed along the path are optimized using the Particle Swarm Optimization technique, through methods as described in Appendix D.

A two-dimensional geometric approach is used in this work, where the optimization variables represent a set of airspeed inputs V and waypoints of the path W, with x (North) and y (East) positions in the NED reference frame. The altitude was chosen to be 1500 meters.

As the positions of the origin $[x_s, y_s]$, destination $[x_t, y_t]$ and wind vectors $[v_w, \psi_w]$ are given in latitude and longitude coordinates, a conversion to the NED frame is needed. Besides, to use the result as an input for an autopilot system, it may be required to convert the waypoints to positions expressed in latitude and longitude. To reduce the error coming from the conversion between frames, the coordinates of the origin of the NED frame are defined as the midpoint between the origin and the destination.

As the path is divided into V velocity steps and W waypoints, the algorithm needs to do an interpolation to discretize the path obtained from the W waypoints into a path with V velocity steps. Therefore, the new path will have $V + 1$ new interpolated waypoints, where $[x_1, y_1] = [x_s, y_s]$ will be the origin of the mission, $[x_{V+1}, y_{V+1}] = [x_t, y_t]$ will be the destination and the other $V-1$ points are resulted from the interpolation.

The cost function f is set in order to evaluate the energy consumption along the path. Therefore, it adds the energy consumption used to travel each V step through:

$$f = L_{step} \sum_{n=1}^{V} \frac{P_{r_n}}{v_{gs_n}}, \tag{2.8}$$

where P_{r_n} is the required power (ref. equation (2.4) and v_{gs_n} is the ground speed in meters per second for the nth velocity step. L_{step} is the length of each step of the path, given by:

$$L_{step} = \frac{L}{V} \tag{2.9}$$

where L is the total length of the path:

$$L = \sum_{n=1}^{V} \sqrt{(x_{n+1} - x_n)^2 + (y_{n+1} - y_n)^2} \tag{2.10}$$

The domain (x_{min}, x_{max}, y_{min}, y_{max}) has to be defined taking into consideration that the UAS may not deviate too far from the straight line path between the origin and destination. In addition, the airspeed must be optimized within the limits of the aircraft constrains.

To initialize the optimization algorithm, first a straight path from the origin to the destination is generated - with waypoints distributed equally along the path, while the airspeed along the path is set as the airspeed that would give the best range without the presence of wind. This strategy is crucial, as usually the optimal solution will be a deviation from this straight path. If only particles initialized with random positions are used, they might have uncommon waypoints displacement, causing the algorithm to take a long time to find an optimal solution or to get stuck in a local minimum.

The other paths generated for the initialization of the optimization algorithm have the waypoints randomly chosen following the rule that the next waypoint must be closer to the destination than the previous one. The airspeed variables are randomly chosen between the minimum ($\boldsymbol{v}_{a_{min}}$) and maximum ($\boldsymbol{v}_{a_{max}}$) airspeed. Figure 2.3 shows an initial guess for the paths.

2.4.2 Aircraft Platform

The P31016 (figure 2.4) is a small battery-powered aircraft that is powered by a 6.0 kilowatt brushless motor, and has a battery capacity of 977 Watt-hour. The propulsion efficiency is assumed constant at 50% with an ideal electrical discharge

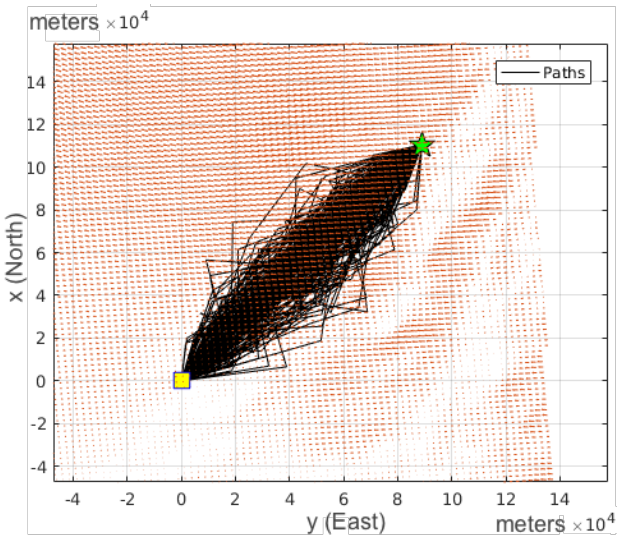

Figure 2.3: 200 paths generated in the initial guess. The yellow square is the origin and the green star is the destination. The red arrows are the wind vectors.

pattern. The aircraft has a wing surface of 0.81 square meters and has a typical mission-ready mass of 17.5 kilograms. Its aerodynamic characteristics were determined through a simplified model of the aircraft in the software tool XFLR5. Here it was found that at an altitude of 1500 meters under ISA conditions the airspeed for maximum range occurs at 28.8 meters per second, while the airspeed for maximum endurance is found at 24.0 meters per second. The aircraft's stall speed with extended flaps is 14 meters per second, while the maximum speed is limited to 38 meters per second.

Figure 2.4: P31016 concept battery-powered fixed-wing unmanned aircraft

2.4.3 Wind vector maps

The horizontal wind map used was originally obtained from the Norwegian Meteorological Institute (MET), and provided by the Norwegian Defence Research Establishment (FFI). The wind map contains the amplitude and direction of the wind for each point in the grid at a given altitude. The grid has a resolution of approximately 2.5 kilometers, and the position of the points are given as the latitude and the longitude. Figure 2.5 illustrates a section of the wind map used.

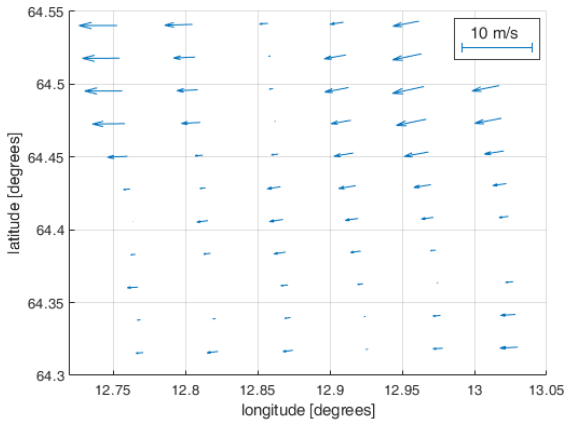

Figure 2.5: Part of the wind map used. The arrows show the amplitude and direction of the wind for each point in the grid.

In order to obtain wind data in between the grid points in the wind map, the wind data needs to be interpolated. Nearest neighbor interpolation could be used for fast interpolation, and could provide sufficient accuracy for a smooth wind field. However, the discontinuity of nearest neighbor interpolation or abrupt wind changes could cause significant errors. In order to improve this, biharmonic spline interpolation [119] is used. Biharmonic spline interpolation has the benefits of creating a smooth surface (has minimum curvature) and passes through each data point. To obtain a sufficiently low computation time, the 16 surrounding grid points (the smallest and second smallest squares, each containing unique grid points, and enclosing the point to be interpolated) are selected as the data points for calculating the interpolation function.

2.4.4 Results

The parameters chosen to set the optimization algorithm are shown in Table 2.1. Figure 2.6 shows the optimized path (black dots) for the mission where the objec-

tive is to fly from the yellow square (origin) to the green star (destination). The algorithm has optimized the position of the five waypoints (blue dots) and the airspeed at each V-step. The resulted optimized airspeed is shown in figure 2.7. In this mission the total energy consumption calculated for the straight line path, when flying at the no-wind best-range airspeed of 28.8 meters per second, was 691 Watt-hour. The total energy consumption of the optimized path was 662 Watt-hour. This is a saving of 4.2% of consumed energy. This is despite the fact that the optimized path is 3.6 kilometers longer than the straight path. An overview of the results of the flight time, path length and energy consumption as a comparison between the straight path and the optimized path are shown in Table 2.2.

Table 2.1: List of parameters

Name	Value
Iterations	200
Particles	200
Waypoints (W)	5
V	50
Particle Size	55
Particle velocity constraint	0.1 x Domain
w_{ini}	1.0
w_{fin}	0.1
x_{min}	x_s-$L_{min}/3$
x_{max}	x_t+$L_{min}/3$
y_{min}	y_s-$L_{min}/3$
y_{max}	y_t+$L_{min}/3$
$v_{a_{min}}$	18 m/s
$v_{a_{max}}$	38 m/s

Table 2.2: Simulation results

	Straight Path	Optimized Path
Length	141.8 km	145.4 km
Time	1h 37min	1h 29min
Consumed energy	691 Wh	662 Wh

2.5 Discussion

The wind maps used in this study represents the wind information obtained through meteorological wind models. As the current wind map is only valid for that moment

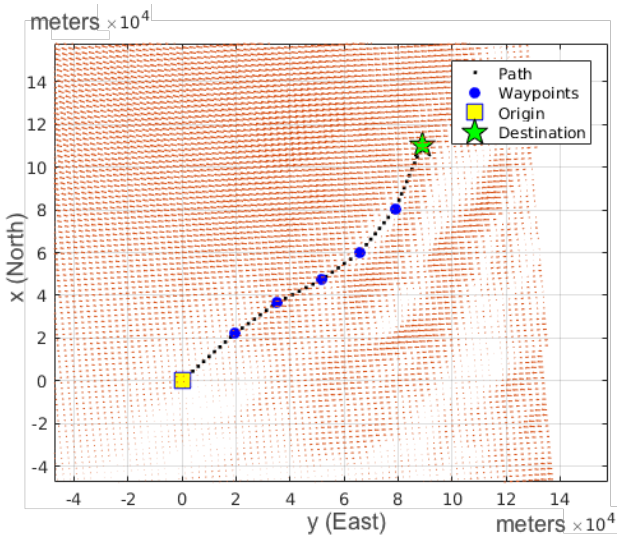

Figure 2.6: Final path - Accounting for en-route winds

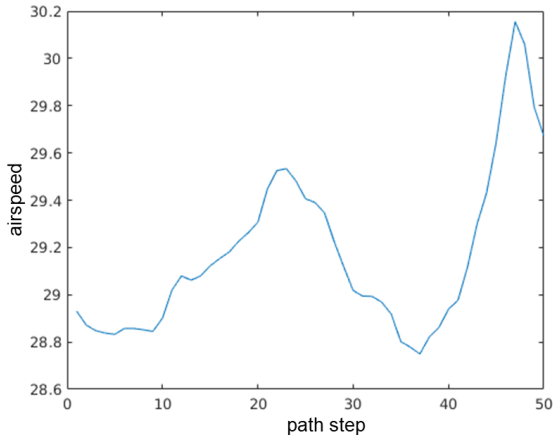

Figure 2.7: Optimized commanded airspeed along the route

in time, for longer flights it may prove useful to include forecast wind maps valid for future time windows. Moreover, in-situ path planning may be complemented with real-time wind field estimations through methods such as described in [54] and [85]. In the work described in [10] a real-time field estimation method is described utilizing a moving horizon estimator, which may be used to identify both steady and turbulent wind velocities.

The simulation results presented in this chapter are valid for one chosen scenario.

Depending on the local wind field and aerodynamic characteristics of the aircraft the obtainable savings may be higher or lower for other scenarios. It is important to extend this research in the future with more varied scenarios, while having a validated aerodynamic model and propulsion efficiency model of the used aircraft. Finally, the accuracy of the simulation results are as always limited by the accuracy of the input parameters, which to a large extend include the predicted wind field model. As horizontal wind maps do not specify vertical wind components, these effects are not included. It is therefore warranted that in a future research the proposed model is verified through field tests. This is done preferably for a variety of mission scenarios with a different wind field, altitude and terrain.

It is important to complement the proposed method with the ability to include horizontal wind maps of different altitudes, and thereby effectively creating a quasi-three-dimensional wind field. This allows for en-route adjustment of the cruise altitude which has the potential to further increase the obtained flight efficiency.

2.6 Conclusion

In this chapter a method was presented for the inclusion of horizontal wind maps into a path planning optimization algorithm. An aircraft performance model is presented that incorporates the effects of wind on the in-flight energy consumption, in relation to the airspeed and the resulting ground speed. It is demonstrated that in the presence of wind the best-range airspeed is no longer found at the airspeed associated with $(C_L/C_D)_{max}$, thus en-route airspeed optimization is warranted. It is described that when the goal is to maximize the flight range, an optimization algorithm which is set up to optimize the commanded airspeed in order to minimize the energy consumption as a function of ground distance covered, will inherently command the optimal course and airspeed in the presence of wind.

A simulation was performed where a particle swarm optimization method was utilized to determine the wind-optimized flight path, where an in-situ forecast 2D wind field was incorporated. The performed simulation shows that when comparing the wind-optimized flight path to the straight path, the length increased with 3.6 kilometers to a total of 145.4 kilometers. However, the flight time was reduced by eight minutes and the total consumed energy was reduced by 4.2%. These simulation results are valid for the chosen scenario utilizing the P31016 unmanned aircraft. In future work it should be particularly interesting to simulate a more diverse wind field. In addition it is warranted to validate the proposed model through field experiments.

Chapter 3

Long range path planning using an aircraft performance model for battery powered sUAS equipped with icing protection system

Earlier studies demonstrate that en-route atmospheric parameters, such as winds and icing conditions, significantly affect the safety and in-flight performance of unmanned aerial systems. Nowadays, the inclusion of meteorological factors is not a common practice in determining the optimal flight path. This study aims to contribute with a practical method that includes meteorological forecast information in order to obtain the most energy efficient path of a fixed-wing aircraft. The Particle Swarm Optimization based algorithm takes into consideration the aircraft performance, including the effects of en-route winds and the power required for active icing protection systems to mitigate the effects of icing. As a result, the algorithm selects a path that will use the least energy to complete the given mission. In the scenario evaluated with real meteorological data and real aerodynamic parameters, the battery consumption of the optimized path was 52% lower than the standard straight path.

3.1 Introduction

Small Unmanned Aerial Systems (sUAS) have become versatile tools that can be used in a broad spectrum of missions. The rapid growth of the use of sUAS is justified by their endurance, reduced cost, rapid deployment and flexibility. This flexibility is mainly due to the many types of sensors that can be mounted on sUAS, enabling them to be used in many different applications, such as surveillance, recon-

naissance, search and rescue, delivery, photogrammetry, inspection, among others. In addition, they offer reduced risk for humans and impact on the environment, when compared to manned aircraft.

A next and necessary step for the continuous evolution of sUAS technology is to enable safe autonomous missions also in adverse weather conditions. For this to be possible, effects of wind and icing on the aircraft performance must be addressed, controlled and taken into consideration by the path planning algorithm to decide if it is worth it to face the adverse weather conditions or to take a detour in order to avoid exposing the sUAS to this.

Scientific literature on path planning of sUAS is abundant. In [68] a comparative analysis of four three dimensional path planning algorithms based on geometry search was done. The algorithms compared were Dijkstra, Floyd, A* and Ant Colony. Run time and path length were the two analyzed aspects. In [21], the author used the Voronoi diagram to produce routes minimizing their detection by radar, while in [153] the Rapidly Exploring Trees (RTTs) were used with a smoothing algorithm based on cubic spiral curves for collision-free path planning. Optimization techniques are also adopted, as Genetic Algorithms [104], MILP [112] and Particle Swarm Optimization [90], where the author used the method to minimize the UAS path's length and danger based on the proximity of threats.

Atmospheric winds usually constitute 20-50% of the airspeed of sUAS [8]. Therefore, it affects the aircraft's in-flight performance significantly. In [117], a sophisticated method was described where Model Predictive Control (MPC) was employed for path planning optimization including the effects of uniform wind. In [1], the author used Markov Decision Process to optimize the unmanned aerial vehicle's path, integrating the uncertainty of the wind field into the wind model. The goal of the algorithm was to minimize the energy consumption and time-to-goal. A similar approach was chosen in [77], where the Ant Colony Optimization (ACO) technique was used to optimize the path by minimizing the travel time considering the effects of an uniform wind.

Most of the works about path planning of sUAS that takes the wind into consideration use an uniform wind distribution. This information is often used in a simplified model when calculating the effects of the wind on the energy consumption. However, in [23], an aircraft performance was successfully included, with the assumption of a constant wind field. In recent literature a nonuniform wind distribution in addition to an aircraft performance model was used. That is the case in [71], where the flight path was optimized so that sUAS was guaranteed to be able to reach a pre-designated safe landing stop. This was done by continuously calculating the remaining range considering the remaining battery capacity in case

of an engine failure. In that study a wind map with nonuniform wind distribution was used in the calculations of the maximum range of the sUAS. Also using a nonuniform wind distribution, [73] proposed a two-dimensional optimization algorithm to find the path between two points with the minimum energy consumption. By being aware of the wind map valid for a given altitude, it was possible to choose a path where the wind was used favorably for energy savings for that flight level.

One of the most important meteorological constraints for UAS mission planning is atmospheric icing. This hazard is also called in-cloud icing and occurs when an airframe travels through a cloud containing supercooled liquid droplets. When these droplets collide with the airframe they freeze and result in surface icing that grow over time into ice horns that can significantly alter the wing shape. Even small ice accretions have been shown to be able to decrease the aerodynamic performance of a wing dramatically [14] [93].

The icing hazard is a well-researched topic for general aviation, but little attention has been given to this topic until the recent years for UAS – although the issue has already been identified during the 1990s [124]. UAS icing is in many ways similar to icing on large aircrafts, but also exhibits significant differences when it comes to flight velocities, airframe size, mission profiles, and weight restrictions. In particular, the small UAS typically operate at Reynolds numbers an order of magnitude lower compared to general aviation which causes differences in the flow regime [129].

Modeling of icing effects on UAS have shown that icing results in a degradation of aerodynamic performance. Ice accretions on the leading edge of the lifting surfaces can decrease lift, increase drag, and initiate earlier stall [130]. The degree of the degradations seems strongly linked to the prevailing meteorological conditions. In addition, icing has also shown to have detrimental effects on static and dynamic stability. In summary, icing is a severe hazard, especially for small UAS, and it is common practice to avoid flying in icing at all costs.

An icing protection system (IPS) can be used to mitigate this restriction of the flight envelope. In the scope of this work an electro-thermal system designed at the Norwegian University of Science and Technology will be investigated [127] [66]. This system consists of heating zones on the leading edge of the lifting surfaces that are activated when the aircraft enters an icing cloud. The IPS can run in two different modes. In anti-icing mode, the system will continuously heat the leading edge to inhibit the build-up of any ice. In de-icing mode, the systems operates in a cyclic way, allowing for the accumulation of a small amount of ice over a time of 90 s, followed by the removal of the ice by activating the heating zones for 30 s. Typically, the de-icing mode will require lower power requirements compared to anti-icing,

but will also results in performance degradation during the ice accumulation cycles [49].

As weather conditions often varies for geographic location and altitude, it is important that the path planning algorithm is able to allow altitude changes in during flight. Consequently, the terrain profile must be taken into consideration and treated as an obstacle by the algorithm. This was previously implemented by [113], where the PSO and Parallel GA optimization techniques were compared when used to find the best trajectory by minimizing a cost function based on the path length and average altitude, including a penalization in the cases when the path has parts under the terrain.

Electric batteries have variable potential according to the remaining capacity. [138] presented a simple model for open-circuit potential determination. With this model, it is possible to calculate the battery potential with respect to the current being drawn. Lately, [44] derived the model equations to calculate the rate of discharge for a constant-power.

In this study, a path planning algorithm is proposed to find an optimal path between a chosen origin and destination allowing both changes in course and altitude. This optimization is performed by an unique algorithm that simultaneously process several factors, some of which are novel and others that are normally individually studied by the literature. These factors include: the icing protection system usage, which is a very novel solution that enables sUAS to fly under icing conditions; horizontal wind, that is a major issue on sUAS operations and has only recently been studied; terrain profile, that is a fundamental factor that has already been included in many studies; the aircraft performance model, which brings more realistic and accurate calculations of the propulsion required power according to the aircraft platform and environmental parameters; and battery discharge properties, which is a relevant factor as sUAS are typically powered by electric batteries and the discharge rates vary according to the remaining capacity. Therefore, this work contributes to the field by proposing a tool that can be used to plan the sUAS mission and to evaluate the different possible scenarios, in order to assist the decision making. In addition, to demonstrate its applicability, this work also brings the analysis of the proposed solution for a mission scenario using real sUAS platform parameters and real terrain and weather data.

3.2 Aircraft performance model

In this chapter the aircraft performance model is presented with the equations required for the calculation of the required power to propel the aircraft in given

atmospheric conditions and for a desired maneuver.

3.2.1 Pressure

The pressure (p in [Pa]) is calculated from the aircraft altitude by using the barometric formula with subscript 0, that is valid from sea level up to 11000 m of altitude:

$$p = p_0 \left[\frac{T_0}{T_0 + L_0(h - h_0)} \right]^{\frac{g_0 M}{R L_0}} \tag{3.1}$$

where h is the altitude in [m], p_0 is the standard pressure at sea level of 101325 Pa, T_0 is the standard temperature at sea level of 288.15 K, L_0 is the standard temperature lapse rate for subscript 0 of -0.0065 K/m, h_0 is the altitude at sea level of 0 m, R is the molar gas constant of 8.314472 $\text{Jmol}^{-1}\text{K}^{-1}$, M is the molar mass of Earth's air of 0.0289644 kg/mol and g_0 is the gravitational acceleration at sea level of 9.80665 m/s^2. The values of the constants are taken from the International Standard Atmosphere (ISA) mean sea level conditions [106].

3.2.2 Air Density

The density of air (ρ in $[\text{kgm}^{-3}]$) is an atmospheric property which significantly affects the aerodynamic forces. To calculate the air density, the ideal gas law is used:

$$\rho = \frac{p}{R_d T}, \tag{3.2}$$

where p is the pressure in [Pa] given by Eq. 3.1, T is the air temperature in [K] and R_d is the specific gas constant for dry air of 287.058 $\text{Jkg}^{-1}\text{K}^{-1}$.

3.2.3 Power Required

For steady, unaccelerated flight, the power required is calculated through:

$$P_{req} = (D + W sin(\theta)) v_a \tag{3.3}$$

where P_{req} is the required propulsive power in [W], v_a is the airspeed in [m/s], D is the drag force in [N] given by Eq. 3.4, W is the aircraft weight in [N] and θ is the climb angle in [rad].

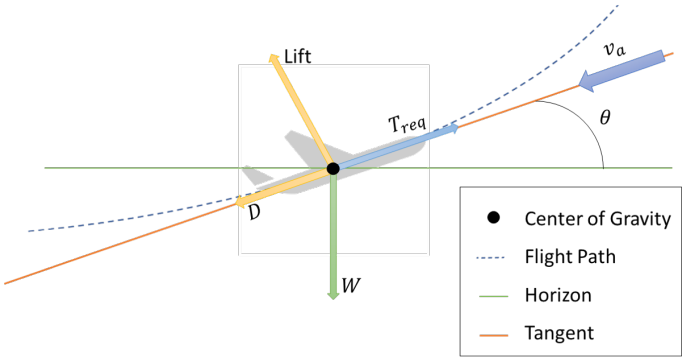

Figure 3.1: 2-D representation of an aircraft in a straight flight.

Hence, when the aircraft is cruising (θ is equal to zero), this results in $sin(\theta)$ being equal to zero. In this case, the weight is normal to the drag force and tangent to the lift. As the drag force is dependent on the body's size (e.g. the wing surface), the air density and the airspeed, the equation for drag force D is derived by dimensional analysis following the Buckingham's π-Theorem:

$$D = 0.5\rho v_a^2 S C_D \tag{3.4}$$

where ρ is the air density in [kgm^{-3}] given by Eq. 3.2, v_a is the airspeed in [m/s], S is the wing surface area in [m^2] and C_D is the drag coefficient, given by Eq. 3.7. For an aircraft equipped with propellers, the motor's required power (P_{req}) is obtained dividing the required propulsive power by the propeller efficiency (η_p):

$$P_{req} = \frac{P_{shaft}}{\eta_p}. \tag{3.5}$$

For a pure descent slope, for which no propulsion power is required, the aircraft's motor is assumed to be completely shut off and the on-board systems, except for the icing protection systems, are assumed to use insignificant amounts of energy. Therefore, the energy consumption in this case is assumed to be equal to the energy consumption of the icing protection requirements. However, the maximum descent angle needs to be chosen so that sufficient lift is provided for airspeed values that are in the range of predefined accepted values of the desired airspeed.

Aerodynamic Coefficients

To be able to calculate the drag force, which characterizes the power required to propel the sUAS, it is necessary to first calculate the drag and lift coefficients

(C_D and C_L respectively). In common A-to-B missions the aircraft is expected to primarily be flying in a horizontal straight flight, and performs a limited amount of turns. These turns depend on the path optimization, however the turns denote on a relatively small part of the entire path. Therefore, the effects of turns (circling flights) are not considered in the following calculations. This holds valid for "A-to-B" missions, and not for other mission types, such as loitering.

In addition, and with respect to the mission profile, the aircraft is assumed to follow a steady motion flight path, trust angle is zero, and the angle of attack is small, typically ranging between -4 and 10 deg. The lift coefficient for straight flight is given by [53] as:

$$C_L = \frac{2W\cos(\theta)}{\rho S v_a^2}, \tag{3.6}$$

where v_a is the airspeed in [m/s], W is the aircraft weight in [N], θ is the climb angle in [rad], ρ is the air density in [kgm^{-3}] given by Eq. 3.2 and S is the wing surface area in [m^2].

In this study, the drag coefficient (C_D) as a function the lift coefficient (C_L) was derived by a curve fitting process that aims to find a polynomial equation that represents the drag polar, typically acquired from wind tunnel experiments or Computational Fluid Dynamics (CFD) simulations. To derive a valid polynomial equation, it is necessary to first define the range of the lift coefficient where the equation will be valid. This domain can be calculated by finding the lowest and highest lift coefficient ($C_{L_{min}}$ and $C_{L_{max}}$), respectively, for the mission and aircraft constrains, such as minimum and maximum accepted airspeed (v_a), minimum and maximum accepted climb angle (θ) and minimum and maximum air density (ρ). C_D is therefore a function of C_L:

$$C_D = f(C_L), \tag{3.7}$$

where f is the fitted function.

3.2.4 Ground speed

The airspeed is defined as the speed of the aircraft with relation to the mass of air in which it is flying. In this research, the airspeed is considered tangent to the aircraft's heading. Therefore, when the aircraft climbs or descends, it is possible to calculate the projection of the airspeed on the horizontal axis (Fig. 3.2), with the assumption of the absence of vertical wind, by:

$$v_h = \sqrt{v_{h_x}^2 + v_{h_y}^2}, \tag{3.8}$$

with x and y components of the horizontal airspeed (v_h) given by:

$$\begin{aligned} v_{h_y} &= v_a \cos(\psi)\cos(\theta), \\ v_{h_x} &= v_a \sin(\psi)\cos(\theta), \end{aligned} \tag{3.9}$$

where v_a is the airspeed in [m/s], ψ is the heading in [rad] (Eq. 3.11) and θ is the climb angle in [rad].

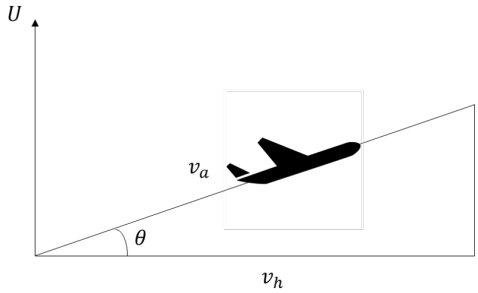

Figure 3.2: Representation of side view of the aircraft.

The presence of wind affects the aircraft's travelled trajectory (Fig. 3.3). The travelled trajectory is subject to the aircraft's ground speed (v_{gs} in [m/s]), which is the aircraft's speed relative to the ground and calculated by:

$$v_{gs} = \sqrt{(v_{h_x} + v_{wind_x})^2 + (v_{h_y} + v_{wind_y})^2}, \tag{3.10}$$

where v_h is the horizontal airspeed in [m/s] and v_{wind} the wind speed in [m/s].

The heading (ψ) is the direction where the aircraft points to, given by:

$$\psi = \chi - \arcsin\left(\frac{v_{wind}}{v_a \sin(\psi_{wind} - \chi)}\right), \tag{3.11}$$

where the course (χ in [rad]) is the travelled direction relative to the ground, with the wind speed given by:

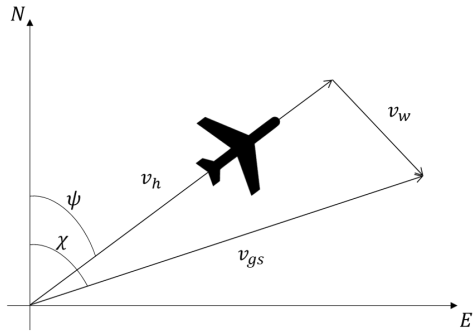

Figure 3.3: Wind triangle in coordinated flight.

$$v_{wind} = \sqrt{v_{wind_x}^2 + v_{wind_y}^2}, \tag{3.12}$$

and with the wind heading (ψ_{wind} in [rad]) given by:

$$\psi_{wind} = \arctan2(v_{wind_x}, v_{wind_y}). \tag{3.13}$$

3.3 Battery performance model

Modern electric batteries have become dominant power sources within sUAS, mainly because of their simplicity, and relatively high peak power output. Common battery types, such as lithium-based cells, are rechargeable and durable, which makes them suitable for sUAS operations. Electric batteries' energy potential changes according to the remaining capacity. [53] modelled the battery potential (V_{oc} in [V]) based on [138] as (Fig. 3.4):

$$V_{oc} = V_o - \left(\frac{\kappa C_{cut}}{C_{cut} - C}\right) + Ae^{-BC}, \tag{3.14}$$

where C_{cut} is the capacity discharged at cut-off in [Ah], C is the capacity discharged in [Ah], $A = V_{full} - V_{exp}$ and $B = 3/C_{exp}$ where V_{full} is the fully charged potential in [V]. Additionally, V_{exp} is the potential at the end of the exponential range in [V], and C_{exp} is the capacity discharged at the end of the exponential range in [Ah], with the Polarization Voltage (κ in [V]):

$$\kappa = \frac{(V_{full} - V_{nom} + A(e^{-BC_{nom}} - 1))(C_{cut} - C_{nom})}{C_{nom}}, \tag{3.15}$$

where V_{nom} is the potential at the end of the nominal range in [V], C_{nom} is the capacity discharged at the end of the nominal range in [Ah], and with battery constant potential (V_o in [V]):

$$V_o = V_{full} + \kappa + (R_C I_{eff}) - A, \tag{3.16}$$

where R_C is the internal resistance in [Ohms] and I_{eff} is the effective discharge current in [A].

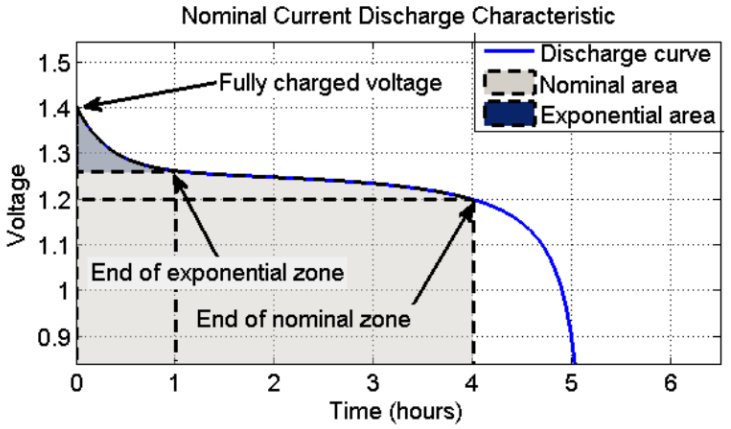

Figure 3.4: Battery discharge curve. (Source: [138])

In this study, the power is considered constant during the discretization step, and, therefore, the effective discharge current is the variable to be calculated. As a result, the Trembley's equations were manipulated to accommodate obtaining the effective discharge current for a given power. From Ohm's law, the effective current (I_{eff} in [A]) is given by:

$$I_{eff} = \frac{P_{eff}}{V_{oc}}, \tag{3.17}$$

with the potential (V_{oc} in [V]) being obtained by solving the nonlinear equation:

$$V_{oc}^{n+1} - \left(V_{full} + \kappa - A - \frac{\kappa C_{cut}}{C_{cut} - C} + Ae^{-BC} \right) V_{oc}^{n} - R_C I_{rated}^{1-n} P_{eff}^{n} = 0, \tag{3.18}$$

where n is the battery-specific Peukert's constant and I_{rated} is the maximum battery rated current in A.

Note that to obtain the potential (V_{oc}), it is necessary to solve the nonlinear Eq. 3.18. The valid solution will be in the range from the cut-off potential (V_{cut}) to the fully charged potential (V_{full}).

3.4 Meteorological and elevation data

This work aims to allow sUAS operations in adverse weather conditions. Therefore, meteorological forecast data needs to be considered. This data is used in the calculation of the total aircraft energy consumption, as it affects the aircraft's in-flight performance. Additionally, the meteorological conditions define when the icing protection systems are to be used, and how much power is required to mitigate the adverse effects of aircraft icing. Finally, the elevation data is of importance as the path planning algorithm optimizes the sUAS' altitude, and therefore it is vital to ensure a minimum terrain clearance in the aircraft's planned path.

3.4.1 Meteorological parameters

In Table 3.1 the downloaded parameters are shown. The wind and air temperature parameters are implemented directly in the form that they were supplied in. Other parameters were modified due to unit compatibility for usage in the calculation of other parameters, as described in the following sub-sections.

Table 3.1: List of downloaded parameters.

Parameter	Description	Units
v_{wind_x}	Meridional wind in x direction	m/s
v_{wind_y}	Meridional wind in y direction	m/s
T	Air temperature	K
q	Specific humidity	kg/kg
LWC	Atmospheric cloud condensed water content or Liquid Water Content	kg/kg

Relative Humidity

The specific humidity parameter can be downloaded from the meteorological service. However, in this work, the parameter used in the calculations is not the specific humidity but the relative humidity. This is because the aircraft is assumed to be in icing conditions and turn on the icing protection system when the temperature is below 0 deg C and the relative humidity is over 0.99. Therefore, the relative humidity (H) needs to be calculated and it is given by [46]:

$$H = \frac{e_a}{e_{sat}} \tag{3.19}$$

with the vapour pressure (e_a in [Pa]):

$$e_a = \frac{qp}{0.622 + 0.378q} \tag{3.20}$$

where q is the specific humidity, p is the pressure in [Pa] given by Eq. 3.1 and with the saturated water vapour pressure (e_{sat} in [Pa]):

$$e_{sat} = 10^{\frac{0.7859+0.03477(T-273.16)}{(1+0.00412(T-273.16))}} + 2 \tag{3.21}$$

where T is the temperature in [K].

LWC and MVD

The "mass fraction of cloud condensed water in air" can be also referred as "liquid water content (LWC)". In the icing protection system regression model, the LWC is one of the input parameters to estimate how much power is required by the system. The regression model uses the LWC concentration in [gm^{-3}] but the downloaded parameter is the LWC mixing ratio in [kg/kg]. Therefore, to convert LWC mixing ratio (LWC_m in [kg/kg]) to LWC concentration (LWC_c in [gm^{-3}]), the gas law for dry air is used:

$$LWC_c = \frac{LWC_m p}{R_d T} \times 10^3, \tag{3.22}$$

where T is the temperature in [K], R_d is the specific gas constant for dry air of 287.058 Jkg^{-1}K^{-1}. and p is the pressure in [Pa] given by Eq. 3.1. The Water Droplet Median Volume Diameter (MVD in [μm]) is another parameter used to calculate the power required by the icing protection system. It is approximated by following [134] and given by:

$$MVD = \frac{3.672 + \mu}{\lambda}, \tag{3.23}$$

with the shape parameter (μ) given by:

$$\mu = min\left(\frac{1000}{N_c} + 2,15\right), \tag{3.24}$$

where N_c is the pre-specified droplet number of 100 cm^{-3} and with:

$$\lambda = \left[\frac{\pi}{6}\frac{\rho_w N_c}{LWC_c}\frac{\Gamma(\mu+4)}{\Gamma(\mu+1)}\right]^{\frac{1}{3}}, \tag{3.25}$$

where Γ is the gamma function, ρ_w is the density of water of 1 gm^{-3} and N_c is equal to 100x10^{-6} m^{-3}.

Meteorological data download

The Norwegian Meteorological Institute hosts a webapp called THREDDS Data Server, where it is possible to have access to weather forecasts of several meteorological parameters. One of the services is the MetCoOp Ensemble Prediction System (MEPS) [101], from where the parameters used in this work were downloaded. This service provides data for the Scandinavian region with horizontal resolution of 2.5 km and from around 0.00986 to 0.99851 atm pressure levels (that can be converted to altitude) divided into 65 not equally spaced values. In the MEPS service, raw and post processed data are available for 10 ensemble members (set of forecast simulations) and for up to 66 hours of forecast. The models are run every 6 hours (00,06,12,18 UTC) and the first data file (00) is the most complete one and the only file containing all the necessary parameters for the development of this work. Therefore, the 00 file was downloaded for the esemble member 0 (mbr0) and the data from the forecast time slot 0 was used in the simulations. The time slot 0 reflects the instant information of the chosen date/time while the other time slots are hourly forecast.

The files are available in the Network Common Data Form (NetCDF) format and each file is up to 200 GB. However, it is possible to select which parts to download by using the Open-source Project for a Network Data Access Protocol (OPeNDAP). Therefore, the selected parameters can be downloaded only for the region of interest and for the desired pressure levels (altitudes).

3.4.2 Elevation data

The elevation data was downloaded from the Norwegian national website for map data (geonorge.no). Geonorge provides a catalog with a wide variety of map products, including elevation maps. These elevation maps are in the form of Digital

Terrain Model (DTM) or Digital Surface Model (DSM) and can be visualized in the website or downloaded via WCS or WMS services. In this work, the DTM was used, which is available with 1 m and 15 m of resolution for the regions correspondent to UTM32, UTM33 and UTM35.

Elevation data download

To download the data with the WCS service, the web browser can be used as the WCS client. Therefore, the data is requested via HTTP through URL parameters. The commands to be used are: GetCapabilities; DescribeCoverage; and GetCoverage. The first one returns all service-level metadata and a brief description, the second one returns the full description and the third one returns the data itself. The URL parameters varies according to the product and are usually described in the information obtained by the GetCapabilities and DescribeCoverage commands.

3.5 Path Planning

The goal of this work is to find an optimum three dimensions path minimizing the energy consumption of a long range sUAS flight from an origin to a destination in adverse weather conditions. To achieve this an optimization technique is used to minimize a given cost function.

3.5.1 Optimization technique

In this study the Particle Swarm Optimization (PSO) [34] technique is used to minimize the cost function and therefore find the optimum path. PSO is a meta-heuristic optimization method where the particles (solutions) are updated every iteration based on the best global and local solutions. In this study the standard PSO was used with a modification to reduce the maximum absolute particle velocity by an ϵ factor. This was implemented to keep the search more local, and thereby avoiding too large movements in the solution domain per iteration, as it may be expected that the optimum solution is relatively close to the straight line path.

3.5.2 Optimization algorithm

The algorithm's block diagram is shown in Fig. 3.5. The orange blocks scenario-based input parameters, such as the meteorological and elevation data, the origin and destination, the number of control inputs and the PSO parameters. The other boxes outside the blue box are part of the pre-processing phase when the model is created and the initial solutions are generated.

The blue box contains the optimization loop. First the candidate solutions are evaluated with respect to the terrain. If part of the path is under terrain, the solution is discarded ($cost = \infty$). If not, the optimization will evaluate the icing conditions for each discretization step i.

If icing conditions are present in the step i ($H_i > 99\%$ and $T_i < 0degC$), the deice and anti-ice required power are calculated (P_{deice_i} and $P_{anti-ice_i}$, respectively). For the deicing operations the engine's required power is calculated with an updated drag coefficient ($C^*_{D_i}$), which constitutes the average icing penalty, and therefore an updated required propulsive power $P^*_{req_i}$. For the anti-ice operations the aircraft's wings are kept clear from icing. Therefore the engine's required power is the same as without ice (P_{req_i}). However, the anti-icing system does require thermal energy. In this study the anti-icing system uses the main battery as power source (i.e. does not have a separate power source), and therefore induces a performance penalty during usage. The total power required by the deice and anti-ice systems, including the respective engine's required power, are compared and the solution that requires the least total power is chosen. If there are no icing conditions present the total required propulsion power remains unchanged (P_{req_i}).

The next step is to calculate the battery energy consumption in the step i taking into consideration the battery model and how much battery capacity is left. Finally, the total battery energy consumption is calculated by summing the battery energy consumption times the flight time of all steps. The total battery energy consumption is, therefore, used to update the particles' position in the domain. The new solutions are then evaluated. This process repeats for the chosen total number of iterations.

3.5.3 Cost Function

The aim of the optimization algorithm is to minimize a cost function (Eq. 3.26), which represents the total energy consumption and is calculated by the sum of the battery discharge rate ($\dot{C}$ in [Ah/s]) in each discretization step, multiplied by the time in each discretization step:

$$minimize\, C_{tot}(\dot{\mathbf{C}}, \mathbf{t}) = \sum_{i=1}^{N} \dot{C}_i t_i \tag{3.26}$$

where $\dot{\mathbf{C}}$ and $\mathbf{t}$ are the vectors with all $\dot{C}_i$ and t_i, respectively. C_{tot} is the total discharged capacity in [Ah], i is the index of the discretization step, N is the number of discretization steps in the path, t_i is the time in [s] at the i-th step given by:

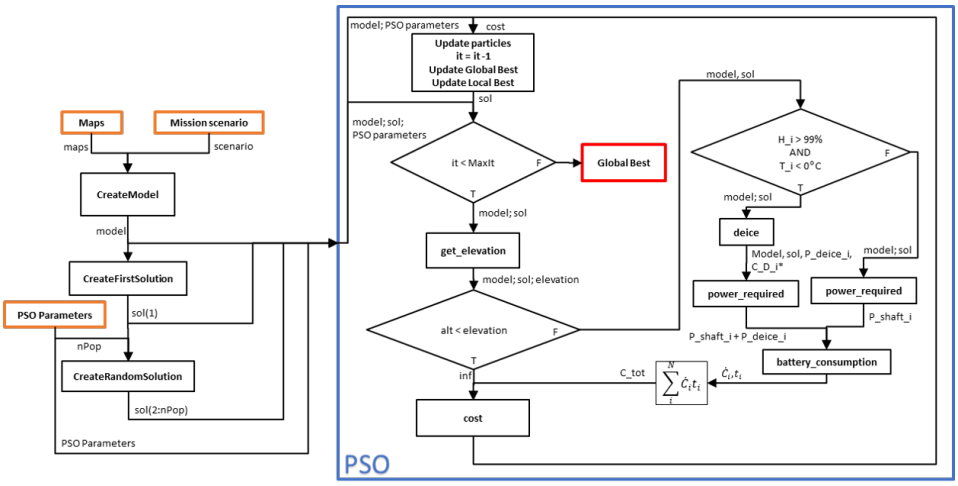

Figure 3.5: Algorithm block diagram.

$$t_i = L_{step}/v_{gs_i}, \tag{3.27}$$

where v_{gs_i} is the ground speed in the discretization step i in [m/s] given by Eq. 3.10, with the step's length (L_{step} in [m]) given by:

$$L_{step}(L) = \frac{L}{N}, \tag{3.28}$$

and with the total length of the path (L in [m]) given by:

$$L(\mathbf{x}, \mathbf{y}) = \sum_{i=1}^{N} \sqrt{(x_{i+1} - x_i)^2 + (y_{i+1} - y_i)^2} \tag{3.29}$$

where x_i and y_i are east and north positions in the ENU frame and i is the index of the discretization step.

The the rate of discharge ($\dot{C}$ in [Ah/s]) given by:

$$\dot{C}_i = \frac{I_{tot_i}}{3600}, \tag{3.30}$$

with the total current (I_{tot} in [A]) given by:

$$I_{tot_i} = \frac{P_{tot_i}}{V_{oc_i}}, \tag{3.31}$$

where V_{oc} is the battery's potential in [V] (Eq. 3.18) and with the total required power (P_{tot} in [W]) given by:

$$P_{tot} = P_{req}, \tag{3.32}$$

if there are not icing conditions occurring, or

$$P_{tot} = P^*_{req} + P_{deice}, \tag{3.33}$$

when there are icing conditions occuring, and the deice solution is the one requiring the least power, or

$$P_{tot} = P_{req} + P_{anti-ice} \tag{3.34}$$

if there are icing conditions, while the anti-ice solution requires the least power. Here, P_{req} is the engine's required power in [W] (Eq. 3.3), P^*_{req} is the engine's required power when using the deice solution in [W] (Eq. **??**), $P_{anti-ice}$ is the anti-ice solution required power in [W] and P_{deice} is the deice solution required power in [W]. Finally, C_i is the total capacity discharged in [Ah] until instant i and given by:

$$C_i = \sum_{i=0}^{i} \dot{C}_i t_i, \tag{3.35}$$

where $\dot{\mathbf{C}}_i$ is the vector of $\dot{C}$ from $\dot{C}_0$ to $\dot{C}_i$ and $\mathbf{t}_i$ is the vector of t from t_0 to t_i. C_0 is the initial discharged capacity.

Note that when parts of the path are not above the terrain, or if the total energy consumption is higher than the battery's capacity, this candidate solution receives an infinite penalty to ensure it is disregarded as a candidate solution.

3.5.4 Control inputs

The required control inputs are horizontal plane waypoints (x,y), airspeeds (v_a) and climb angles (θ). The number of waypoints (O) and airspeeds/climb angles

(K) are chosen by the user when defining the scenario. Note that the airspeed and climb angle changes were chosen to occur at the same time for algorithm simplicity.

3.5.5 Model and Mission Parameters

ENU frame

The ENU frame was chosen as the coordinate system of the optimization algorithm. Therefore, all information in World Geodetic System 1984 (WGS84), which is in the format of latitude, longitude and altitude, must be converted to the ENU frame. Also, the resulting waypoints of the optimized solution must be converted to WGS84 in order to be fed into the sUAS' flight control system. In this work, when using the ENU frame, the x axis points east, the y axis points north and the z axis points up. It is also necessary to define the origin (0,0,0) of the ENU frame. As the region around the origin is less affected by the frame conversion error, the origin was chosen to be in the geographical midpoint between origin and destination at sea level.

Domain

The candidate solutions' waypoints are limited to be away from the straight path up to a maximum distance. This maximum distance was defined as one third of the length of the straight path between the origin and destination. Therefore, the optimization algorithm can only find candidate solutions containing waypoints within this domain region.

The boundaries of airspeed (v_a) and climbing angle (θ) must also be defined according to the aircraft platform's constraints. In addition, these boundaries should be fine tuned for values around the expected optimization resulting values, in order to achieve faster convergence.

Discretization strategy

The cost function (Eq. 3.26) is evaluated for each discretization step of the path and the total cost is the sum of the energy consumption in each step. Therefore the number of steps will affect the resolution of the optimization algorithm, and the processing time. The number of discretization steps (N) is defined by the multiplication factor (F) and the number of airspeed and climb angle changes (K):

$$N = KF - 1 \tag{3.36}$$

These parameters are presented for a scenario example in Fig. 3.6. In this example, A is the origin and B is the destination. There is one waypoint between origin and destination ($O = 1$). There are three airspeed and climb angle changes ($K = 3$), and three of multiplication factor ($F = 3$). Therefore there are eight discretization steps (N).

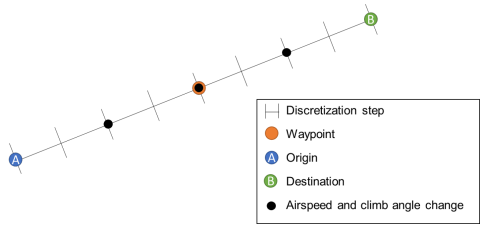

Figure 3.6: Example of a path and its division.

Additionally, the first particle in the PSO algorithm has to be initiated with a candidate solution. A good candidate initial solution for the first particle is a straight path from origin to destination, climbing with constant climb angle to the altitude a few meters above the highest peak, then cruising close to the destination, and finally descending with constant negative climb rate to the destination.

Also, the other particles (candidate solutions) of the population must be initiated. To not distract the optimization algorithm from the region around the first candidate solution, which is expected to contain an optimal solution, the particles are chosen to be variations of the first particle following the exponential probability distribution. Therefore, the values of the set of variables of the other particles are close to the values of the first initial solution set of variables.

3.6 Case study

In this section, the chosen mission case and operational profiles that were evaluated are described, and the aircraft and battery parameters used in the optimization algorithm are explained.

3.6.1 Aircraft platform

The P31016 (Fig. 3.7) is a small battery-powered aircraft that is powered by a 6.0 kilowatt brushless motor. The propulsion efficiency (η_p) is assumed constant at 50% with discharge parameters as specified in the next section. The aircraft has a wing surface (S) of 0.81 m^2 and has a typical mission-ready weight of 171.5 N (W).

Figure 3.7: P31016 concept battery-powered fixed-wing unmanned aircraft

Based on the aircraft flight envelope, the airspeed (v_a) was set ranging from 20 m/s to 30 m/s, and the climb angle (θ) ranging from -10 to 10 degrees. Considering the aircraft performance these limits were chosen to avoid the optimization algorithm explores too high climb angles and airspeed.

The aircraft performance data was generated with the flow solving module FENSAP, which is part of FENSAP-ICE [6]. Three-dimensional CFD simulations were performed on the P31016 (Fig. 3.7) at Reynolds number (Re) of 1.2×10^6 with angles of attack (AOA) corresponding to the set envelope limitations and using a numerical setup described in Table 3.3. The results for drag and lift of the P31016 are presented in Fig. 3.8. The simulations indicate that the flow separation starts from the trailing-edge at AOA of 8 deg. Drag forces increase unproportionally after the onset of stall, whereas lift is decreased as the separation intensifies with higher AOAs.

This data was used to fit the drag polar curve (Fig. 3.9). The curve was fitted for a lift coefficient range calculated based on the aircraft and mission constrains. These constrains are: minimum and maximum airspeed (v_a), minimum and maximum climb angle (θ) and minimum and maximum air density (ρ). The air density was calculated according to the minimum and maximum expected relative humidity (H), temperature (T) and pressure (p) in the meteorological data. The minimum and maximum resulting lift coefficient for these constrains were 0.3436 and 1.0371 respectively. The fitted curve of the drag polar for this range is given as:

$$C_D = 0.1407C_L^2 - 0.07989C_L + 0.02496, \tag{3.37}$$

where C_L is the lift coefficient and C_D is the drag coefficient.

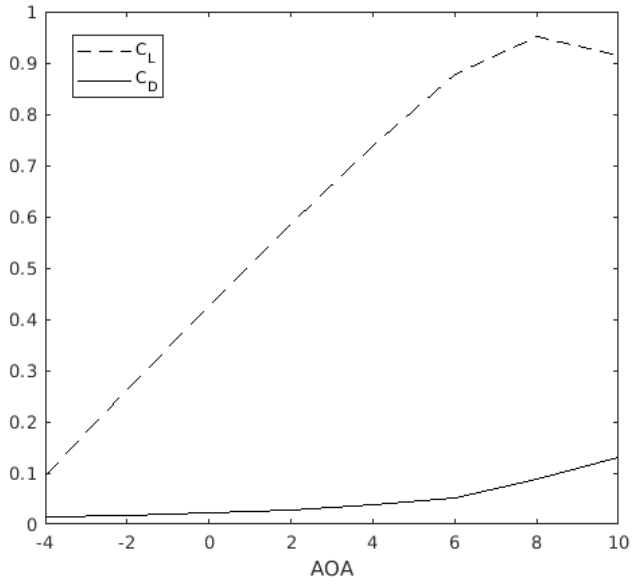

Figure 3.8: AOA (Angle-Of-Attack) vs C_D and C_L from CFD simulations

3.6.2 Icing protection System model

The power requirements for de-icing and anti-icing, as well as the performance penalties during de-icing are generated using numerical simulation methods. Two icing codes are used for this. LEWICE is an icing code that has been developed by NASA over several decades for general aviation [150]. It is a widely validated code [151], but it has been shown that there may be limitations for the application of small UAS [63] [64]. The code is based on a panel-method, that can simulate ice accumulation, anti-icing, and de-icing with very low computational resources. ANSYS FENSAP-ICE is an icing code using modern computational fluid dynamics (CFD) methods [58]. The code is very flexible and has in the past been used for UAS applications [59] but still lacks a dedicated validation for icing at small Reynolds numbers [65].

In this work, the LEWICE is used to generate a model for the anti-icing and de-icing loads, whereas FENSAP-ICE is used for the de-icing performance penalties. The low computational requirements of the panel-method of LEWICE allow to simulate a large number of different meteorological icing conditions in short time, in the order of minutes on a typical desktop computer. The same computations would take several days on a high-performance computing (HPC) cluster with FENSAP-ICE.

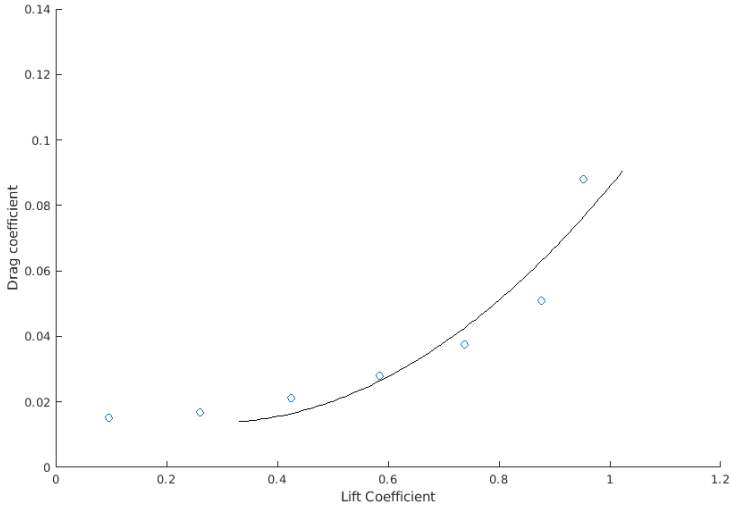

Figure 3.9: Drag polar fitted curve

A total of 112 different icing cases have been simulated with LEWICE to generate a dataset for anti-icing with LEWICE. The boundary conditions of the meteorological cases are based on the icing envelope of 14 CFR Part 25, App. C [38] used for the airworthiness certification of commercial aircrafts. The simulation cases cover the intermittent maximum (IM) icing and continuous maximum (CM) icing envelope. The range of values for each icing parameter is shown in Table 3.2. Simulations were performed in 2D using the mean aerodynamic chord (MAC = 0.275 m) of the wing. For all simulation it was assumed that only 20% of the leading-edge area of the lifting surfaces was protected (surface temperature of +5 deg C). Runback icing, generated by the refreezing of melted ice from the heated zones, was not included in this study. This was done for reasons of simplification and lack of dedicated studies of runback icing on UAS. Runback icing itself may be a significant source of aerodynamic performance degradation of any IPS [148].

Table 3.2: Range of values for each icing parameter

Parameter	**Range of values**
Airspeed	[20, 30, 40, 50] m/s
Angle of attack AOA	[0] deg
Chord c	[0.275] m
Temperature T_C	[-2, -5, -10, -30] deg C
Median (droplet) volume diameter MVD	[15, 20, 30, 40] μm
Liquid water content LWC concentration	[0.04 ... 2.82] gm^{-3}

The de-icing power requirements have been assumed to be 60% lower than the anti-icing loads. In contrast to the anti-icing, the minimum power requirement for de-icing can not be directly simulated with a steady-state assumption. This means that transient simulations that prescribe a power supply to the leading-edge is required. Such simulations were carried out with LEWICE and confirmed that the aforementioned assumption provides sufficient power for successful de-icing. It should be noted however, that this assumption is a gross simplification, but is deemed sufficient for the purpose of this work.

The 112 simulation cases from LEWICE for the anti-icing and de-icing power requirements ($P_{anti-ice}$ and P_{deice}, respectively) were used to generate linear models that are used for the path-planning optimization. Forth order linear regression models were used and have been found to be able to predict the power loads depending on airspeed (v_a in [m/s]), temperature (T_C in [deg C]), Liquid Water Content concentration (LWC_c in gm^{-3}) and Median Volume Diameter (MVD in [μm]) with good accuracy (R^2= 0.977).

The data for the de-icing performance degradation was obtained with FENSAP-ICE in 2D and then extrapolated for the entire aircraft. First, 90 s of ice accretion were simulated with FENSAP-ICE with the numerical parameters specified in Table 3.3. The degradation of lift and drag was then averaged over a full de-icing cycle of 120 s. Again the 14 CFR Part 25, App. C icing envelopes (CM & IM) were applied. In order to reduce the number of simulations, only the cruise velocity of 25 m/s and a single MVD of 20 μm was considered.

Table 3.3: Numerical parameters setup

Parameter	**Setup**
Flow conditions	Steady-state, fully turbulent
Turbulence model	Spalart-Allmaras
Droplet distribution	Monodisperse
Artificial	Second order
Viscosity	Streamline upwind

The aerodynamic degradation occurring during de-icing is presented in Fig. 3.10. A linear model (Eq. 3.38) was selected for the drag (R^2 = 0.81).

$$C_D^* = C_D + C_D(0.0785\, LWC_c + 0.4973). \tag{3.38}$$

Therefore, the required power to propel the aircraft when the de-icing solution is used needs to be calculated using the degraded drag coefficient (C_D^*):

$$P^*_{req} = \frac{(0.5\rho v_a^2 S C^*_D + W sin(\theta))v_a}{\eta_p}. \tag{3.39}$$

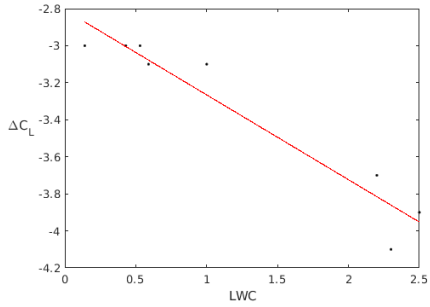

(a) LWC [gm^{-3}] vs ΔC_L [%]

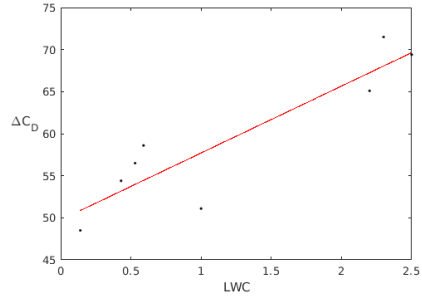

(b) LWC [gm^{-3}] vs ΔC_D [%]

Figure 3.10: Degradation on lift and drag.

Battery parameters

The P31016 is assumed to be equipped with a commercial 10-cells LiPo battery with 26.4 Ah capacity (C_{cut}). Following Tremblay's model, the potential parameters of a 10-cells LiPo battery are approximately: 41.8, 39.67 and 37.67 ampere-hour of fully charged (V_{full}), end of exponential range (V_{exp}) and end of nominal range (V_{nom}) respectively. The capacity parameters are approximately: 2.64 and 20.4 ampere-hour of end of exponential range (C_{exp}) and end of nominal range (C_{nom}), respectively. In addition, from the battery's manual it is found that the internal resistance (R_c) is 0.015 Ohms and the maximum rated discharge current (I_{rated}) to be 660 ampere. The potential curve of this battery with respect to the capacity discharged for 10 ampere of constant current is shown in Fig. 3.11.

Note that for all cases, the battery was assumed to be fully charged in the beginning of the mission. Therefore, C_0 (the initial capacity discharged of the battery) was assumed to be equal to 0 Ah.

3.6.3 Mission Case

The region of Northern Norway was chosen for the evaluation of the proposed solution. The meteorological and elevation data were obtained for the area of the white rectangle of Fig. 3.13. In this area, one mission case was defined to be investigated and the weather of the date of 20th of January of 2019 was chosen as the reference weather. For this area and date, the parameters of liquid water content concentration (LWC_c in [gm^{-3}]) and temperature in deg C are related as shown in Fig. 3.12 if icing conditions are met.

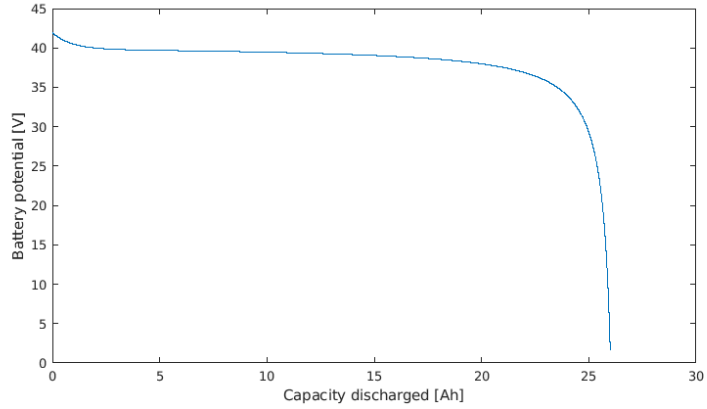

Figure 3.11: Battery potential versus capacity discharged

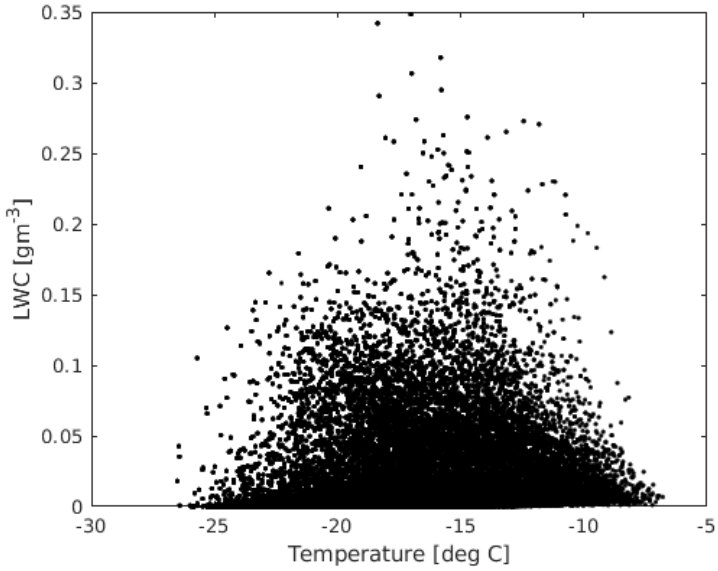

Figure 3.12: LWC_c and temperature distribution.

Operational Profiles

For the mission case, twelve different operational profiles (OP) were evaluated as described below.

Note that all the operational profiles start at 250 m of altitude, regardless of the altitude of the take off spot. Therefore, it is assumed that before starting the autopilot, the aircraft will be taken by the pilot to 250 m of altitude. Also, when

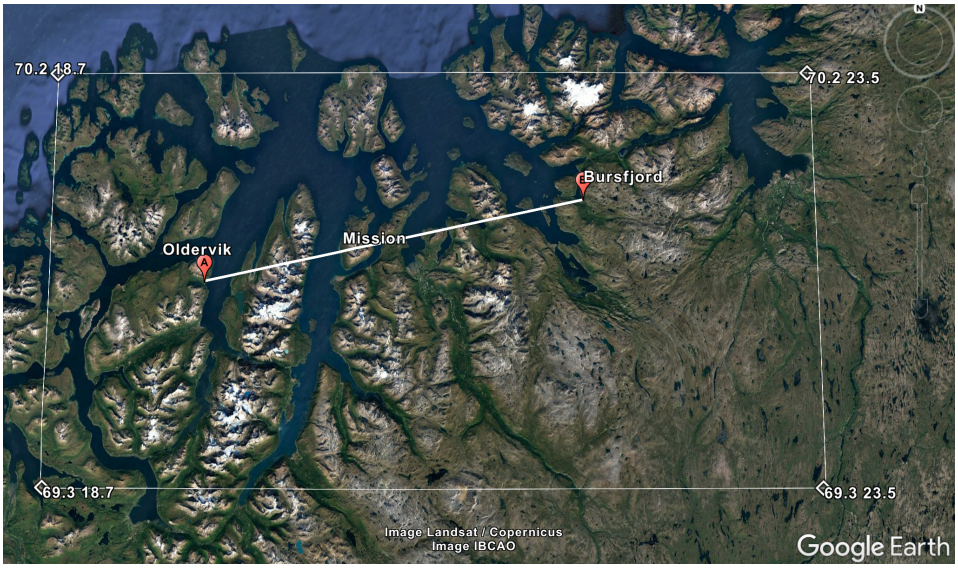

Figure 3.13: Mission case.

reaching the destination, the aircraft must be landed by the pilot. Take off and landing maneuvers are not considered in this work.

The straight path for the initialization is assumed to have constant airspeed of 28 m/s, which is around the value of the best cruise airspeed for the P31016.

- OP 01: Horizontal straight path between origin and destination, climbing to a few meters above the highest peak, flying at constant altitude until close to the destination, then descending until the destination. Evaluated under no icing conditions.
- OP 02: Optimized path without considering icing conditions. Evaluated under no icing conditions.
- OP 03: Optimized path considering icing conditions, using deice or anti-ice (best option) when needed. Evaluated under no icing conditions.
- OP 04: Optimized path considering icing conditions, using only anti-ice when needed. Evaluated under no icing conditions.
- OP 05: Horizontal straight path between origin and destination, climbing to a few meters above the highest peak, flying at constant altitude until close to the destination, then descending until the destination. Evaluated under icing conditions, using deice or anti-ice (best option) when needed.
- OP 06: Optimized path without considering icing conditions. Evaluated under icing conditions, using deice or anti-ice (best option) when needed.

- OP 07: Optimized path considering icing conditions, using deice or anti-ice (best option) when needed. Evaluated under icing conditions, using deice or anti-ice (best option) when needed.
- OP 08: Optimized path without considering icing conditions. Evaluated under icing conditions, using only anti-ice when needed.
- OP 09: Horizontal straight path between origin and destination, climbing to a few meters above the highest peak, flying at constant altitude until close to the destination, then descending until the destination. Evaluated under icing conditions, using only anti-ice when needed.
- OP 10: Optimized path considering icing conditions, using only anti-ice when needed. Evaluated under icing conditions, using deice or anti-ice (best option) when needed.
- OP 11: Optimized path considering icing conditions, using only anti-ice when needed. Evaluated under icing conditions, using only anti-ice when needed.
- OP 12: Optimized path considering icing conditions, using deice or anti-ice (best option) when needed. Evaluated under icing conditions, using only anti-ice when needed.

3.7 Results

Table 3.4 show the results for the mission case, where the sUAS flies from Oldervik to Bursfjord. In icing conditions, the operational profile seven has the lowest battery energy consumption (7.05 Ah), as expected. Compared to the operational profile one, which consumes 14.82 Ah of battery, it brings a reduction of 52.43 % on the battery energy consumption. Also, in this mission case, if only the anti-ice is used and the sUAS is flying straight (OP 09), the battery energy consumption is equal to 20.54 Ah, almost three times more than the optimized path that both deice and anti-ice are available. This is due to the absence of path optimization and to the fact that the anti-ice system requires more power.

In addition, if the path is optimized without taking the ice into consideration, the expected battery energy consumption is of 6.28 Ah (OP 02). However, if the sUAS actually experiences icing conditions during this flight, the battery energy consumption is of 10.74 Ah (OP 06), against 7.05 Ah when the path is optimized taking into consideration the weather forecast (OP 07). Therefore, this shows the importance of using the weather information to optimize the path.

All optimized paths were longer than the straight path. Also, the flight time was slightly longer in all cases. This is due to the fact the optimization takes the wind into consideration so it is able to change the path to find a better wind profile

Table 3.4: Mission case operational profiles results

	Straight	Opt. without ice	Opt. with anti-ice	Opt. with deice	Eval. with anti-ice	Eval. with deice	Battery Cons. [Ah]	Length [km]	Time [min]	Length in ice [km]	Time in ice [min]
OP 01	x						8.08	91.47	44.68	0.00	0.00
OP 02		x					6.28	91.82	45.59	0.00	0.00
OP 03			x	x			6.52	97.49	49.80	0.00	0.00
OP 04			x				6.65	94.84	50.36	0.00	0.00
OP 05	x				x	x	14.82	91.47	44.68	49.39	23.32
OP 06		x			x	x	10.74	91.82	45.59	34.89	16.27
OP 07			x	x	x	x	7.05	97.49	49.80	3.90	1.96
OP 08		x			x		14.32	91.82	45.59	34.89	16.27
OP 09	x				x		20.54	91.47	44.68	49.39	23.32
OP 10			x		x	x	7.09	94.84	50.36	3.79	1.71
OP 11			x		x		7.46	94.84	50.36	3.79	1.71
OP 12			x	x	x		7.48	97.49	49.80	3.90	1.96

and/or to change the airspeed accordingly. Therefore, the flight duration is longer but the battery energy consumption is lower.

Figure 3.14 shows the straight path (OP 05) and Fig. 3.15 the optimized path (OP 07) of the mission case. It is possible to notice that in the optimization, the path is optimized so that the ice is avoided when possible by placing it under or above the icing clouds (blue dots). Also, when close to the destination, the descent maneuver is started as soon as possible, so energy savings are enhanced.

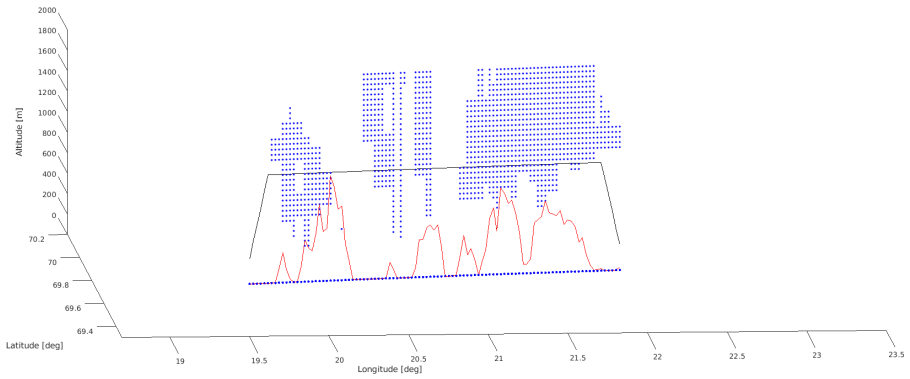

Figure 3.14: Straight path.

The two peaks on the battery consumption (Fig. 3.16) between 5 and 10 minutes and between 35 and 40 minutes are due to the icing conditions. In the first moment that the sUAS is flying under icing conditions, the power required by the deice system is 477 W and the increase on the power required to propel the aircraft is 184 W, totalizing 661 W. The increase on the propulsion required power is due to the drag coefficient penalty. If the anti-ice solution was used, where there is no penalty on the drag, the required power would be around 1150 W. Therefore,

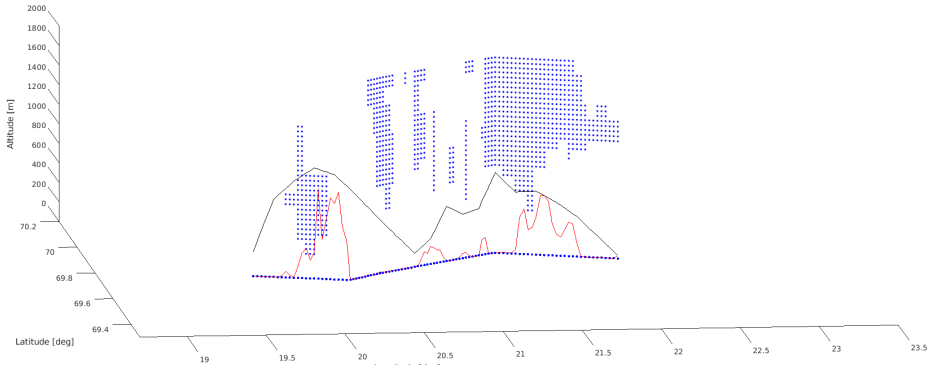

Figure 3.15: Optimized path.

the deice solution requires less power in total (deice system plus propulsion power). The predominance of the deice solution over the anti-ice will repeat in almost every case investigated in this work. This is due to the mission constrains and to the fact that, according to the deice and anti-ice regression models used in this work, the anti-ice will only have an advantage in maneuvers with high drag.

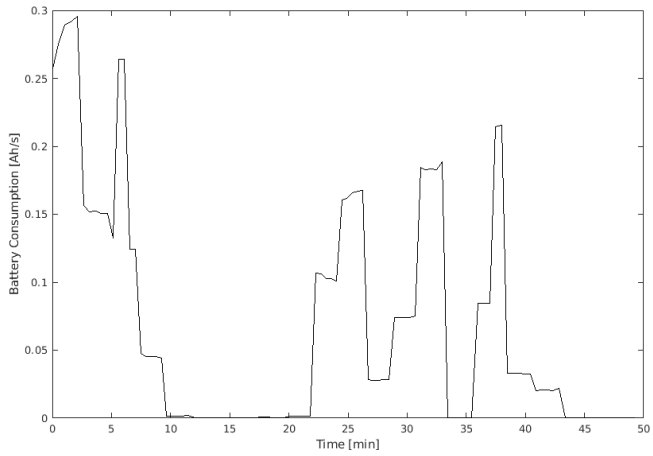

Figure 3.16: Battery Consumption.

Finally, Fig. 3.18 shows the optimized airspeed along the path (OP 07). It is possible to notice that the airspeed is kept around the known best cruise airspeed of the aircraft, which is around 28 m/s.

It should be noted that several simplifications have been applied to some of the simulation input of this study regarding the icing protection system and icing effects

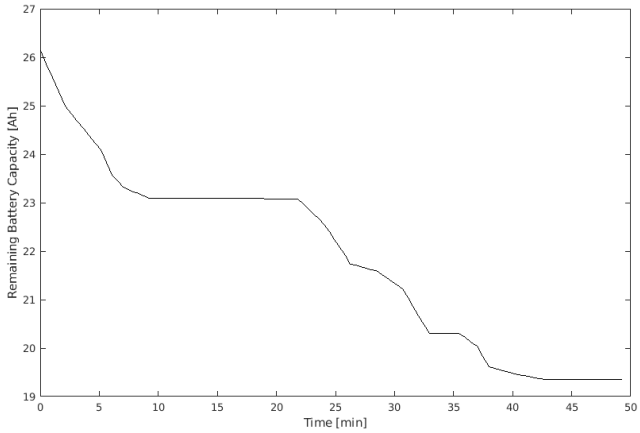

Figure 3.17: Battery Discharged.

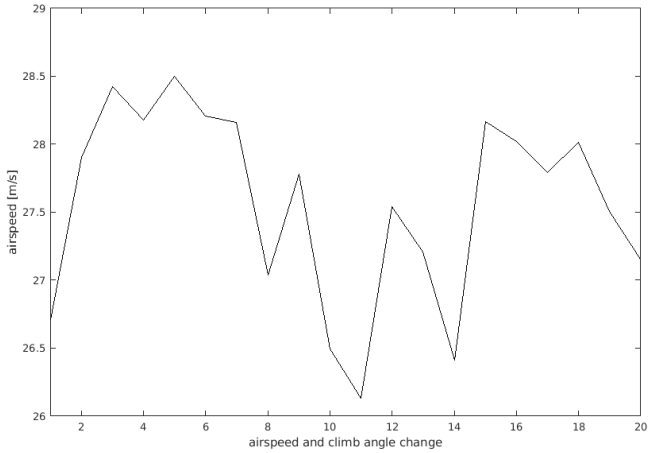

Figure 3.18: Airspeed of optimized path.

that may have a significant influence on the overall results:

- No runback icing effects
- Simplified de-icing load calculation
- Simplified simulation of the aerodynamic degradation during de-icing

These simplifications were introduced in order to limit the amount of expensive computational simulations. Since this work is focussing mostly on the path-planning method, these simplifications were considered sufficient for this study. For

future work, a greater level of detail can easily be included to the required input data.

3.8 Conclusion

This chapter presented a path-planning algorithm for small UAS equipped with icing protection systems. An aircraft performance model was used to calculate the power required to propel the aircraft. A battery model was also included in the calculations to give a more precise battery consumption. The goal of the algorithm was to find an optimum path that uses the least energy, taking into consideration the atmospheric parameters, such as wind, liquid water content, relative humidity and temperature of a given time. Climb/decent angles, airspeed and waypoints were the optimization variables. The investigated mission case was to fly between two towns in Northern Norway in a given date of the winter season. Twelve operational profiles were compared and the proposed solution, that takes the icing conditions into consideration when optimizing the path, achieved 52% of battery savings when compared to the standard straight path, proving itself to be a very useful solution for path-planning in icing conditions. In addition, it was verified that, for the sUAS used in this work, the deice solution will require less power to protect the sUAS from icing in the majority of situations, compared to the anti-ice solution.

Part II

Long-range Flight Performance and Safety

Chapter 4

Contingency Path Planning for Hybrid-electric UAS

This chapter presents a path planning optimization method which aims to mitigate the risks in the event of a critical engine or generator failure in hybrid-electric UAS. This is achieved through continuous determination of the optimum flight path, based on the remaining battery range and expected local wind conditions. The result is a dynamically adjusting flight path which ensures the aircraft to remain within range of pre-specified safe landing spots. The developed algorithm uses the Particle Swarm Optimization technique to optimize the flight path, and incorporates regional wind information in order to increase the accuracy of the expected in-flight performance of the aircraft.

4.1 Introduction

Hybrid-electric power trains used by long-range fixed-wing unmanned aerial vehicles often employ an internal combustion engine as the main source of power. It is witnessed that the internal combustion engine often is a critical point of failure. In such an event a functioning electric motor may still be able to propel the aircraft for a short period by utilizing the remaining battery capacity.

In an effort to contribute to the current scientific search towards path safety within autonomous decision-making, this chapter proposes a new method for contingent path planning optimization. The main goal of this study is to derive a method for autonomous path planning which ensures that the aircraft is able to reach a safe landing spot in the event of a critical engine or generator failure. This is done while taking into consideration the presence of expected local winds and their effect on the obtainable battery range. The resulting optimum path is found by applying

the technique of Particle Swarm Optimization (PSO) [34].

In recent scientific literature path planning algorithm methods are described which use local wind information. In [1], the author integrates the uncertainty of the wind field into the wind model, and uses a Markov Decision Process for path planning. The goal was to minimize the power consumption of the aircraft and minimize time-to-goal. A similar approach was chosen in [77], where the technique of Ant Colony Optimization (ACO) is used to find the path which minimizes the travel time considering the wind. However, as with most studies the wind is considered constant during the flight. The ACO is a bio-inspired metaheuristic optimization algorithm suchlike the Particle Swarm Optimization used in this study. PSO is widely used for path planning, such as described in [90], where the author uses the method to minimize the UAS path's length and danger based on the proximity of threats.

The study presented in this chapter builds further upon the before mentioned methods by incorporating a dynamic wind model and translating this into the real-time in-flight performance of hybrid-electric UAS.

4.2 Aircraft performance model

The resulting achievable flight range is described in the following subsections. This is illustrated by analyzing the different segments of a flight that suffers a critical engine or generator failure. The flight segments are divided into normal operations, battery-powered flight, and unpowered glide.

4.2.1 Aircraft Power Model

For a conventional propeller-driven aircraft in level and unaccelerated flight, the power that is required for obtaining the maximum flight range is expressed, in watts, by:

$$P_{rmr} = W \left(\frac{C_D}{C_L} \right)_{min} \cdot v_{TAS} \tag{4.1}$$

where W is the aircraft total weight in Newton, $(C_D/C_L)_{min}$ is the minimum obtainable ratio between the aerodynamic drag and lift coefficients, and v_{TAS} is the true airspeed occurring at the $(C_D/C_L)_{min}$ condition.

One advantage of utilizing a hybrid-electric power train is that there is the possibility of co-powering the main drive shaft (continuous or intermittent). Depending on the sizing of the hybrid system and mission specifications, this may prove to be

beneficial for the resulting range. A method for determining the achievable range in the case of co-powering of a hybrid system is described by Marwa in [95]. In the remainder of this analytical study it is further assumed that a functioning main generator set is sized so that it is capable of supplying the necessary power required for maintaining the maximum range cruise speed (v_{mr}). Therefore during cruise it is given that the necessary amount of co-powering by the electric motor is zero.

4.2.2 Aircraft range - Normal operations

In the case of a hybrid powered aircraft where the electric co-powering equals zero, the obtainable maximum range may be modelled similarly to conventional fuel-powered aircraft. The Breguet range equation is a commonly used first-order approximation to determine the achievable maximum range of a conventional propeller aircraft [39]. When assuming no wind and a parabolic drag polar, the resulting maximum range in normal operations (R_{no} in meters) is expressed by [3]:

$$R_{no} = \frac{\eta_{pg}}{c} \cdot \left(\frac{C_L}{C_D}\right)_{max} \cdot ln\left(\frac{W_0}{W_1}\right) \tag{4.2}$$

where η_{pg} is the complete propulsion efficiency of the hybrid system, c is the specific fuel consumption of the generator in Newtons per second per watt, W_0 is the aircraft's total weight at the beginning of the cruise flight, W_1 is the aircraft's total weight at the end of the cruise flight, and $(C_L/C_D)_{max}$ is the maximum achievable ratio between the aerodynamic lift and drag coefficients in level and unaccelerated flight.

4.2.3 Aircraft range - Battery-powered flight

In a situation where the main engine or generator fails, the hybrid system remains able to supply the power necessary to propel the aircraft by utilizing the remaining battery capacity. To obtain the performance model the aircraft is considered purely battery-powered. The adopted method for determining the maximum achievable range of battery-powered sUAS has previously been described in [72]. The adopted method in that study is an extension on the classical determination of battery-powered aircraft range, by including the Peukert effect on the battery capacity. This allows for a more accurate determination of the aircraft's battery range [31][136]. When assuming no wind and a parabolic drag polar, the maximum range (R_{bp}, in kilometers) for battery-powered sUAS in level and unaccelerated flight, without the influence of wind, is expressed by:

$$R_{bp} = \left(\frac{V \times C\,\eta_{pe}}{W\left(\frac{C_D}{C_L}\right)_{min}} \right)^{n} \left(\sqrt{\frac{2W}{\rho_\infty\, S\, C_L}} \right)^{1-n} \cdot {R_t}^{1-n} \cdot 3.6 \tag{4.3}$$

Here V is the battery bus voltage, C is the battery capacity, n is the battery-specific Peukert constant, R_t is the battery hour rating (i.e. the discharge period at which the rated capacity C was determined), and η_{pe} is the propulsion efficiency of the battery-powered system. The amount of experienced resistance depends on the specific set-up, and the availability of mitigation systems, such as mechanical decoupling.

4.2.4 Aircraft range - Unpowered glide

After the main batteries have been drained, the aircraft may be able to fly further by exchanging its altitude for range. This flight phase is modelled as pure unpowered glide, depending solely on the altitude (h), and maximum glide ratio $(L/D)_{max}$. When the aircraft's glide angle is moderate the maximum range for unpowered glide in no-wind condition and for flat terrain is expressed by [4]:

$$R_{ug} = h \left(\frac{L}{D} \right)_{max} \tag{4.4}$$

4.2.5 Effects of Wind

Small unmanned aircraft are often operating in relatively high wind speeds - commonly exceeding half of the true air speed. Depending on the speed and direction, en-route winds may have a significant influence on the obtainable range of the aircraft. Therefore, in an effort to accurately estimate the maximum obtainable range of an aircraft, one has to include the wind effects. This study aims to describes a method for determining the maximum obtainable range, while including the effects of horizontal winds that are encountered en-route. Note that this wind model shall be applied to each segment of the flight.

In [61] it is described how the optimum airspeed may be determined when accounting for head- and tailwinds. The author states that for propeller-powered aircraft the optimum airspeed is obtained through:

$$m_{br} = \frac{v_{TAS}}{v_{br}} = \left[\frac{2\, m_{br} \pm \left(\frac{v_w}{v_{md}}\right)}{2\, m_{br} \pm 3 \left(\frac{v_w}{v_{md}}\right)} \right]^{\frac{1}{4}} \tag{4.5}$$

Here m_{br} is the relative airspeed parameter between the true airspeed and the best-range airspeed (v_{br}). v_w is the wind speed, with $\pm$ indicating a head- or tailwind, v_{md} is the minimum-drag airspeed. Solving for m_{br} yields the optimum ratio to achieve the best range in the event of head- or tailwind. As Eq. (4.5) only takes into account head- or tailwinds along the flight path, it is necessary to include and isolate the crosswind component that may be encountered en-route. When assuming a flat and non-rotating Earth and flying in level and unaccelerated flight, the equations of motion through decomposed wind vectors are modelled as:

$$v_{GS} = v_{TAS} \begin{bmatrix} cos\,\phi \\ sin\,\phi \end{bmatrix} + v_w \begin{bmatrix} cos\,\theta_w \\ sin\,\theta_w \end{bmatrix} \tag{4.6}$$

Here v_{GS} is the aircraft's ground velocity vector, and θ_w is the direction of the wind. The aircraft's commanded heading (ϕ) is the sum of the course angle (θ) and the crab angle (β). Here β is defined as the angle between the TAS vector and the ground course angle. The wind components perpendicular and parallel to the resulting ground track, in relation to the reference horizontal path, can be found by rotating the wind's x and y components through angle θ, resulting in [147]:

$$\begin{aligned} v_{\parallel} &= v_{wN}\,\cos\,\theta + v_{wE}\,\sin\theta \\ v_{\perp} &= -v_{wN}\,\sin\,\theta + v_{wE}\,\cos\theta \end{aligned} \tag{4.7}$$

Considering the horizontal wind field to be described in the NED (North, East, Down) frame, then v_{wE} is the decomposed East wind component, and v_{wN} is the decomposed North wind component. $v_{\parallel}$ is the wind component parallel to the aircraft's ground course and $v_{\perp}$ is the perpendicular wind component to the ground course. In relation to Eq. (4.5) the parallel wind component constitutes the value for v_w.

4.3 Path Planning

In this section, the optimization problem formulation and the cost function that has to be minimized by the Particle Swarm Optimization (PSO) are presented. The Apeendix contains a detailed description of the PSO algorithm.

4.3.1 Optimization Problem Formulation

In this study the goal is to find a safe path with the shortest length. Therefore, the cost function ought to take into consideration both the path's length and the safety. Here a safe path is defined as a path in which the aircraft, in the event of

a critical engine or generator failure, is within flight range of a pre-specified safe landing spot.

A two-dimensions geographical approach is used in this work, where the optimization variables represent a set of waypoints of the path, with x (North) and y (East) positions in the NED frame. As the input positions of the origin, destination and landings spots are given in latitude and longitude coordinates, a conversion to the NED frame is needed. Besides, to use the result as an input for an Autopilot system it may be required to convert the waypoints to positions expressed in latitude and longitude.

The domain has to be defined taking into consideration that the UAV may not deviate too far from the straight line path between the departure and destination.

To initialize the optimization algorithm, first a straight path from the origin to the destination is generated - with waypoints distributed equally along the path. This strategy is crucial, as usually the optimal solution will be a deviation from this straight path. If only particles initialized with random positions are used, they might have uncommon waypoints displacement, causing the algorithm to take longer time to find an optimal solution or to fall into a local minimum.

The stop criteria used is straight forward. The algorithm runs until it reaches a pre-defined number of iterations.

4.3.2 Cost Function

Always flying within range of a safe landing spot may not always be desired (or realistic), since this may cause the path to be too long. For that reason a cost function (f) is proposed that employs a method for weighing the importance of the safety against the importance of the path length. As shown in the following equation, α represents the weight of the path's length over the safety. This results in:

$$f = (\alpha)\, length + (1 - \alpha)\frac{1}{safety} \tag{4.8}$$

where *length* and *safety* are relative values and in this study presented as percentages. The function is calculated based on the minimum length, which is the straight line between the departure and destination, as per Eq. (4.9), and the maximum safety, if all points along the path are safe, as per Eq. (4.10).

$$length = \frac{\text{current length } (L_{cur})}{\text{minimum length } (L_{min})} \tag{4.9}$$

$$safety = \frac{\text{number of safe points } (n_{safe})}{\text{total number of points } (N_{path})} \tag{4.10}$$

To ensure that the safety is evaluated for the entire path, and not only for the position of the waypoint, an interpolation is performed to discretize the path into N_{path} number of points. The effective flight range using battery power is calculated to all landing spots that are not further than the maximum range which the UAV could fly by taking into consideration a vector of wind that would provide the maximum range, thus, landing spots very far away are not considered in that step of the algorithm, saving computational power. As the wind might change along the path between the point and the landing spot, the range is recalculated every R_{step} considering the closest wind vector.

For each point (n), it is evaluated if it is close enough to at least one landing spot (j). Then one unity is added to the safety result variable, demonstrated by:

$$n_{safe} = \sum_{n=1}^{N_{path}} \begin{cases} 1 & \text{if } (r_1^n < d_1)||...||(r_j^n < d_j) \\ 0 & \text{otherwise} \end{cases} \tag{4.11}$$

The total length is the sum of the distance between the points of the interpolation:

$$L_{cur} = \sum_{n=1}^{N_{path}} \sqrt{(x_n - x_{n-1})^2 + (y_n - y_{n-1})^2} \tag{4.12}$$

4.4 Case study and Experimental setup

4.4.1 Case Study

The scenario chosen for this simulation comprises the area located to the north of the Norwegian city of Trondheim (Figure 4.1). For this study the Norwegian Defence Research Establishment (FFI) made regional wind models available for calculating wind speeds and directions for different altitudes with the resolution of 2.5 km. The date of the data retrieval was July 5th 2017, with wind information valid between 03:00PM and 09:00PM of that day. The orange polygon in the figure illustrates for which region the information was available. The locations of the origin (A) and destination (B) were chosen so that the maximum length across the wind model's specified area was utilized. The straight-line path distance between

origin and destination is 210 kilometers, illustrated by the red dotted line, and has a path safety of 72.6%. The safe landing spot locations were manually selected through studying satellite imagery. The initial cruise altitude is chosen to be 1500 meters, meaning it can pass any mountain the aircraft may encounter within the specified region.

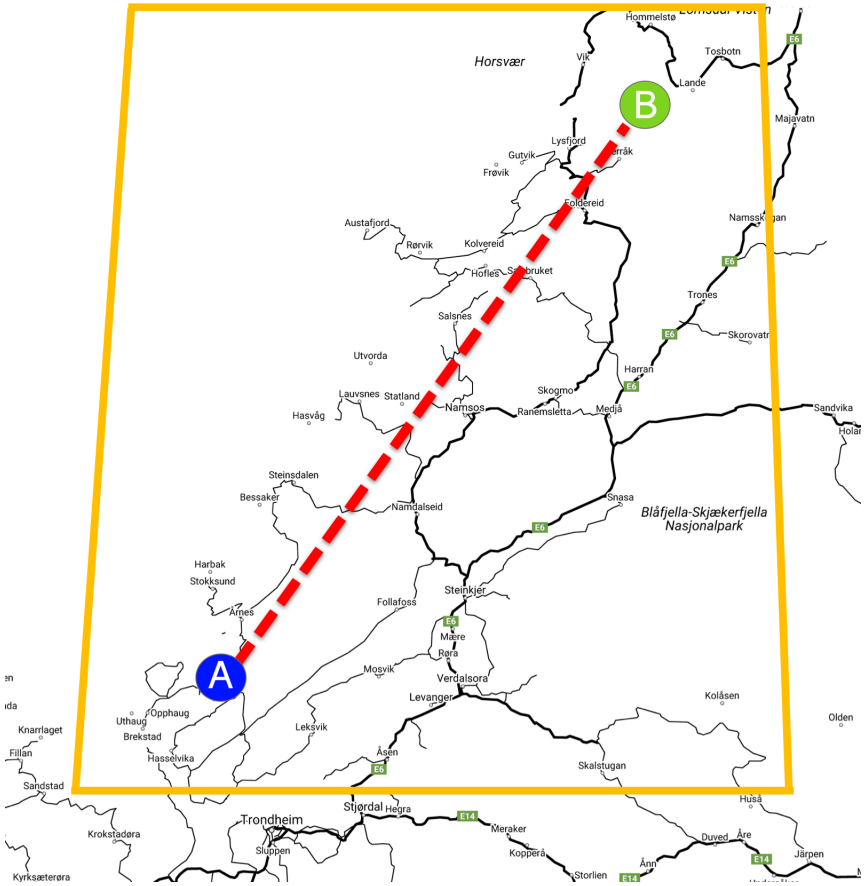

Figure 4.1: Simulation scenario

4.4.2 Experimental Setup

This case study utilizes the P31015 concept UAV, which is a fixed-wing aircraft in conventional pusher configuration. In this theoretical study the model shall employ a hybrid propulsion system with sufficient capacity to allow continuous in-flight recharging of the batteries - effectively enabling fully charged batteries during cruise flight. The total propulsion efficiency through the generator (η_{pg}) is assumed to be invariable at 28.5% while the specific fuel consumption c equals 383 grams per

horsepower per hour. The direct electric propulsion efficiency (η_{pe}) is assumed to be invariable at 50%. These values lie within range of experimental data found in [31], [98] and [75]. At the initiation of the cruise phase the aircraft is modelled to carry 5.5 liters of on board fuel, and to have a fully charged battery with a usable nominal capacity of 10 Ampere-hours at 44.4 Volts. The total weight of the aircraft is assumed to be 17.5 kilograms. More detailed aircraft specifications may be found in [72].

The theoretical maximum obtainable range of the aircraft at any point in time during the cruise phase is calculated as the sum of R_{no}, R_{bp} and R_{ug}. As R_{ug} is defined as the maximum obtainable range related to flat terrain, this requires to be re-evaluated when considering operating in mountainous terrain, such as the selected region for this experiment. The terrain in the selected region is mountainous, and contains elevated fields nearly as high as the selected cruise altitude. Therefore the actual obtainable glide range is considered too variant. Thus, in this specific simulation it is decided to leave out the potential range of unpowered glide, leaving the sum of R_{bp} as the maximum obtainable range in case of an engine failure.

4.4.3 MATLAB Code description

A MATLAB script was written to perform the simulation. The main user inputs are the WGS-84 coordinates of the origin, destination and safe landing spots. The wind information obtained was previously saved in a .dat file, which is used for the evaluation of the cost function. The airframe characteristics and battery efficiency, as detailed in previous sections, need to be configured. The optimization parameters are shown in the next subsection. The script is set up so that it runs the optimization algorithm until a pre-determined number of iterations is reached. Figure 4.2 shows a simplified block diagram of the script.

4.4.4 Parameters and Optimization Algorithm

Some parameters need to be defined in the optimization algorithm. Several of these parameters may strongly affect the convergence speed of the algorithm, and can prevent it from falling into local minima. Among these are the PSO velocity constraint, which was chosen to be attached to the domain in order to be automatically changed according to the problem; and the initial and final inertia weight, which were chosen to range from 1.0 to 0.1, to allow a more global search at the beginning, and a more local search in the course of iterations. However, other parameters can hardly be modified as they are specified by the user's requirements, which affects the processing time. For instance, this is the case with the number of points which discretize the path (N_{steps}). The parameters used in this simulation are presented in the table below, where the domain is defined by $[x_{min}, x_{max}, y_{min}, y_{max}]$:

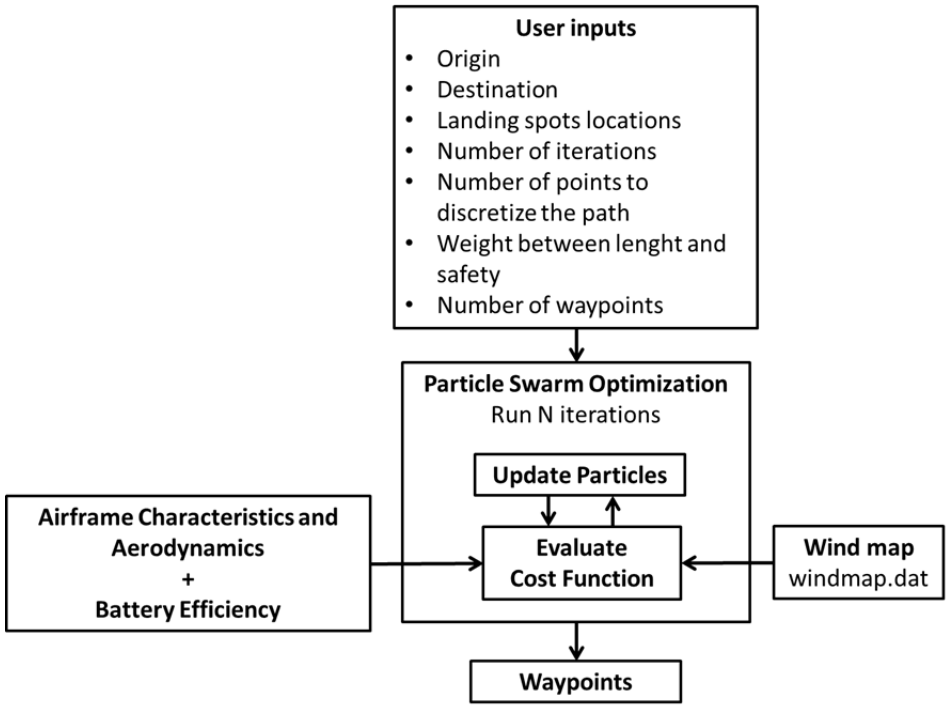

Figure 4.2: Overall block diagram

4.5 Results

Figure 4.3 shows the simulation result in the NED frame for a simulation using $\alpha = 0.3$. The yellow square and the green star represent the origin and destination respectively. The red circles are the generated waypoints, while the red crosses represent the safe landing spots. The path's discretized points are presented as black dots. The arrows represent the distance from the point of the path to a landing spot which the UAS can reach during a critical engine failure. This also takes into account the effects of wind. What may be observed is that the projected path is always close enough to at least one of three safe landing spots, resulting in two landing spots to not be utilized within this scenario. It was found that in this specific scenario the calculated path has a safety factor of 100%, with a total length of 215.4 kilometers. This route is 5.4 kilometers longer than the straight path distance between origin and destination. The convergence of the algorithm is shown in Figure 4.4, where the vertical axis refers to the Cost Function, Eq. (4.8).

In an attempt to study the effects of the positioning and amount of safe landing spots, a second simulation was conducted where the first landing spot was removed, as illustrated in Figure 4.5. Here it is impossible to reach a safety score of 100% due

Table 4.1: List of parameters

Name	Value
Number of iterations	100
Particle velocity constraint	0.1 x Domain
w_{ini}	1.0
w_{fin}	0.1
N_{steps}	84
Safe landing spots	5
x_{min}	x_s-$L_{min}/2$
x_{max}	x_t+$L_{min}/2$
y_{min}	y_s-$L_{min}/2$
y_{max}	y_t+$L_{min}/2$
R_{step}	5 km

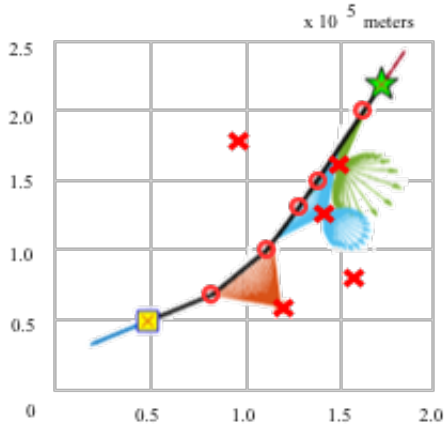

Figure 4.3: Result for $\alpha = 0.3$

to the distance between the landing spots. The grey dots forming a line indicates the part of the path where the UAS can not reach a landing spot in case of engine failure. In this specific case it was found that for $\alpha = 0.3$ the rated path safety was 83.3%, while the path distance had increased to 231.4 kilometers.

In a third scenario where five safe landing spots were placed at different locations, the simulation for $\alpha = 0.3$ resulted in a path with length 229.4 and safety of 100%. When $\alpha = 0.7$ was chosen, the length was shorter (219.9 km), while the safety was 90.48%.

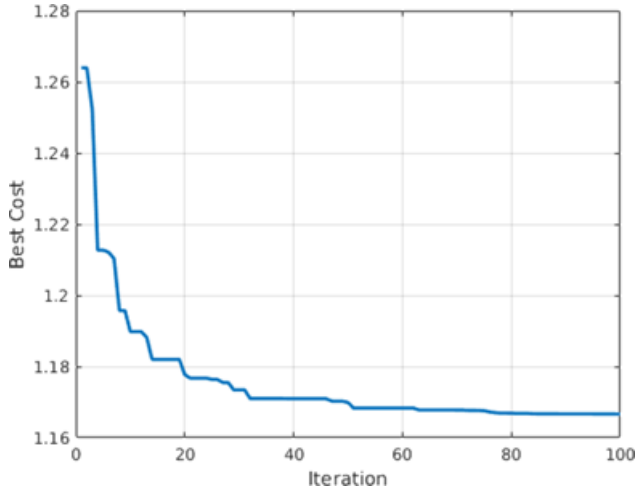

Figure 4.4: Algorithm convergence

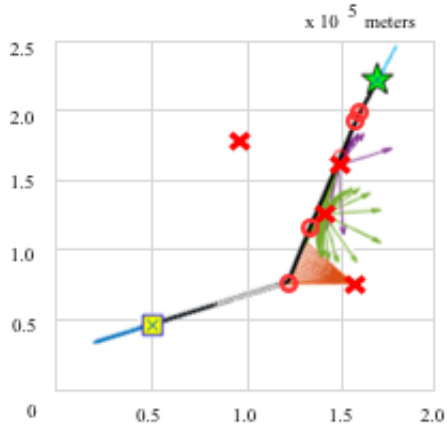

Figure 4.5: Result without LS1 for $\alpha = 0.3$

Therefore in this scenario it was found that compared to the straight-line trajectory, the trade-off for $\alpha = 0.3$ is 27.4% increased safety against an increase of 19.4 kilometers in path length. When using an α of 0.7, the trade-off was of 17.9% increased safety against 9.9 kilometers increase in path length, when compared to the straight-line trajectory.

Figure 4.6 illustrates a magnified part of the path, including the plotting of the wind vectors (orange arrows). The blue arrows represent by size the range that the UAS can obtain using the electrical battery from the discretized point of the path (black dots) to the landing spot (red cross). It may be observed that the wind is pointing south, resulting in a larger obtainable range when flying North to South,

compared to flying South to North.

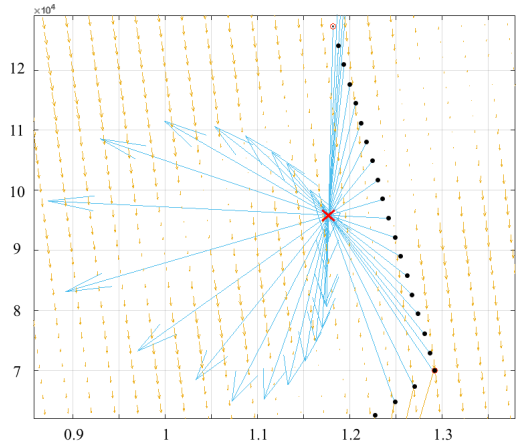

Figure 4.6: Extract of path including the wind vectors

4.6 Limitations

The suggested methods are evaluated through performing simulations. The physical input parameters, such as the wind, are predicted values based on weather model simulations. The suggested method does not include vertical winds, nor was this information available. The aerodynamic and propulsion efficiency parameters that were used are drawn from a concept aircraft and hybrid system, with assumed performance characteristics. Although the geographic model is realistic, the safe landing spots were chosen arbitrarily. All before mentioned limitations may influence the accuracy of the proposed model, and therefore a verification of the model may be warranted.

4.7 Discussion

To eliminate the limitations described in the previous section, and to further verify the proposed model, more simulations are needed. Besides the verification, a validation through flight test is to be conducted through utilizing an aircraft with known performance characteristics. One desirable improvement is to optimize the algorithm to reduce the processing time, so that in-flight real-time recalculation becomes a possibility.

Though it is beyond the scope of this study, one might consider using a more sophisticated glide performance model, such as described in [22] which also includes the effects of turn performance on the achievable range, and consider [41] and [142]

which describe an optimization method for the in-flight performance in variable (and altitude dependent) winds.

4.8 Conclusion

In this chapter a method was proposed that aims to increase the operational safety of hybrid-electric powered UAVs. This was done by taking into account the possibility of direct-electric propulsion in case of main generator failure. It was demonstrated that the aircraft's projected flight path can be adjusted so that it remains within range of pre-specified safe landing spots. This is done while taking into account the pre-calculated effects of winds that are encountered en-route by including an altitude-dependent wind model. As it is not always possible (or desirable) to have a completely safe path, the proposed method includes a cost function in which the user may specify the importance of path safety over the path length. A first simulation ($\alpha = 0.3$) with arbitrarily picked safe landing locations shows a path safety of 100%, while having a total path length of 215.4 kilometers. This is opposed to the straight path distance of 210.0 kilometers which offers a path safety of 72.6%. In this instance it is concluded that the trade-off may be an increased path safety of 27.4% at the cost of a longer path length of 5.4 kilometers. In a second simulation (also $\alpha = 0.3$) one central safe landing spot was removed. This simulation resulted in a path safety of 83.3%, while having a total path length of 231.4 kilometers. The trade-off may be determined through a similar approach. A third scenario was tested where the five safe landing spots were placed at a different location, while α was chosen to be 0.3 and 0.7. In this scenario it was shown that compared to the straight-line trajectory the trade-off made for $\alpha = 0.3$ is 27.4% increased safety against an increase of 19.4 kilometers in path length, while for $\alpha = 0.7$ this is 17.9% increased safety against 9.9 kilometers increase in path length. The study presented here was a theoretical study based on simulations utilizing hypothetical aircraft systems. To further validate and verify the proposed methods, a future study with more diverse simulated scenarios is suggested, and to perform test flights conducted with an aircraft that has known performance characteristics.

Part III

In-flight Performance and Airframe Design Considerations

Chapter 5

Mission Performance Trade-offs of Battery-powered sUAS

In this chapter a sensitivity analysis is presented on the influence of the weight, altitude and speed of battery-powered sUAS on the resulting stall speed, endurance and range. To aid in the determination of the aircraft performance prior to flight, a method is being brought forth that quantifies the impact of these mission parameters. As a case study the P31015 sUAS is used. The P31015 is a concept model of a battery-powered sUAS with a total battery capacity of 977Wh. Since the aerodynamic model of the aircraft was determined through simulations, and the specific propulsion set-up is yet to be determined, the case study remains to be a theoretical approach. The proposed methods and limitations of this study are applicable to other electric sUAS in similar set-up.

5.1 Introduction

With the recent technological advancements in small Unmanned Aircraft Systems (sUAS) there has been an increase in the search for suitable applications. Where the commercial development of a manned aircraft is solely reserved to large specialized firms, this is not the case for the development of sUAS. The increasing growth of new sUAS platforms testify to this accessibility to the market. The lower costs and reduced regulatory complexity allow for smaller firms to enter the market and offer tailored solutions to the end-user's specific requirements. With the trend of tailored designs, there is room for a stronger role of the end-user in the design process. In these often multi-disciplinary settings there may be challenges in terms of expectations versus technical possibilities [55]. It is the author's observation that there is often a knowledge gap on the consequences of altering the mission requirements and the resulting consequences on the in-flight performance. This study aims to

contribute to the scientific community by offering a clear overview of the trade-offs of the in-flight cruise performance characteristics of a sUAS, and perform a sensitivity analysis on mission-specific flight characteristics. This paper shall demonstrate its proposed theory through analysis of the P31015 sUAS (Fig. 5.1) as case study. However, the proposed theoretical model (and limitations) are applicable to any electric sUAS in similar configuration. The theoretical framework of this article builds upon the work of Traub [136] and Donateo et al. [31] who studied the effects of the Peukert-constant and battery discharge rate on the in-flight performance of sUAS. Currently the P31015 is a conceptual aircraft, with an aerodynamic model that was approximated through simulations using the AVL software package [33]. The P31015 is an electric-powered sUAS in a conventional pusher configuration. The sUAS was specifically designed to offer strong wind penetrating capabilities and low landing speeds. Propulsion for the intended aircraft shall be delivered by one brushless motor with a maximum shaft power (P_s) of 6kW, while the electric power shall be delivered by two six-cell LiPo battery packs with a total capacity of 977Wh.

Figure 5.1: Maritime Robotics P31015 Prototype sUAS

5.2 Flight Envelope

In a level and unaccelerated flight at a given altitude, the net force on the aircraft's body equals zero. This requires that the aircraft produces a lift force (L) that equals the aircraft's weight (W), and thrust force (T) that equals the experienced aerodynamic drag force (D). For an electric sUAS the weight is considered constant during the length of the mission. For sUAS flying in subsonic, level and unaccelerated conditions the lift and drag forces are a function of the dynamic pressure (q_∞), wing surface (S) and the specific aircraft's known lift and drag coefficients (C_L, C_D) [4]. This results in:

$$L = W = q_\infty S C_L \tag{5.1}$$

$$D = T = q_\infty S C_D \tag{5.2}$$

Where:

$$q_\infty = \frac{1}{2}\rho_\infty v_\infty^2 \tag{5.3}$$

In level and unaccelerated flight the air density (ρ_∞) is incrementally constant. Demonstrated by Eq. 5.3 the dynamic pressure is therefore solely a function of the free-stream air velocity (v_∞). As described by [39], rearranging Eq. 5.1 results in the following expression for v_∞:

$$v_\infty = \sqrt{\frac{2}{\rho_\infty}\left(\frac{W}{S}\right)\frac{1}{C_L}} \tag{5.4}$$

5.2.1 Available power

Eq. 5.2 expresses that for level and unaccelerated flight the thrust force must equal the drag force that is experienced by the aircraft. As the efficiency of the propeller depends on airspeed, the resulting thrust force is a velocity-dependent variable. The measurement for the propulsion is therefore referred to in power (P) rather than force [25][3][52]. Multiplying the thrust force with airspeed results in the following expression for the available power (P_a):

$$P_a = \eta_p \, T \, v_\infty = \eta_p P_s \tag{5.5}$$

Today sUAS primarily utilize a fixed-pitch propeller. For the remainder of this study the assumption is made that for each situation an optimal propeller is installed to offer an invariant efficiency. Due to a lack of data the total efficiency of the complete propulsion system (η_p) is assumed to have a constant value of $\eta_p = 0.50$. This value lies within the range of the typical propulsion efficiency of a small sUAS, as described in [141].

5.2.2 Required power

To be able to compare the required power with the available power, one must also transform the required thrust into the required power (P_r). This is done by multiplying the required thrust with the velocity component, as expressed in Eq. 5.6. The required power for level and unaccelerated flight is determined by substituting Eq. 5.4 into Eq. 5.1 and 5.2. As proposed by [143] this results in the following expression for P_r:

$$P_r = D\, v_\infty = \sqrt{\frac{2\, W^3}{\rho_\infty\, S} \frac{C_D^2}{C_L^3}} \tag{5.6}$$

For level and unaccelerated flight a lift force is required that equals the aircraft's weight. Eq. 5.6 shows that for one specific aircraft design the drag, and consequently the required power, are solely a function of airspeed, as C_L,C_D are speed dependent variables, and the weight, air density and wing surface are constant parameters. When plotting P_r against v_∞, one illustrates what is known as the aircraft's power curve. This curve describes the required power at different airspeeds. With a total aircraft mass of 17.5 kilograms, or weight W of 171.7 Newtons, a wing surface of 0.81m^2 and flying at an altitude of 0m under International Standard Atmospheric (ISA) conditions (ρ_∞ = 1.225kg/m^3), the resulting power curve of the P31015 is shown in Figure 5.2.

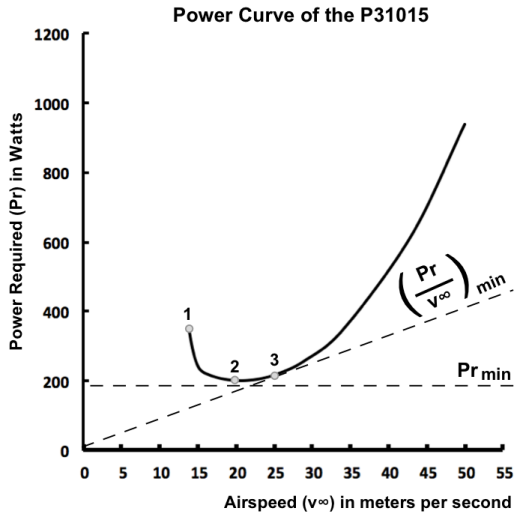

Figure 5.2: Power Curve of the P31015 - where $\rho_\infty = 1.225 kg/m^3$

5.2.3 Minimum airspeed

As the aircraft slows down, it can only maintain altitude by exchanging the lower airspeed for a higher C_L. However, the C_L of one aircraft is limited to a maximum, $C_{L_{max}}$, after which the aircraft will enter a stall. For most aircraft the practical minimum airspeed is naturally limited to be at the stall speed (v_{stall}) [52]. As described by [39] the expression for v_{stall} in level and unaccelerated flight can be obtained by rearranging Eq. 5.1 and Eq. 5.3 into:

$$v_{stall} = \sqrt{\frac{2}{\rho_\infty}\left(\frac{W}{S}\right)\frac{1}{C_{L_{max}}}} \tag{5.7}$$

Under the conditions described in the previous section the P31015 has a resulting stall steed of 13.8 meters per second. In Fig. 5.2 the stall speed and corresponding P_r are indicated as point (1).

5.2.4 Maximum endurance

Point (2) in Fig. 5.2 corresponds to the minimum amount of power required ($P_{r_{min}}$) for sustained horizontal flight. When flying at this speed, the electric power consumption per time unit is minimal. Thus the aircraft can stay airborne the longest on one battery load. This point is defined as the aircraft's maximum endurance [3]. This airspeed is relevant for planning long endurance missions. An example of such a mission could be the surveillance of a static object.

Relating to Eq. 5.6 the required power for flying at the speed that offers the maximum endurance is influenced by the aircraft weight, air density, surface, and lift and drag characteristics. During cruise flight the air density and wing surface are considered constant. In addition battery-powered aircraft have a constant total weight during flight [7]. Therefore the remaining variables are the aircraft's lift and drag characteristics. By flying at the aircraft's minimum ratio between C_D^2 and C_L^3, commonly known as $(C_L^3/C_D^2)_{max}$, the aircraft shall fly at the airspeed where the maximum endurance is achieved [116]. The corresponding airspeed can be found by substituting the value of C_L into Eq. 5.4. Under the standard conditions, as described in the section for the required power, the P31015 has a maximum endurance of 2.57hr (2hr 34m), at a speed of 20.0 meters per second.

5.2.5 Maximum range

Point (3) in Fig. 5.2 corresponds to the speed and power consumption for achieving maximum range (R_{max}). In contrast to maximum endurance, which aims to minimize the power consumption, the maximum range aims to maximise the trade-off between power consumption and ground distance covered [3]. This airspeed is relevant for missions that require the sUAS to fly as far as possible on one battery load, such as an A-B mission or an A-B-A mission. As described by [143] the speed for maximum range occurs at $(P_r/v_\infty)_{min}$ and can be found by substitution of Eq. 5.2 and 5.4 into 5.6, resulting in:

$$\left(\frac{P_r}{v_\infty}\right)_{min} = W\left(\frac{C_D}{C_L}\right)_{min} \tag{5.8}$$

Since the aircraft's weight is considered constant, this resulting expression shows that the maximum range is achieved by flying at the minimum ratio between C_D and C_L, commonly known as $(C_L/C_D)_{max}$. The corresponding airspeed can be found by substituting the value for C_L into Eq. 5.4. Under the standard conditions, as described in the section for the required power, the P31015 has a maximum range of 214km, at a speed of 25.6 meters per second.

5.3 Effective battery capacity

A typical (but inaccurate) way to determine the flight time of a battery-powered aircraft is by dividing the specified battery capacity by the current draw. Often it is assumed that a battery with a capacity (C) of 2Ah, while being discharged at a rate of 2A, is expected give a flight time of one hour. Similarly the flight time is often incorrectly assumed to be reduced to half an hour when the battery is discharged at 4A. In contrast to this method, a higher current draw reduces the battery's available capacity [136][31][29]. This behaviour can be assigned to the so-called Peukert-effect. In [136] it is proposed that when accounting for the Peukert-effect the discharge time (t) is described by:

$$t = \frac{R_t}{i^n} \left(\frac{C}{R_t} \right)^n \tag{5.9}$$

Where R_t is the battery hour rating in hours, and i the battery discharge current in Amperes. Here n is the Peukert-constant, which is a discharge parameter that depends on the battery type, and battery-specific factors, such as temperature, age and cycles runned [67]. Proposed by [136] the total battery output power (P_B) is then expressed by:

$$P_B = V \frac{C}{R_t} \left(\frac{R_t}{t} \right)^n \tag{5.10}$$

Where V is the battery voltage. By considering the total battery capacity to be invariant, and instead modelling the effective power consumption to be increased, the range and endurance can be determined by solving Eq. 5.10 for different airspeeds [136][31]. Consequently, the aircraft's maximum endurance (E_{max}, in hours) and maximum range (R_{max}, in kilometers) can be determined through:

$$E_{max} = \left(\frac{V \times C\,\eta_p}{\sqrt{\frac{2W^3}{\rho_\infty S}\left(\frac{C_D^2}{C_L^3}\right)_{min}}} \right)^n R_t^{1-n} \tag{5.11}$$

$$R_{max} = \left(\frac{V \times C\,\eta_p}{W\left(\frac{C_D}{C_L}\right)_{min}} \right)^n \left(\sqrt{\frac{2W}{\rho_\infty S\,C_L}} \right)^{1-n} \cdot {R_t}^{1-n} \cdot 3.6 \tag{5.12}$$

The P31015 shall be equipped with a LiPo battery pack with a capacity of 977Ah, of which the specific model is yet to be determined. Due to a lack of data the Peukert-constant n of the battery is therefore assumed to have a value of 1.05, corresponding to the typical value for a lithium-polymer battery pack found in [31]. This observation corresponds to a 2012 study by Omar [105] where it was found that the Peukert-constant for Lithium-ion based batteries typically vary between 1 and 1.09. The value R_t is the discharge time over which the capacity was determined. It is assumed that the capacity of the battery used in this study was determined over one hour, thus giving a constant value of R_t of 1.0. Similarly, for this study the battery voltage during discharge is assumed to be invariable, as these effects on the mission performance are usually limited, as found in [136].

5.4 Mission Parameters

This paper investigates the mission performance characteristics (stall speed, endurance and range) during the cruise phase of a mission. The typical parameters that a user often changes prior to a mission are the cargo capacity, flight altitude and airspeed. This paper aims to give a better insight in the impact of the change in these parameters on the mission performance of the aircraft through a sensitivity analysis. There are several interdependent relationships between these performance characteristics. The effects on the mission performance shall determined by analysing the shift of the power curve as the mission parameters change. These effects shall be discussed individually in the following sections.

5.4.1 Effects of changing Weight

Although a battery-powered sUAS typically has a fixed airframe weight, the choice of cargo can cause a change in total aircraft weight. To determine how the P_r versus v_∞ curve shifts, it is assumed that with changing total weight the altitude and aircraft configuration remain constant. Deriving from Eq. 5.4 and 5.6 the expression for the power curve can be reduced to:

$$P_r = constant_1 \sqrt{W^3} \tag{5.13}$$

$$v_\infty = constant_2 \sqrt{W} \tag{5.14}$$

As described by [143], with increasing weight the required power increases with $\sqrt{W^3}$, while the airspeed increases with $\sqrt{W}$. However, when also including the Peukert effect, as determined through by Eq. 5.10, the power curve shifts as illustrated in Fig 5.3. This figure shows the power curve at a total weight increase of 50%. Also this figure illustrates the aircraft's performance sensitivity to changes in weight on v_{stall}, E_{max} and R_{max}. In addition Table 5.1 lists the sensitivity to weight by showing the corresponding performance parameters to a fraction of the original total aircraft mass of 17.5kg (W_f in %).

Table 5.1: Resulting performance at varying weight (W_f as fraction of 17.5kg)

W_f	v_{stall} (ms^{-1})	E_{max} (hr)	R_{max} (km)
80%	12.3	3.7	272.0
100%	13.8	2.57	214.0
120%	15.1	1.9	175.9
140%	16.3	1.51	149.1

Through Eq. 5.11 and 5.12 an expression can be given for the sensitivity of the flight performance to the weight by:

- The stall speed is influenced by a factor of $\sqrt{W}$. Note that the aircraft's stall speed is not influenced by the Peukert effect. Thus the new stall speed can no longer be read directly from this resulting power curve.
- The maximum endurance is influenced by a factor of $W^{\frac{-3n}{2}}$
- The maximum range is influenced by a factor of $W^{\frac{1-3n}{2}}$.

An important remark is that the increase in weight is considered to be due to increased cargo weight. Alternatively the weight increase can be caused by an additional battery. In [136] and [137] a study was performed on the effects of the battery weight fraction on the in-flight performance in. However this study shall continue to focus solely on the influence of increased cargo load.

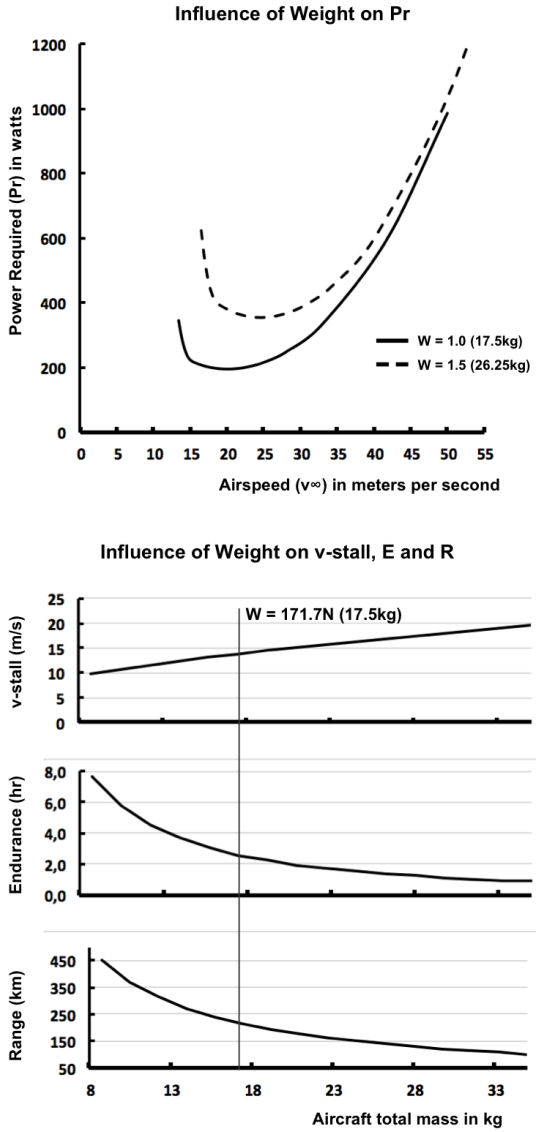

Figure 5.3: Influence of Weight on P_r, v_{stall}, E and R (n=1.05, $\rho = 1.225$)

5.4.2 Effects of changing Altitude

The influence of altitude on the performance parameters are evaluated similarly to that of the weight. To determine the shift of the power curve with increased altitude, it is assumed that the aircraft weight and configuration remain constant. As described by [143] Eq. 5.4 and 5.6 can be reduced to:

$$P_r = constant_3 \sqrt{\frac{1}{\rho}} \tag{5.15}$$

$$v_\infty = constant_4 \sqrt{\frac{1}{\rho}} \tag{5.16}$$

Eq. 5.15 and 5.16 demonstrate that with increasing altitude both the required power and the airspeed shall increase by $\sqrt{\frac{1}{\rho}}$. Similarly to the weight analysis, when also including the Peukert effect, the power curve shifts as illustrated in Fig 5.4. This illustration shows the shift of the power curve to an altitude of 3.0km, corresponding to $\rho_\infty = 0.909$ under ISA conditions.

In aircraft designs where the effects of ρ_∞ on C_L and C_D are small, or where the change of altitude is relatively small, the effects of altitude on the flight performance can be approximated through:

- The stall speed is influenced approximately by a factor of $\sqrt{\frac{1}{\rho}}$, as previously described by [143]. Note that similarly to an increase in weight, the aircraft's stall speed is not influenced by the Peukert effect.
- The maximum endurance is influenced approximately by a factor of $\rho^{\frac{n}{2}}$
- The maximum range is influenced approximately by a factor of $\rho^{\frac{n-1}{2}}$, as previously described by [136]

Fig. 5.4 shows the approximated values for the aircraft's mission performance as a result to change in pressure altitude. In addition Table 5.2 lists this sensitivity by listing the approximated performance parameters corresponding to a change in air density (ρ_∞) from zero to three kilometers. For the determination of the air density the ISA model was applied consistently.

Table 5.2: Resulting performance at varying altitudes (ISA)

h in km	v_{stall} (ms^{-1})	E_{max} (hr)	R_{max} (km)
$0km$	13.8	2.6	214.0
$1km$	14.5	2.4	213.5
$2km$	15.2	2.3	213.0
$3km$	16.0	2.20	212.4

Note also that, as mentioned before, the theoretical model presented in this paper assumes an invariant propulsion efficiency. As described in [67] the temperature of the battery influences its available capacity. As the temperature may drop with

increasing altitude this could ultimately influence the range and endurance of the aircraft as the battery cools down.

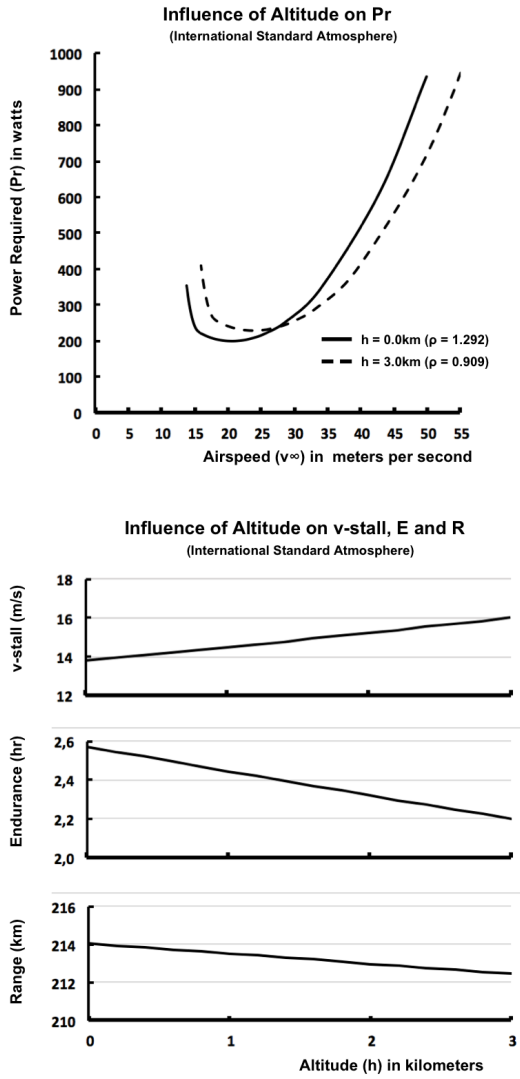

Figure 5.4: Influence of Altitude on P_r, v_{stall}, E and R (n=1.05)

5.4.3 Effects of changing Airspeed

By deviating from the speed $v_{E_{max}}$ or $v_{R_{max}}$, the aircraft will no longer follow the optimal cruise speeds for respectively maximum endurance and maximum range. The aircraft's range becomes solely a function of the achievable endurance, multiplied by the corresponding airspeed. The aircraft's stall speed remains unchanged.

For level and horizontal flight the required value of C_L changes in relation to a change in speed. Through the aerodynamic model of the aircraft the required airspeed for sustained level flight can be determined through Eq. 5.4. Then, through Eq. 5.11 the endurance can be determined for varying airspeeds. Note that this expression shall now produce the value for E instead of E_{max}. This is because the expression no longer utilizes the maximum C_L^3/C_D^2 ratio of the aerodynamic model, but simply the C_L^3 and C_D^2 values that correspond to that specific airspeed.

Fig. 5.5 shows the aircraft's mission performance sensitivity to changes in airspeed expressed in E and R. Table 5.3 shows the new performance parameters corresponding to a change in airspeed ranging van 20m/s to 40m/s kilometers.

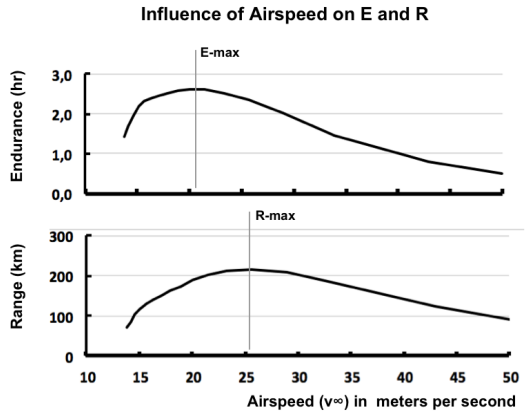

Figure 5.5: Influence of Airspeed on E and R (n=1.05)

Table 5.3: Resulting performance at varying airspeeds (interpolated values)

v_∞ in ms^{-1}	Endurance (hr)	Range (km)
20	2.5	187.5
30	1.89	202.7
40	1.02	141.59

5.5 Limitations and future work

As this paper presents an analytical case study, the validity of the proposed method is yet to be demonstrated through experimental test flights. Since the study was conducted on a conceptual design, it was performed with the assumption of an invariable propulsion efficiency, thus neglecting variances in battery temperature, voltage discharge effects and propeller efficiency. Anyone considering using these

presented methods with the purpose of determining the performance of an sUAS, ought to know the aircraft's complete aerodynamic model and propulsion efficiency parameters in order to obtain the correct results.

5.6 Conclusion

A method has been proposed which quantifies the influence of weight and airspeed on the mission performance of a battery-powered fixed-wing sUAS. In addition a method has been proposed that, with limitations, approximates the influence of a change in altitude on the mission performance parameters of the aircraft.

Part IV

Concluding Remarks & Recommendation for Future Work

Conclusion

In this thesis several methods are discussed to increase in the flight performance of fixed-wing small unmanned aircraft through intelligent path planning. By including relevant factors that affect the en-route performance, such as winds and icing conditions, it has been demonstrated through simulations that substantial improvements can be achieved. These findings have been documented in four parts.

The first part of the thesis demonstrated that by including information on forecast horizontal wind maps into path planning algorithms, substantial energy savings can be achieved in typical A-to-B missions. The goal of the algorithm was to find an optimum path that requires the least energy, taking into consideration the atmospheric parameters. In one instance it was found through simulations using PSO methods that considering the horizontal wind profile for fixed-altitude operations, a reduction in required propulsion energy of 4.2% could be achieved. In another instance, considering multi-altitude and potential icing conditions, it was found that an aircraft equipped with icing protection system, could obtain a reduction of up to 52%, when adverse icing conditions were present en-route. An interesting observation related to the icing protection system is also that en-route deicing could have a lower energy consumption compared to anti-icing.

In the second part of the thesis, the potential of advanced path planning in relation to operational safety were explored. In this work it was demonstrated that a hybrid-electrically powered small unmanned aircraft can take advantage of the dual-propulsive nature of the system, by considering this a redundant propulsion setup. In case of a critical engine failure the electric motor has the ability to safely bring the aircraft to a pre-defined safe landing spot. In order to have the aircraft always (or as much as possible) be in range of such a landing spot, advanced path planning methods were demonstrated. These include the aircraft performance model of hybrid-electric propeller aircraft, as well as en-route winds. In cases explored through simulations using PSO methods it was found that the en-route time spent in range of a safe landing spot was increased from 72.6% to 100% when a path was chosen that was 2.6% longer. Other scenarios were described which in every case quantifies the advantages of such optimization methods.

In the fourth and final chapter of the thesis airframe design consideration for increased in-flight performance were introduced. First a sensitivity analysis was presented of typical mission planning parameters (aircraft weight, cruising altitude and airspeed) on the resulting mission range, endurance and stall speed. The battery discharge effects are included in the analysis. This work provides operators of small unmanned aircraft with a better understanding and opportunity for optimizing the airframe for an increased operational envelope.

Additionally, in the appendix of the thesis work is presented where real-time path planning optimization methods were described in relation to the aircraft turn performance. The advantages were demonstrated through different applications where the mission performance depend heavily on the aircraft's turn performance. Initially the advantages were demonstrated through simulations using MPC for the case of multi-UAS airborne communication relaying between a ground station and unmanned surface vessel. Here the goal was to maximizing the communication range, while guaranteeing a minimum communication signal quality. It was demonstrated that, assuming constant wind, through airborne relay methods the signal strength was above the specified minimum threshold for a significantly longer period compared to direct communication. This ultimately effectively extended the communication range and signal strength. Similarly, the turn performance in path planning optimization was demonstrated through simulations using MPC for the use case of real-time multi-UAS Search and Rescue missions. It was found that a 50% probability of success mark in the case of three cooperative airborne systems was on average achieved 2.25 times faster when compared to a single UAS. Finally, methods are described for the design and integration of camera gimbal systems. This also includes considerations relating to in-flight aircraft performance.

Recommendation for future work

- **Aircraft performance model**: The aircraft performance models presented in this work are based on existing aircraft: X8 by Skywalker and the PX-31 by Maritime Robotics AS. Non-exact digital models of these airframes have been used in order to approximate the aerodynamic characteristics using Computational Fluid Dynamics (CFD) simulations. Although CFD methods are becoming increasingly more accurate and accessible, for low Reynolds applications it is difficult to obtain an accurate drag model. Ideally the presented work is repeated with the inclusion of a more accurate aerodynamic models, verified through wind tunnel experiments.

- **Propulsion efficiency model**: Similarly to the aircraft performance model, the presented work would benefit from an improved propulsion efficiency model, which was mostly assumed to be constant. This assumption has imposed limitations to the accuracy of the research results, and disabled the potential benefits of path optimisation based on variable propulsion efficiency. Propulsion efficiency tests have been performed in May 2018 in the wind tunnel located at NTNU's Fluid Mechanics Laboratory. This was done for several propellers suitable for the PX-31 airframe, with propellers in the range

of 22x10. Due to time constraints these measurements were never processed and integrated into the presented research. However, the data is available by request to continue the work. The logged data include set motor RPM, measured motor RPM, motor input voltage and current, ESC input voltage and current, commanded duty cycle, force balance measurements, wind tunnel airspeed, ambient wind tunnel temperature, wind tunnel set RPM and wind tunnel ambient pressure.

- **Icing effects model**: The aerodynamic effects of wing icing is a complex case, and in this work has been approximated using CFD methods. This includes modelling of essential data on the power requirements for the icing protection system. Ideally the presented work is repeated with an improved model, based on data obtained in icing wind tunnel experiments. Colleague researchers are performing such experiments at the moment of writing, and may publish an updated model. Fellow researchers are encouraged to improve the proposed simulations by including such updated models.

- **Real-time wind measurements**: The presented work relies on forecast wind maps that are either loaded prior to the mission, or intermittently updated during the execution of the mission. Ideally, such forecast models are complemented with in-situ measurements obtained in-flight by the aircraft. This creates the opportunity for an increased wind model accuracy. Fellow researchers are encouraged to integrate such methods, also described in [53].

- **Simulations versus field testing**: No field test has been conducted due to time and budgetary constraints. This is arguably one of the biggest drawbacks of the presented research. Although the researchers have spared neither time nor effort to set up simulation environments to represent the real world as good as they could, unfortunately it is practically unavoidable that significant real world effects are overlooked or otherwise neglected. Ideally, the presented methods are verified through field testing, under varying conditions.

Appendices

Appendix A

Path Planning of Multi-UAS Communication Relay by Decentralized MPC

When using Autonomous Surface Vehicles (ASV) in marine operations, long distances and/or low power transmissions may severely limit the communication between the ASV and the ground station. One solution to overcome this obstacle is to use a group of small Unmanned Aerial Systems (UAS) to act as relay nodes, in order to provide a user-defined minimum communication capability. To achieve this, a decentralized cooperative multi-agent system using fixed-wing UAS with nonlinear model predictive control is proposed, which aims to guarantee a desired signal strength between the ASV and the ground station. The novelty of the presented research resides in the inclusion of the aircraft performance model and the effects of wind, together with the inclusion of the directivity of the antennas. Experimental results of the proposed method are obtained through simulations.

A.1 Introduction

Utilizing an Autonomous Surface Vehicle (ASV) in maritime missions brings forth the need for a reliable communication link with sufficient signal strength between the ASV and the ground station. Although in some cases a direct link can be used, it is often severely limited in range and affected by the local geography. Satellite communication can manage longer distances, but can not always be used due to partial satellite coverage, limited bandwidth or the high associated costs. An alternative solution is to use autonomous fixed wing Unmanned Aerial Systems (UAS) to act as communication relay nodes in order to establish a communication link between the ASV and the ground station. By strategically coordinating the

UAS' trajectories, the obtainable communication link can reach the desired signal strength over a larger distance.

In recent scientific literature, there are several approaches to solve similar problems. Grancharova et al. [50] used multiple rotary wing UAS to form a communication network between a base station, a stationary target and a moving target. The author used RF Signal Propagation, Loss, And Terrain (SPLAT!) for calculating the communication path losses. The path losses were approximated to linear functions, and a Model Predictive Control problem was solved by quadratic programming. Johansen et al. [79] describes the use of one fixed wing UAS as a communication relay node between a ground station and an Autonomous Underwater Vehicle (AUV), where the AUV was positioned at the ocean surface. In this reference, horizontally omni-directional antennas were used. However, in their experiment, due to the vertical directionality of the antenna beam, the roll angle of the UAS affects the communication signal power. Kim et al. [81] used multiple autonomous fixed wing UAS as communication relay nodes for a fleet of vessels using a decision making algorithm to choose the waypoints which could satisfy Dubins trajectories and lead to a configuration where the range between the nodes will be less than a specified minimum communication range. The solution was improved in [82], where the paths of the UAS were optimized using Nonlinear Model Predictive Control (NMPC), and the network connectivity was modelled in the context of Mobile Ad hoc NETworks (MANETs) based on global message connectivity. In this reference, the change on the directivity of the antenna pattern due to the effect of the attitude of the UAS was not considered. This made it simpler to model the communication characteristics, but also made it less realistic. In addition, the method does not consider the effects of wind or the power consumption of the UAS. Braga et al. [13] optimized the communication Quality of Service, considering the power consumption and the bandwidth. Here, a simplified power consumption estimation was used, and, again, the wind and the UAS attitude effect on the radiation pattern were not considered. In recent studies, Palma et al. [107] performed field experiments using a UAS as a data mule, i.e. the UAS was used to download and offload data sequentially, rather than to uphold a data link. Different protocols were tested where it is shown that the quality of the communication depends on the protocol being used. The author also states that the combination between the altitude and loiter radius, which determines the angle between the nodes, has a significant effect on the efficiency of data transfer due to the antenna-radiation patterns. Therefore, it is fundamental to define flight trajectories whilst taking this into consideration.

Dixon and Frew [27] used a decentralized algorithm based on the gradient of Signal-to-Noise Ratio (SNR) measurements to obtain a cascaded communication chain between a control station and a moving vehicle. A drawback of their method is

the limitation in the vehicle dynamics – a cyclic motion is required in order to obtain an estimate of the SNR – which can result in a non-optimal path. The authors do not consider power consumption of the vehicles, resulting in a functional communication relay, but with a reduced duration compared to an algorithm that considers the power consumption, and has more freedom in vehicle dynamics. Frew and Brown [43] considered a meshed network of UAV relay nodes. Experimental data showed that the meshed network improved the range and throughput of the communication link compared to a static meshed network.

This chapter proposes a solution by using a decentralized nonlinear MPC to optimize the state of multiple UAS to achieve the desired signal strength between the ground station and the ASV. This is done while minimizing the power consumption of the maneuvering aircraft in order to maximize the mission endurance. As the directivity of the antennas is also considered, roll angles of the UAS are taken into account when determining the signal strength. The proposed solution also takes into account the effects of wind on the aircraft performance.

A.2 Methodology

A.2.1 Path Planning

Assuming that the path planning problem starts with all the UAS organized on a network topology (Figure A.1) providing the required transmitter-receiver signal strength between the ASV and the ground station, the aim of the algorithm is to optimize the states of the UAS to sustain a signal strength which does not fall below a preset requirement. A Nonlinear Model Predictive Control (NMPC) [17] method is used to optimize the airspeed and bank angle of the UAS to achieve the desired signal strength while minimizing power consumption.

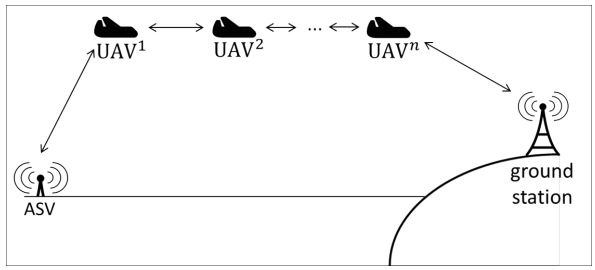

Figure A.1: Network topology

A centralized control system would need to optimize the control inputs of all the relay nodes, causing significantly increased complexity. With an increased number of relay nodes the method ultimately becomes unfeasible. Therefore, a fully decen-

tralized NMPC is proposed in this chapter, where each UAS plans its own path and attitude, taking into consideration the planned states of the other UAS and the planned position of the ASV in time. This can only be achieved under the assumption that the information can be shared between the UAS. Here, the UAS only needs to be able to communicate with the adjacent nodes.

Assuming that the UAS will fly at a constant altitude maintained by the autopilot, a two-dimensional kinematic model can be used based on the Coordinated Flight Vehicle model [117] as:

$$\begin{pmatrix} \dot{x} \\ \dot{y} \\ \dot{\psi} \\ \dot{v_a} \\ \dot{\phi} \end{pmatrix} = f(\mathbf{x}, \mathbf{u}) = \begin{pmatrix} v_a \cos\psi + v_w \cos\psi_w \\ v_a \sin\psi + v_w \sin\psi_w \\ \frac{g \tan\phi}{v_a} \\ u_v \\ u_\phi \end{pmatrix} \tag{A.1}$$

where $\mathbf{x} = (x, y, \psi, v_a, \phi)$ are the North and East positions in the NED frame, heading, air-relative velocity (airspeed) and bank angle of the UAS, respectively. v_w and ψ_w are the velocity and heading of the wind and g is the gravity acceleration of 9.81 $\mathrm{m/s^2}$. $\mathbf{u} = (u_v, u_\phi)$ are the acceleration control input and the roll rate control input, respectively.

The model is discretized by the forward Euler method:

$$\mathbf{x}_{k+1} = f_d(\mathbf{x}_k, \mathbf{u}_k) = \mathbf{x}_k + T_s f(\mathbf{x}_k, \mathbf{u}_k), \tag{A.2}$$

where T_s is the sampling period.

The overall control problem is decomposed as a unique local control problem for each UAS node, where each UAS optimizes its own state based on the signal strength with respect to its two adjacent nodes, while taking into consideration the planned states of the adjacent nodes. Collision avoidance and power consumption are also considered.

Considering n UAS ($\mathbf{x}^i, \forall i \in \{1, ..., n\}$), a fixed ground station ($\mathbf{x}^0$) and a moving ASV ($\mathbf{x}^{n+1}$), the NMPC algorithm finds a control input sequence $U_k^i = \{\mathbf{u}_0^i, \mathbf{u}_1^i, ..., \mathbf{u}_{N-1}^i\}$ $\in R^{2\times N}$ for the ith UAS, which solves the following optimal control problem:

$$\text{minimize} \quad \delta^i(\bar{\mathbf{x}}_N^i) + \sum_{k=0}^{N-1} L^i(\bar{\mathbf{x}}_k^i, \mathbf{u}_k^i) \tag{A.3}$$

$$\text{subject to} \quad \mathbf{x}_{k+1}^i = f_d(\mathbf{x}_k^i, \mathbf{u}_k^i) \tag{A.4}$$

$$v_{a\,min} \leq v_{ak}^i \leq v_{a_{max}} \tag{A.5}$$

$$\phi_{min} \leq \phi_k^i \leq \phi_{max} \tag{A.6}$$

$$\dot{v}_{a_{min}} \leq u_{vk}^i \leq \dot{v}_{a_{max}} \tag{A.7}$$

$$\dot{\phi}_{min} \leq u_{\phi k}^i \leq \dot{\phi}_{max} \tag{A.8}$$

$$\|\mathbf{C}_1(\mathbf{x}_k^i - \mathbf{x}_k^j)\| > r_c, \ \forall j \in \{1, ..., n\} \backslash \{i\} \tag{A.9}$$

where

$$\delta^i(\bar{\mathbf{x}}_N^i) = aJ^i(\bar{\mathbf{x}}_N^i), \tag{A.10}$$

$$L^i(\bar{\mathbf{x}}_k^i) = aJ^i(\bar{\mathbf{x}}_k^i) + b{u_{vk}^i}^2 + c{u_{\phi k}^i}^2, \tag{A.11}$$

and

$$J^i(\bar{\mathbf{x}}_k^i) = \alpha E^i(\mathbf{C}_2\bar{\mathbf{x}}_k^i) + (1-\alpha)P^i(\mathbf{C}_3\mathbf{x}_k^i). \tag{A.12}$$

$\bar{\mathbf{x}}_k^i = [\mathbf{x}_k^{i-1}, \mathbf{x}_k^i, \mathbf{x}_k^{i+1}]$ are the states of the adjacent nodes, N is the number of horizon steps and r_c is the minimum safe distance between the UAS to avoid collision. a, b, c are constant weighting factors and $\mathbf{C}_1$, $\mathbf{C}_2$ and $\mathbf{C}_3 \in R^{2\times 5}$ are used to define which state variables of the vehicles are to be considered in the equations. In case of $\mathbf{C}_1$, only the x and y positions should be used, in case of $\mathbf{C}_2$, x, y, ψ and ϕ are used and in case of $\mathbf{C}_3$, only v_a and ϕ are used.

$$\mathbf{C}_1 = \begin{bmatrix} 1 & 0 & 0 & 0 & 0 \\ 0 & 1 & 0 & 0 & 0 \end{bmatrix}, \tag{A.13}$$

$$\mathbf{C}_2 = \begin{bmatrix} 1 & 0 & 0 & 0 & 0 \\ 0 & 1 & 0 & 0 & 0 \\ 0 & 0 & 1 & 0 & 0 \\ 0 & 0 & 0 & 0 & 1 \end{bmatrix}, \tag{A.14}$$

$$\mathbf{C}_3 = \begin{bmatrix} 0 & 0 & 0 & 1 & 0 \\ 0 & 0 & 0 & 0 & 1 \end{bmatrix}. \tag{A.15}$$

As the main goal of the system is to provide the desired signal strength with the lowest power consumption, $E^i(\mathbf{C}_2\bar{\mathbf{x}}^i)$ through Eq. (A.16) is the difference between the desired and actual signal strength between the ith UAS and its adjacent nodes, while $P^i(\mathbf{C}_3\mathbf{x}^i)$ through Eq. (A.27) is the power consumption function. Finally, α is a weighting factor that defines how much power can be used to improve the communication.

A.2.2 Signal strength

The function of the transmitter-receiver signal strength between the ith UAS and its adjacent nodes is the sum of the difference between the calculated signal strength and the desired signal strength, for the ith UAS and each of the two adjacent nodes (Eq. A.16). If the signal strength is equal or higher than the desired one, the error is considered to be zero.

$$E^i(\mathbf{C}_2\bar{\mathbf{x}}^i) = \Delta Err^i(\mathbf{C}_2\bar{\mathbf{x}}^i)\frac{\frac{\pi}{2} - \arctan(-\beta\Delta Err^i(\mathbf{C}_2\bar{\mathbf{x}}^i))}{\pi}, \tag{A.16}$$

where β is the constant which defines how close the curve will be to a conditional function and $\Delta Err^i(\bar{\mathbf{x}}^i)$ is the difference between the desired signal strength and the minimum calculated signal strength as the following:

$$\Delta Err^i(\mathbf{C}_2\bar{\mathbf{x}}^i) = P_d - P^i_{min}(\mathbf{C}_2\bar{\mathbf{x}}^i), \tag{A.17}$$

where P_d is the desired signal strength and $P^i_{min}(\mathbf{C}_2\bar{\mathbf{x}}^i)$ is the lowest signal strength between the ith UAS and each one of its adjacent nodes, as the lowest signal strength is the one limiting the link. To calculate the minimum value between two elements, the following equation is used:

$$\begin{aligned} &P^i_{min}(\mathbf{C}_2\bar{\mathbf{x}}^i) = \\ &0.5(P^{i-1}_{dBm}(\mathbf{C}_2\mathbf{x}^{i-1}, \mathbf{C}_2\mathbf{x}^i) + P^i_{dBm}(\mathbf{C}_2\mathbf{x}^i, \mathbf{C}_2\mathbf{x}^{i+1}) - \\ &\sqrt{(P^{i-1}_{dBm}(\mathbf{C}_2\mathbf{x}^{i-1}, \mathbf{C}_2\mathbf{x}^i) - P^i_{dBm}(\mathbf{C}_2\mathbf{x}^i, \mathbf{C}_2\mathbf{x}^{i+1}))^2}) \end{aligned} \tag{A.18}$$

where $P^i_{dBm}(\mathbf{C}_2\mathbf{x}^i, \mathbf{C}_2\mathbf{x}^{i+1}) = 10\log P^i(\mathbf{C}_2\mathbf{x}^i, \mathbf{C}_2\mathbf{x}^{i+1}) + 30$.

To calculate the signal strength between nodes, the Friis equation [84] is used to calculate the received power, based on the distance between the nodes and the directivity of the antennas:

$$P^i(\mathbf{C}_2\mathbf{x}^i, \mathbf{C}_2\mathbf{x}^{i+1}) = P_t \cdot D^{i,i+1}(\mathbf{C}_2\mathbf{x}^i, \mathbf{C}_1\mathbf{x}^{i+1}) \cdot D^{i+1,i}(\mathbf{C}_2\mathbf{x}^{i+1}, \mathbf{C}_1\mathbf{x}^i) \cdot FSPL(\mathbf{C}_1\mathbf{x}^i, \mathbf{C}_1\mathbf{x}^{i+1}), \tag{A.19}$$

where $FSPL(\mathbf{C}_1\mathbf{x}^i, \mathbf{C}_1\mathbf{x}^{i+1})$ is the Free-Space-Path-Loss:

$$FSPL(\mathbf{C}_1\mathbf{x}^i, \mathbf{C}_1\mathbf{x}^{i+1}) = (\frac{\lambda}{4\pi d^i(\mathbf{C}_1\mathbf{x}^i, \mathbf{C}_1\mathbf{x}^{i+1})})^2, \tag{A.20}$$

and P_t is the transmitted power, λ is the wavelength, $D^{i,i+1}(\mathbf{x}^i, \mathbf{x}^{i+1})$ is the directivity gain with respect to the position and antenna angle of the ith and $(i+1)$th nodes, and $d^i(\mathbf{C}_1\mathbf{x}^i, \mathbf{C}_1\mathbf{x}^{i+1})$ is the distance between nodes:

$$d^i(\mathbf{C}_1\mathbf{x}^i, \mathbf{C}_1\mathbf{x}^{i+1}) = \sqrt{(x^i - x^{i+1})^2 + (y^i - y^{i+1})^2 + (z^i - z^{i+1})^2}, \tag{A.21}$$

where z^i is the constant z offsets of the antennas of the ith node.

The directivities are obtained by the following equation:

$$D^{i,i+1}(\mathbf{C}_2\mathbf{x}^i, \mathbf{C}_1\mathbf{x}^{i+1}) = 4\pi \frac{F(\theta(\mathbf{C}_2\mathbf{x}^i, \mathbf{C}_1\mathbf{x}^{i+1}))}{F_{avg}}, \tag{A.22}$$

where $F(\theta(\mathbf{C}_2\mathbf{x}^i, \mathbf{C}_1\mathbf{x}^{i+1}))$ is the power radiation pattern of the antenna and F_{avg} is the average power density over a sphere, given by:

$$F_{avg} = \int_0^{2\pi} \int_0^{\pi} F(\theta(\mathbf{C}_2\mathbf{x}^i, \mathbf{C}_1\mathbf{x}^{i+1}))sin\theta d\theta d\gamma, \tag{A.23}$$

where $\theta(\mathbf{C}_2\mathbf{x}^i, \mathbf{C}_1\mathbf{x}^{i+1})$ is the angle between the antenna of the ith node and the body of the $(i+1)$th node:

$$\theta(\mathbf{C}_2\mathbf{x}^i, \mathbf{C}_1\mathbf{x}^{i+1}) = \arcsin \frac{\mathbf{R}_z(\psi^i)\mathbf{R}_x(\phi^i)\mathbf{v}(\mathbf{C}_1\mathbf{x}^{i+1} - \mathbf{C}_1\mathbf{x}^i)}{d^i(\mathbf{C}_1\mathbf{x}^i, \mathbf{C}_1\mathbf{x}^{i+1})}, \tag{A.24}$$

where $\mathbf{v} = [0\ 0\ 1]$ is the reference vector from where the angle θ will be calculated relative to, $\mathbf{R}_x(\phi)$ and $\mathbf{R}_z(\psi)$ are the rotation matrices in x and y with respect to the angles ϕ and ψ [8].

$$\mathbf{R}_x(\phi) = \begin{bmatrix} 1 & 0 & 0 \\ 0 & cos\phi & -sin\phi \\ 0 & sin\phi & cos\phi \end{bmatrix}. \tag{A.25}$$

$$\mathbf{R}_z(\psi) = \begin{bmatrix} cos\psi & -sin\psi & 0 \\ sin\psi & cos\psi & 0 \\ 0 & 0 & 1 \end{bmatrix}. \tag{A.26}$$

A.2.3 Aircraft power consumption

To obtain an accurate model of the overall system performance, the in-flight performance of the aircraft needs to be considered [53][54]. In this study both the aircraft's airspeed and bank angle are being optimized. Therefore it is necessary for the aircraft performance model to evaluate the in-flight power consumption, and express the penalty for changing airspeed and performing longitudinal maneuvering. For a propeller-driven aircraft in steady flight the consumed power (P) is found through:

$$P = \frac{D\, v_a}{\eta_p}, \tag{A.27}$$

where D is the aerodynamic drag force experienced by the aircraft, v_a is the airspeed, and η_p is the total propulsion efficiency. For level flight the generated lift L equals the aircraft weight W. However, when the bank angle ϕ is no longer zero, the lift force is rotated by an angle ϕ in relation to the gravity component. This results in:

$$L \cos\phi = W. \tag{A.28}$$

In this study the loss of lift caused by an increased bank angle is mitigated by increasing the airspeed. This is done so that a constant altitude can be maintained. It is therefore necessary to account for the effects of bank angle ϕ on the required airspeed v_a. When considering a coordinated flight the adjusted airspeed for a turn with constant-C_L is found through:

$$v_a = \sqrt{\frac{2W}{\rho_\infty S}\frac{n}{C_L}} = v_\infty \sqrt{n}. \tag{A.29}$$

Here v_∞ is the required airspeed for level unaccelerated flight in [m/s]. S is the aircraft's effective wing surface in [m^2], W is the aircraft's total weight in [N], and ρ_∞ is the air density in [kg/m^3]. The initial aerodynamic lift coefficient C_L is determined through:

$$C_L = \frac{2W}{\rho_\infty S v_\infty^2}. \tag{A.30}$$

Furthermore, n is the load-factor, which in accelerated flight is larger than zero. This is defined as:

$$n = \frac{1}{\cos\phi} = \left(\frac{T}{W}\right)\left(\frac{L}{D}\right). \tag{A.31}$$

In level unaccelerated flight and constant speed level turns the condition applies that the generated thrust force T equals the drag force experienced by the aircraft. Assuming a general simplified drag model in a coordinated flight where trim drag is neglected, and the thrust line is parallel to the airspeed, the drag force D is obtained through [3]:

$$D = T = \frac{1}{2}\rho_\infty v_a^2 S \left[C_{D_0} + k\left(\frac{nW}{qS}\right)^2\right]. \tag{A.32}$$

Here C_{D_0} is the aircraft's zero-lift drag coefficient. Finally, k is the lift-induced drag constant, which is defined as:

$$k = \frac{1}{\pi\ AR\ e} \tag{A.33}$$

Here AR is the aircraft's effective aspect ratio, and e is the Oswald efficiency factor.

Figure A.2: Skywalker X8 sUAS - operated by AMOS UAVLab (Source: NTNU)

In this study the Skywalker X8 aircraft is used in the simulations. The X8 (Figure A.2) is a small battery-powered unmanned aircraft in flying-wing configuration. It has a wingspan of 2.1 meters with a mission-ready weight of 3.36 kilograms. The

effective wing surface is approximately 0.74 square meters. Two elevon control surfaces are located on the outer wings to provide longitudinal, lateral and directional control of the aircraft. The aerodynamic lift model that was used in the simulation was based on wind tunnel experiments, which are described in [51], while the value for k is assumed to be 0.0907. The propulsion characteristics are unknown. Therefore for the remainder of this study the propulsion efficiency η_p is assumed to be invariable at 0.5, and the maximum thrust T_{max} is assumed to be constant at 25 N with ideal-battery discharge characteristics.

From Eq. (A.31) and (A.32) it can be observed that as the bank angle increases, the power consumption increases. The in-flight performance, and consequently the power consumption, are affected through the required increase in airspeed. It is important to note that to avoid the aircraft from entering a stall, the maximum load factor n_{max} is limited by the available thrust. The thrust-limited maximum load factor can be found by substituting the maximum available thrust in Eq. (A.31). Solving for ϕ yields the thrust-limited maximum bank angle. The minimum value for the airspeed v_{stall} as a function of load factor n and $C_{L_{max}}$ can be found by inserting the maximum lift coefficient into Eq. A.29. This results in:

$$v_{stall} = \sqrt{\frac{2}{\rho_\infty} \frac{W}{S} \frac{n}{C_{L_{max}}}}. \tag{A.34}$$

Finally, a *structural* limitation exists. As the structural limit load factor for the Skywalker X8 platform is not known it is chosen to implement a stricter limitation for the simulations as further referenced in section A.4.

A.3 System description

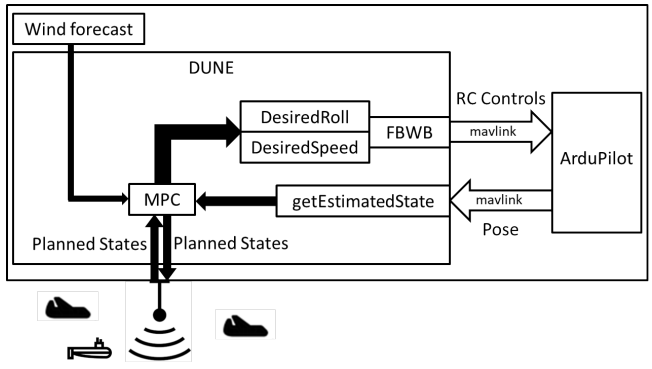

Figure A.3: Individual system's block diagram.

The simplified block diagram of the control system is shown in Figure A.3. The Model Predictive Control (MPC) runs inside DUNE [108], which is an open source robot framework developed by the Underwater Systems and Technology Laboratory (LSTS) of the University of Porto. DUNE is installed on the onboard computer and communicates with the ArduPilot board via Micro Air Vehicle Communication Protocol (MAVLink). When executing the maneuver, the ArduPilot opperates in Fly-By-Wire-B (FBWB) mode and gets the desired roll and airspeed as Radio Control (RC) inputs from DUNE.

The MPC is included in a DUNE task. Every time the UAS gets the updated planned states of the adjacent nodes, it calls the MPC function and, based on its current state and on the adjacent nodes states, it calculates its own planned states. In this step, the wind forecast present in a data file is also considered. After the optimization, the UAS broadcasts its planned states to the other nodes and sends the commands to the ArduPilot. The coordination of the mission is done by the dispatch and consumption of Inter-Module Communication Protocol (IMC) messages. In DUNE, if a IMC message is dispatched by a node, all nodes that are monitoring that type of message will receive it and run the routine binded to the reception of that message.

A.3.1 Mission coordination

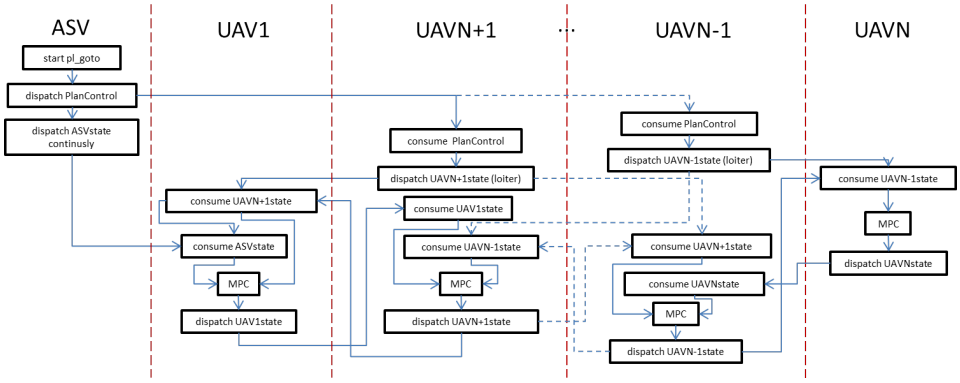

Figure A.4: Communication between nodes using IMC messages and DUNE Tasks

Each UAS awaits the start of the mission in loiter mode. When the ASV starts the plan, it dispatches a "PlanControl" message that is consumed by the UAS. All UAS then start the maneuver and dispatch their planned states considering the loiter maneuver, except the UAS closest to the ASV and the one closest to the Ground Station. These two UAS wait for the planned states of their adjacent nodes and are the first ones to run the MPC. Figure A.4 shows the flow chart of the IMC messages between the nodes.

A.4 Simulations

The first simulation (Figure A.5) was done for a scenario considering two UAS to close the wi-fi link between the ASV and a ground station. The simulation starts when the ASV is at position [300,300] - 423 meters away from the ground station. The first UAS starts the mission at position [100,100] and the second one at position [200,200]. The ASV is moving north with constant speed over ground of 1.6 m/s.

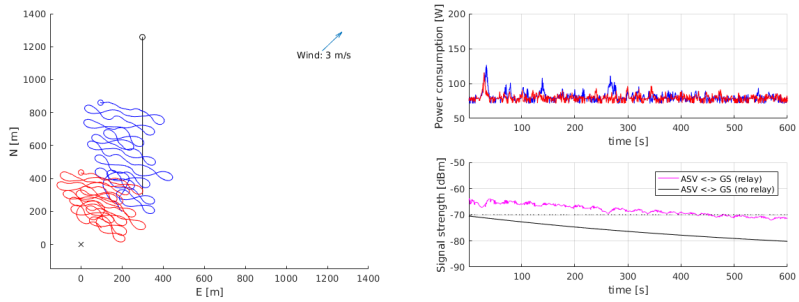

Figure A.5: First simulation scenario. Ground station as a black x, ASV's path in black, UAS 1's path in blue and UAS 2 path's in red.

It is possible to notice that when the mission starts, the straight link between the ASV and the ground station has less than -70 dBm, which was chosen as the desired signal strength as it is the minimum power to establish a wi-fi connection. Using the UAS, the ASV can progress with the mission for more 8 minutes (or 768 meters north), when two UAS are not capable to provide the desired signal strength anymore. This means an increase from around 400 to 800 meters of operational radius around the ground station, resulting in an operational area 4 times bigger. This increase can be expanded if more UAS are used as relay nodes.

Considering the different limitations of the load factor, the maximum bank angle ϕ_{max} is chosen to be restricted to 20^o, which offers an associated stall speed of 8.9 meters per second. Therefore the minimum airspeed $v_{a_{min}}$ is defined to be 12.0 meters per second. The other parameters used in the simulation are shown in tables A.1, A.2 and A.3.

To solve the NMPC problem, Particle Swarm Optimization (PSO) [34] was used. The algorithm, which is described in Appendix D, was developed using CUDA C programming language, benefiting from the parallelization to reduce the computational time. Each optimization takes around 250 ms, proving the algorithm suitable for real-time applications. The computational time can be reduced if necessary, by adjusting the horizon and number of steps. This would result in a decrease of the optimality, but may be beneficial in real environments, as the system will calculate

the control inputs for a state closer to the state that it was when the calculation began.

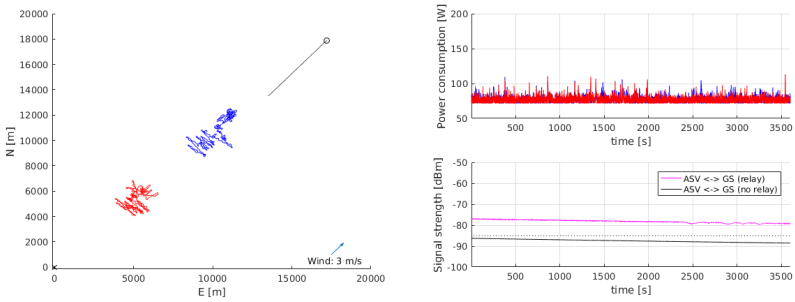

Figure A.6: Second simulation scenario. Ground station as a black x, ASV's path in black, UAS 1's path in blue and UAS 2 path's in red.

A second simulation was done for a scenario where the nodes were equipped with a communication system inspired by the characteristics of the Maritime Broadband Radio (MBR) 144 radio from the company Kongsberg Maritime [83], together with a 7 dBi antenna with around 25 degrees of $HPBW$ in the elevation plane. This radio can provide up to 20 km of range [157] for a frequency between 4.90 and 5.85 GHz. The communication parameters of this simulation were chosen as it is shown in table A.4 and the results are shown in Figure 6. The ASV starts the simulation at position [13500,13500] (around 19 km from the ground station) and the UAS 1 and UAS 2 at [4500,4500] and [8000,8000], respectively. Here, the duration of the mission was set to be one hour. It was found that besides the significant increase in obtainable communication range, it is also noticeable that the link between the ASV and the ground station when using the two UAS as relay nodes has a higher signal strength throughout the duration of the mission.

A.5 Discussion

In the current implementation of the algorithm, the wind is assumed to be constant. For small a aircraft, however, the wind can have a major effect on the power consumption. It would therefore be beneficial to use a forecast wind map or local wind estimations in the optimization algorithm. A proposed method for the forecast map is to fit an analytic function to a discrete wind map in order to improve the convergence of the optimization algorithm. Field experiments are also necessary in order to define constraints for the signal strength variations, that could affect the overall network capability.

Regarding the number of UAS and the ASV behavior, it is necessary to simulate

Table A.1: MPC Parameters

Param	Name	Value	Unit
v_w	velocity of wind	3.0	m/s
ψ_w	heading of wind	0.7	rad
g	gravity acceleration	9.81	m/s^2
t	time horizon	15.0	s
N	horizon steps	30	m/s
h	altitude of UAS	100.0	m
hN	altitude of the ground station	20	m
$v_{a_{min}}$	minimum airspeed	12.0	m/s
$v_{a_{max}}$	maximum airspeed	20.0	m/s
ϕ_{min}	minimum bank angle	-0.349	rad
ϕ_{max}	maximum bank angle	0.349	rad
$\dot{v}_{a_{min}}$	minimum acceleration	-0.2	m/s^2
$\dot{v}_{a_{max}}$	maximum acceleration	0.2	m/s^2
$\dot{\phi}_{min}$	minimum bank angle rate	-1.4	rad/s
$\dot{\phi}_{max}$	maximum bank angle rate	1.4	rad/s
r_c	safe distance between UAVs	50.0	m
a	weight of cost function	1.0	
b	weight of acceleration control	1.0	
c	weight of bank angle rate control	1.0	
α	weight of signal strength / power saving	0.99	

Table A.2: Communication Parameters of Scenario 1

Param	Name	Value	Unit
β	conditional function fitting constant	99999	
P_d	desired signal strength	-70	dBm
P_t	transmitter power	100.0	mW
λ	wavelength	12.5	cm
$HPBW$	Half-Power-Bandwidth	2.09	rad

scenarios where more UAS are used and that the ASV moves in different patterns to evaluate the system performance. Simulations using different altitudes for the UAS should also be considered.

A.6 Conclusion

In this chapter, a communication relay solution was presented. The goal of the system is to provide a minimum signal strength between the Autonomous Surface Vehicle and a ground station by using Unmanned Aerial Systems as communication relay nodes. The system was build to be used with DUNE robotic framework and was modeled as a Nonlinear Model Predictive Control problem. Simulations show

Table A.3: Power consumption Parameters

Param	Name	Value	Unit
η_p	propulsion efficiency	0.5	
W	aircraft weight	32.96	N
ρ_∞	air density	1.225	kg/m^3
C_{D_0}	zero-lift drag coefficient	0.125	
k	lift-induced drag constant	0.0224	
S	wing surface	0.74	m

Table A.4: Communication Parameters of Scenario 2

Param	Name	Value	Unit
β	conditional function fitting constant	99999	
P_d	desired signal strength	-85	dBm
P_t	transmitter power	2.0	W
λ	wavelength	6.0	cm
$HPBW$	Half-Power-Bandwidth	0.437	rad

that the system is capable to be tested in field experiments and may be a suitable tool in maritime missions.

Appendix B

Autonomous Unmanned Aerial Vehicles in Search and Rescue missions using real-time cooperative Model Predictive Control

Unmanned Aerial Vehicles (UAVs) have recently been used on a wide variety of applications due to their versatility, reduced cost, rapid deployment, among other advantages. Search and Rescue (SAR) is one of the most prominent areas for the employment of UAVs in place of a manned mission, specially because of its limitations on the costs, human resources, and mental and perception of the human operators. In this chapter, a real time path-planning solution using multiple cooperative UAVs for SAR missions is proposed. The technique of Particle Swarm Optimization is used to solve a Model Predictive Control problem that aims to perform search in a given area of interest, following the directive of international standards of SAR. The solution is able to be embedded in the UAVs on-board computer, using the Ardupilot autopilot and DUNE, an on-board navigation software. The performance is evaluated in a software-in-the-loop environment with the JSBSim flight dynamics model. Results show that when employing three UAVs, the group reaches 50% of Probability of Success 2.25 times faster than when a single UAV is employed.

B.1 Introduction

Over the last years, Unmanned Aerial Vehicles (UAVs) are becoming an important and indispensable tool in a wide variety of applications due to their versatility, low cost, rapid deployment, among other advantages.

Search and Rescue (SAR) is one of the fields where the employment of UAVs brings many advantages over manned missions, such as its reduced costs, lower use of human resources, and mental and perception limitations of human operators. [121] was one of the first works to perform experimental tests of a complete autonomous single UAV SAR solution. A probability density function (PDF) that expressed the likelihood of the target's location was one of the main inputs of the system. Video data from the UAV was transmitted to the ground station, that processed it in real time using computer vision techniques to detect the presence of the target and update the PDF. Paths were generated by the ground station to maximize the probability of finding the targeted object. The experimental flights showed satisfactory results in searching and detecting the target. The main necessary improvements identified by the authors were to implement on-board computing and to use multiple UAVs in the future.

Search and Rescue missions with autonomous UAVs are usually defined as an exploration problem. Exploration approaches can be used in a wide range of applications. For example, ice management, such as proposed by [62], where a Centralized Model Predictive Search Software was used for surveillance and tracking of ice using multiple UAVs. In this reference, the optimization finds a set of optimal waypoints that are sent to the autopilot. The solution was tested in a Software-In-The-Loop environment and the results were evaluated for a different number of UAVs. A broad literature review about the persistent surveillance problem was done by [103] focusing on the use of multiple UAVs. Persistent surveillance is a type of exploration problem where the areas must be revisited over time. Among the many topics that the literature review covers, grid decomposition and path-planning techniques are the ones of the most interest for this work. The author reviews the most common types of grid decomposition classifying the rectangular one, that is also used by the enhanced solution proposed by this chapter, as the most popular. Regarding the path-planning techniques, the author states that the most common methods are classical search methods such as A* [76], decision theoretic methods such as Mixed Integer Linear Programming (MILP) [40], and Spanning Tree Coverage (STC) methods [45]. Model Predictive Control (MPC) is mentioned as a topic less studied compared to the other planning techniques, but with significant advantages because it directly incorporate dynamic constrains, it is less heuristic and can react to changes in the environment.

Model Predictive Control [18] is a receding horizon control technique where the motion constraints are integrated to the control problem, which is particularly interesting for problems with fixed-wing UAVs. Also, as the optimization is done for a finite time horizon, the technique is proper for real-time problems where the environment can dynamically change during the mission execution. In [126], MPC

was used for sea Search and Track (SAT) missions using an autonomous UAV. Hardware-In-The-Loop tests were performed. Waypoints were optimized and sent to the autopilot. Gimbal attitude was also optimized and sent to the servo system. The MPC optimization was not run on-board but on a dedicated computer in the ground control station. In [24], a cooperative multiple UAV solution using MPC was used to close the communication link between a moving Autonomous Surface Vehicle and the ground station. Each UAV had to minimize a local cost function that took into consideration the planned states of the adjacent UAVs. In [26], a multiple UAVs receding horizon strategy was proposed for a cooperative surveillance problem. A potential field method was used for collision avoidance and network topology control management. The cooperative searching model was established based on the detection probability of the UAVs on targets in cells. In addition, a forgetting factor was included to indicate how fast the detection efforts are forgotten, so the UAVs can revisit the areas that were searched before. Simulations for different parameters were compared. Also, the performance of the proposed method was compared to the performance of a parallel sequence search. In [139], a multi-vehicle cooperative search solution was proposed using MPC. Decoupled, centralized, cooperative and greedy approaches were compared.

In this chapter, a multiple UAVs cooperative Nonlinear Model Predictive Control solution to search a given area is proposed. The coordinated turn vehicle model is implemented considering the effects of wind. The search area is divided into cells and each cell has an associated reward, that in this work is defined according to the international Search and Rescue directives. The algorithm is fully implemented in an embedded system to run in the UAV on-board computer and interfaced to the flight controller board. A Software-In-The-Loop (SITL) environment with flight dynamics simulations is used to test the solution.

As mentioned, research about the use of receding horizon techniques for exploration is limited. Also, the solutions found in the literature are developed with simplified vehicle models, in which the effects of wind are not considered either. In addition, the solutions are only simulated in environments without embedded programming restrictions and where vehicle dynamics are not simulated. This makes results not close enough to what is expected from real-life applications. Implementing the solution in an embedded software for real-time applications brings additional challenges such as communication delays, processing time, actuator limitations, among others. This chapter contributes to the field by filling this gap in the literature.

The main contents of this chapter are the following. First, the exploration Model Predictive Control problem is detailed including a coordinated turn kinematic model that takes the wind into consideration. Second, a finite time horizon grid

search cost function with cells rewards and terminal cost is proposed. Third, the algorithm is fully implemented in an embedded software and tested in a real-time SITL environment that also simulates the flight dynamics, bringing results that are very close to reality. Forth, international SAR directives are used to define the performance indicators and the mission scenario in order to test the solution in a relevant case.

B.2 Optimal Control Problem

B.2.1 Coordinated Turn Model

A two-dimensional kinematic model is used based on the Coordinated Turn model [8] [117] [109] [9] [24]. In this model, the UAV turns by changing its roll angle and therefore there is no net side force acting on the UAV.

As wind is a major issue on UAV missions as it can likely reach more than half of the UAV's maximum airspeed, the Coordinated Turn model used in this project was developed to consider the influence of wind on the UAV kinematics.

For level flight in the presence of wind:

$$\begin{pmatrix} \dot{x} \\ \dot{y} \\ \dot{\chi} \end{pmatrix} = f(\mathbf{x}, \mathbf{u}) = \begin{pmatrix} v_g \cos\chi \\ v_g \sin\chi \\ \frac{g}{v_g} \tan u_\phi cos(\chi - \psi) \end{pmatrix}, \tag{B.1}$$

where g is the gravitational acceleration of 9.81 m/s^2, $\mathbf{x} = (x, y, \chi)$ are the north and east positions in the NED frame in [m] and the course angle in [rad], respectively. $\mathbf{u} = (u_v, u_\phi)$ are the airspeed control input in [m/s] and roll control input in [rad], respectively, and with the ground speed (v_g in [m/s]):

$$v_g = \sqrt{(u_v \cos\psi + v_w \cos\psi_w)^2 + (u_v \sin\psi + v_w \sin\psi_w)^2}, \tag{B.2}$$

where v_w is the wind speed in [m/s], ψ_w is the wind heading in [rad] and with the aircraft heading (ψ in [rad]) calculated using the law of sines:

$$\psi = \chi - \arcsin\Big(\frac{v_w}{u_v} \sin(\psi_w - \chi)\Big). \tag{B.3}$$

The model is discretized by the forward Euler method:

$$\mathbf{x}_{k+1} = f_d(\mathbf{x}_k, \mathbf{u}_k) = \mathbf{x}_k + T_s f(\mathbf{x}_k, \mathbf{u}_k), \tag{B.4}$$

where T_s is the sampling period.

B.2.2 Model Predictive Control Problem

To reach the mission goal, a centralized optimization approach might not be feasible because the problem would be too complex with too many control inputs. In a non-convex problem with a very long vector of variables to optimize, falling very early in a local minima is a common issue. In addition, the necessary processing power to optimize so many control inputs would be difficult to achieve by the on-board processing unit of the UAV. In the other hand, optimizing the controls of all UAVs in a ground station would not be an ideal solution, due to communication range limitations and because that in case of a communication failure, the UAVs would not receive its controls, which could compromise the mission.

Therefore, in this research, the problem is addressed as a cooperative control problem, where each UAV optimizes its own control inputs to update its state so that a local cost function is minimized. The cost function also takes into consideration the planned states of the other UAVs. As each UAV follows the same process, it is expected that the global mission goal is achieved cooperatively. Collision avoidance between UAVs is also considered.

Considering I UAVs ($\mathbf{x}^i, \forall i \in \{0, ..., I-1\}$), the algorithm finds a control input sequence $U_k^i = \{\mathbf{u}_0^i, \mathbf{u}_1^i, ..., \mathbf{u}_{K-1}^i\} \in R^{2\times K}$ for the ith UAV, which solves the following optimal control problem:

$$\begin{aligned}
\text{minimize} \quad & \delta(\mathbf{C}\bar{\mathbf{x}}_K) + \sum_{k=0}^{K-1} L^i(\mathbf{C}\bar{\mathbf{x}}_k, \mathbf{u}_k^i) && \text{(B.5)}\\
\text{subject to} \quad & \mathbf{x}_{k+1}^i = f_d(\mathbf{x}_k^i, \mathbf{u}_k^i), && \text{(B.6)}\\
& v_{a_{min}} \leq u_{v_k}^i \leq v_{a_{max}}, && \text{(B.7)}\\
& \phi_{min} \leq u_{\phi_k}^i \leq \phi_{max}, && \text{(B.8)}\\
& |\mathbf{C}(\mathbf{x}_k^i - \mathbf{x}_k^j)| > r_c, \forall j \in \{0, ..., I-1\}\backslash\{i\}, && \text{(B.9)}
\end{aligned}$$

where

$$\delta(\bar{\mathbf{x}}_K) = F(\mathbf{C}\mathbf{x}_K) - aJ(\mathbf{C}\bar{\mathbf{x}}_K), \tag{B.10}$$

and

$$L^i(\mathbf{C}\bar{\mathbf{x}}_k, \mathbf{u}_k^i) = aJ(\mathbf{C}\bar{\mathbf{x}}_k) + b(u_{v_k}^i - u_{v_{k-1}}^i)^2 + c(u_{\phi_k}^i - u_{\phi_{k-1}}^i)^2. \tag{B.11}$$

Consider $u_{v_{-1}}$ and $u_{\phi_{-1}}$ as the commanded airspeed and roll angle, respectively, in the previous optimization loop, $\bar{\mathbf{x}}_k = [\mathbf{x}_k^0, ..., \mathbf{x}_k^{I-1}]$ as the states of all UAVs, K as the number of horizon steps and r_c as the minimum safe distance between the UAVs to avoid collision. a, b, c are constant weighting factors and $\mathbf{C} \in R^{2\times 3}$ is used to define that only the x (north) and y (east) positions are used from the state vector:

$$\mathbf{C}_1 = \begin{bmatrix} 1 & 0 & 0 \\ 0 & 1 & 0 \end{bmatrix}. \tag{B.12}$$

The function J represents the grid search function, which is the sum of the rewards of unvisited cells. F is the terminal cost (cost-to-go) function, which is the distance from the terminal position to the unvisited cell with highest reward. Both functions are described in detail in Section B.4.

B.3 SAR directives applied to UAVs equipped with remote sensing

The Search and Rescue (SAR) consists, according to the Department of Defense (DoD) of the United States of America, in "the use of aircraft, surface craft, submarines, and specialized rescue teams and equipment to search for and rescue distressed persons on land or at sea in a permissive environment" [28]. This work focuses on the sea cases, therefore, the following description emphasizes sea SAR missions. Also, as only Unmanned Aerial Vehicles (UAVs) are used in this work, only the directives for aircraft facilities are studied.

B.3.1 Search Area

According to the International Aeronautical and Maritime Search and Rescue (IAMSAR) Manual [74], the Total Adjusted Search Area (A_t), which is the mission's actual search area, is calculated based on the Total Available Search Effort (Z_{ta}), the Optimal Search Area (A_o) and the targeted Probability of Detection (POD). The first is a measure of the total area that a set of search facilities can effectively search within limits of search speed, endurance, and sweep width. The second is the search area which will produce the highest probability of success

when searched uniformly with the search effort available and is essentially calculated based on the leeway and the Datum probable position error. Leeway is the the movement of a search object through water caused by winds blowing against exposed surfaces and Datum is a geographic point, line, or area used as a reference in search planning, such as the "Last Known Position" or the "Estimated Incident Position".

If the Total Available Search Effort (Z_{ta}) is smaller than the Optimal Search Area (A_o), a strategy must be chosen to balance the Probability of Detection (POD) and the Total Adjusted Search Area (A_t). Usually, the chosen strategy is to fly on higher altitudes, increasing the sensor's footprint or the crew's field of view while decreasing the POD. However, in this work, as UAVs equipped with automated remote sensing are assumed to be used, resolution requirements usually can not be relaxed. Therefore, no trade-off between the POD and the search area is made and the POD is set to its maximum value of one, which makes the Total Adjusted Search Area (A_t) equal to the Total Available Search Effort (Z_{ta}).

In order to calculate the Total Available Search Effort (Z_{ta}), the sweep width (W) must be defined. When employing UAVs equipped with automated remote sensing in such missions, the sensor being used has a direct influence on this parameter. Altitude, view angle and image quality may affect the capability of identifying a survivor or an object on the sea. This is specially important to be taken into account because if the image does not contain the object of interest properly recorded, the computer vision algorithm will not identify it, independently of the ability that the algorithm has on identifying an important occurrence on an image. This can occur due to low image quality or too long sensing distances, making the object of interest imperceptible.

In the IAMSAR manual, the sweep width is calculated based on the altitude of the aircraft, the visibility and the sensor system specifications. In SAR sea missions with aircraft facilities and visual search, the Corrected Sweep Width (W) is adjusted regarding the weather, velocity and crew fatigue correction factors. However, these factors can be excluded from the equation when automated remote sensing systems are used and the system's velocity constraints are respected. Therefore, in this work, the Corrected Sweep Width (W) is considered equal to the original Uncorrected Sweep Width (W_u).

Finally, the Search Effort (Z_a), which represents the area which can be covered by a specific facility, is calculated by:

$$Z_a = V \times T \times W, \tag{B.13}$$

where V is the Search Facility Speed (average speed) in [m/s], T is the Search Endurance in [s] and W is the Sweep Width in [m].

Note is that the Search Endurance is the time available for the facility to fly looking for the survivors. The IAMSAR manual considers this time as 85% of the lower value between the Daylight Hours Remaining and the On-Scene Endurance. This is due to the fact that human crew is often only able to search with visible light. Despite of it, UAVs are often capable to equip sensors that are not affected by that, such as infrared cameras, which allows the task to be held even along the night. This is a considerable advantage of using UAVs equipped with remote sensing systems.

By summing the Search Effort of all facilities, the Total Available Effort (Z_{ta} in [m^2]) can be found:

$$Z_{ta} = \sum_{f=1}^{F} Z_{af}, \tag{B.14}$$

where F is the number of facilities.

As described above, in this work the Total Adjusted Search Area (A_t) is equal to the Total Available Effort (Z_{ta}). Therefore, for Single Point Datum, the Length and the Width of the search area are given by the square root of the Total Available Effort (Z_{ta}) as defined by the IAMSAR manual.

B.3.2 Probability Map

The Probability of containment (POC) distribution in the search area is very important to guarantee an efficient employment of the SAR facilities. When the initial indications do not provide enough information about the area, a standard distribution is assumed. The two most used types of standard distributions are the standard normal distribution and the uniform distribution, according the nature of the datum. For datum point and lines, the standard normal distribution is used. For datum areas, the uniform distribution is the most used. In this work, only the single point datum is studied. Single point datum occurs, for example, when there is no significant leeway (e.g. when the target is a person in water [16]).

The probability map is a set of grid cells where each cell is labelled with the probability of containing (POC) the search object in that cell. As the the probability map follows a probability distribution function, the total sum of all cells should be equal to 100%. An example of probability table for single point datum with 12×12 cells is shown in Figure B.1:

Figure B.1: Initial probability table. Source: IAMSAR Manual

B.4 Cost Function

An exploration cost function was developed based on [139] to search a given area. The region of interest is divided into $M \times N$ square cells of a width (r_e in [m]), which value must be chosen to be smaller than the optical imaging sensor's footprint radius (R_e in [m]) times the square root of 2. The sensor radius is equal to the radius of the circle inscribed in the sensor's footprint. Figure B.2 shows an example of a 4×4 grid with 100 m of cell width (r_e) and a UAV at position $\mathbf{Cx}$ equipped with a sensor with 100 m of radius (R_e).

The matrix $\mathbf{B}^i \in R^{M \times N}$ is used to identify if a cell was visited by the ith UAV. The matrix $\mathbf{b}^i \in R^{M \times N}$ is used to identify if a cell is planned to be visited by the ith UAV in the MPC horizon. In every $M \times N$ matrix used to identify if the cells are visited, each element has an associated value of 1 if the referring cell is visited or 0 if it is unvisited. Each cell has also an associated reward, given by $\phi \in R^{M \times N}$. The function $J(\bar{\mathbf{x}}_k)$ is the sum of all cells associated value (1 or 0) in the step k times the correspondent reward:

$$J(\bar{\mathbf{x}}_k) = \sum_{m=0}^{M-1} \sum_{n=0}^{N-1} \phi_{mn} y_{mn_k}(\bar{\mathbf{x}}_k), \tag{B.15}$$

with

$$\begin{aligned} y_{mn_k}(\bar{\mathbf{x}}_k) =& (\|\mathbf{Cx}_k - r^1_{mn}\| < R_e \wedge \|\mathbf{Cx}_k - r^2_{mn}\| < R_e \wedge \\ & \|\mathbf{Cx}_k - r^3_{mn}\| < R_e \wedge \|\mathbf{Cx}_k - r^4_{mn}\| < R_e) \vee y_{mn_{k-1}}, \end{aligned} \tag{B.16}$$

where r^1_{mn}, r^2_{mn}, r^3_{mn} and r^4_{mn} are the four vertices of the cell (Figure B.2) and $y_{mn_{k-1}}$ is the associated value of the cell in the previous horizon step.

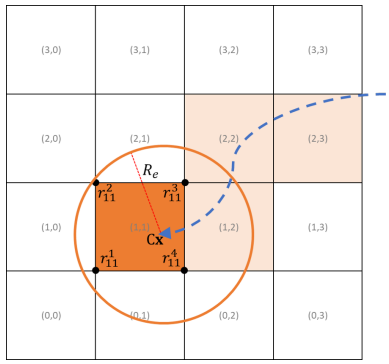

Figure B.2: Cells grid example.

The starting value of y_{mn_0} is given by the logical sum of the matrices of already visited cells of all UAVs and the matrices of cells planned to be visited by other UAVs:

$$y_{mn_0} = \mathbf{B}^i_{mn} \vee \mathbf{B}^j_{mn} \vee \mathbf{b}^j_{mn}, \forall j \in \{0, ..., I-1\} \backslash \{i\}. \tag{B.17}$$

Finally, $F(\mathbf{x}_K)$ is the terminal cost. This function is necessary for the algorithm to consider the search beyond the prediction horizon by having a *cost-to-go* term. It is given as the minimum euclidean distance from the latest state of the UAV in the horizon, to the center of the closest unvisited cell, weighted by the correspondent reward, in the end of the horizon:

$$F(\mathbf{Cx}_K) = \min_{\forall m \in O, \forall n \in P} \frac{\|\mathbf{Cx}_K - \mathbf{r}_{mn_K}\|}{\phi_{mn}}, \tag{B.18}$$

where $O \subseteq M$ and $P \subseteq N$ are subsets of all unvisited cells and $\mathbf{r} = [x, y]$ are the north and east positions of the cell's center.

B.5 Embedded System

The path-planning algorithm was implemented as a task in DUNE: Unified Navigation Environment [108]. DUNE is a software framework that allows the operation of a wide variety of robots using the same environment. This facilitates the development because the communication between DUNE and the different control units is transparent to the user.

Regarding the communication with the UAV control unit, it connects DUNE and the Ardupilot [131] autopilot via MAVLink Micro Air Vehicle Protocol [132]. To command the Ardupilot, the task must dispatch a message with the desired command, which will be interpreted by DUNE's Ardupilot control task and then sent to the Ardupilot via MAVLink.

The communication between DUNE tasks is done via the IMC: Intermodule Communication API protocol [108], which is also part of LSTS' toolchain. This protocol basically works by dispatching and consuming messages. So, if a message is dispatched by a task, another task that is waiting for that message will consume it.

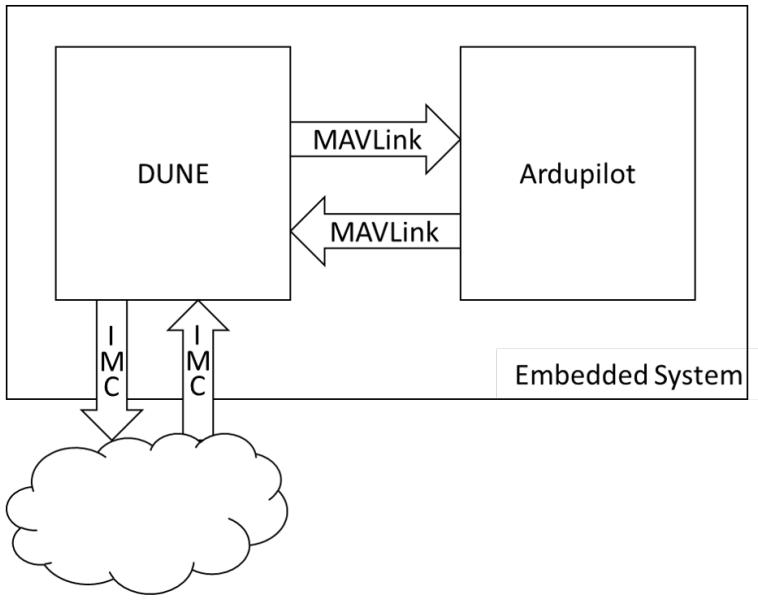

Figure B.3: Simplified embedded system block diagram.

Figure B.3 shows a simplified block diagram describing how the embedded system blocks are associated. DUNE communicates with the Ardupilot via MAVLink and with other UAVs and ground station via IMC. The systems must be in the same network and IP addresses and TCP and UDP ports must be configured.

Inside DUNE resides the MPC task, which is outlined at Figure B.4. The commands to control the UAV are given by the DesiredSpeed and DesiredRoll IMC messages, which carry, respectively, the airspeed and roll control inputs given by

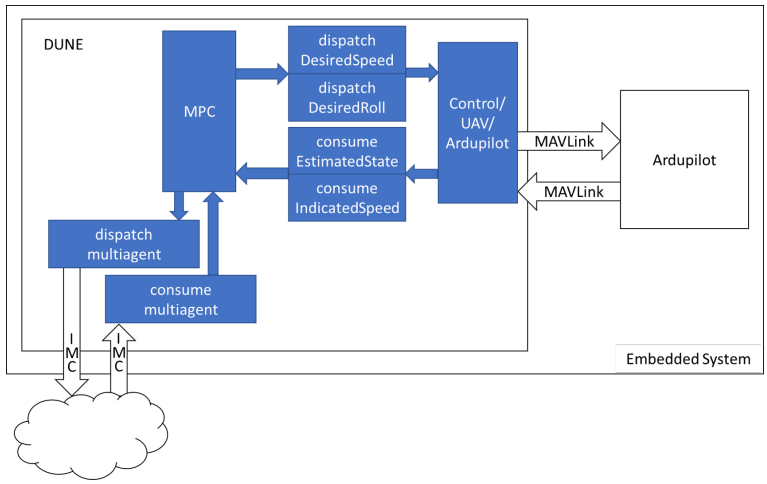

Figure B.4: Simplified DUNE block diagram.

the optimization. These messages are interpreted by the Ardupilot control task, that sends the correspondent MAVLink message to the Ardupilot. The Ardupilot control task is also responsible for receiving the pose and attitude information of the UAV and to dispatch it in the IMC messages EstimatedState and IndicatedSpeed. These messages are consumed by the MPC task to be used as the current state of the UAV.

The communication between the UAVs is done by the multiagent message, which was created and included in the IMC messages list specifically for this application. This message carries the information that the UAVs need to share, such as planned control inputs and current state.

Each UAV waits for the multiagent messages from all other UAVs before running the MPC optimization. Once all messages are received, the optimization is done and then the UAV dispatches its multiagent message containing all information that need to be shared with the other UAVs. This flow is described in Figure B.5. It is important to mention that the UAV states are predicted according to the communication and MPC delay and to the planned control inputs before being used by the MPC algorithm. Therefore, the control inputs that are obtained by the MPC optimization and sent to the Ardupilot correspond to the predicted state that is expected to be close to the real state of the UAV after the MPC optimization.

Note that, in an extension of the method, measures can be employed to protect the system from communication failures, so that the UAV does not wait for delayed messages for too long.

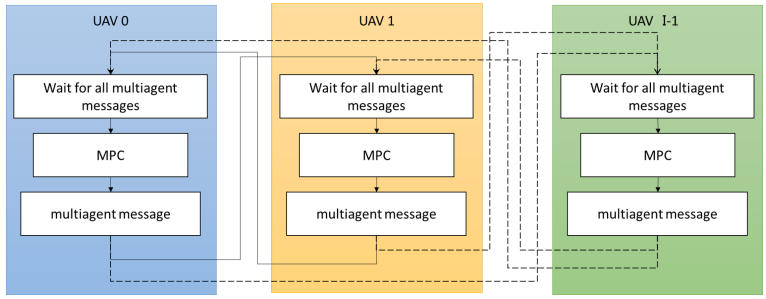

Figure B.5: UAV agents flowchart.

B.5.1 Optimization Technique

In this application, the Particle Swarm Optimization (PSO) [34] technique is used to find an optimal set of airspeed (u_v) and roll angle (u_ϕ) that minimizes the cost function. PSO, which is described in the Appendix D, is a meta-heuristic optimization method where the particles (solutions) are updated every iteration based on the best global and local solutions. In this application, a standard PSO algorithm was implemented using CUDA C programming language in order to benefit from the parallelism of the Nvidia Graphics Processing Unit that is assumed to be used in the UAV on-board computer.

The algorithm was set to run a fixed number of iterations on every loop. In addition, the number of particles must be defined. These two parameters affect the processing time and need to be fine-tuned according to the requirements.

The initial solutions are initiated with random values following the uniform distribution, where the minimum and maximum values are the defined boundaries of the airspeed and roll angle control inputs.

B.6 Software-In-The-Loop environment

To evaluate the proposed solution, a Software-In-The-Loop (SITL) environment was set up. In this environment, the original Ardupilot and DUNE embedded software are used. The aircraft platform is simulated by JSBSim [11], an open source Flight Dynamics Model. Therefore, it is able to compute the UAV dynamics according to the actuator controls of the Ardupilot.

The JSBSim was modified to use in its calculations the same wind map that is used by the MPC optimization. Also, an aircraft platform model must be chosen for JSBSim flight dynamics calculations. In this work, the X8 UAV (Figure B.6) model [51] was used.

Figure B.6: X8 UAV. (Source: NTNU)

Figure B.7 shows the interconnection between modules. For each UAV, an Ardupilot SITL instance must be started linked to a JSBSim module. Each Ardupilot instance uses a different TCP port. Therefore, one DUNE module must be started for each UAV, set with the correspondent TCP port. Finally, Neptus [108], a command and control software which is also part of the LSTS' toolchain, is used to visualize the UAVs telemetry and location and to give commands to the UAVs, such as take off, loiter and to start/stop the Search and Rescue mission.

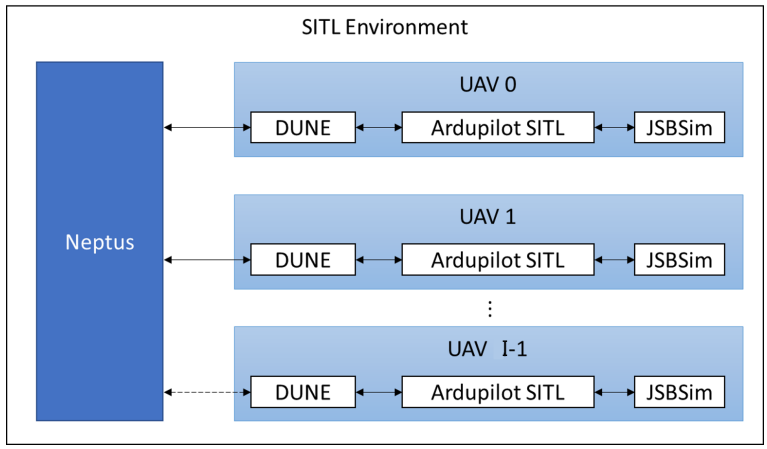

Figure B.7: Software-In-The-Loop setup.

B.7 Mission Simulation Scenario and Parameters

In this section, the parameters that define the mission scenario are described.

B.7.1 Aircraft platform

In this work, the Skywalker X8 UAV (Figure B.6) was chosen to be the aircraft platform. The X8 is a battery powered small UAV which can fly for around 80 min with the automated remote sensing payload and proper battery. The radius of the remote sensor is equal to 200 m, which is half of the width of the sensor's footprint. This footprint was chosen assuming that a computer vision algorithm,

such as the one described in [115], can detect the target in images captured at 400 m of altitude by an infrared camera with 7.5 mm of lens focal length, 640 × 480 pixels of resolution and 17 μm of pixel size.

B.7.2 Search Domain

The reference search area used in this work is equivalent to the Search Effort (Z_a) of one X8 UAV, calculated by Equation B.13. Considering the total endurance of 80 min, the On-Scene Endurance (T) is equal to 60 min (85% of the total endurance). The Search Facility Speed (V) is equal to the average airspeed of the aircraft, in this case 16 m/s. The Sweep Width (W) is equal to 400 m, which is the lateral length of the required sensor footprint. Therefore, the search area is equal to 23.04 km^2, which gives a length and width equal to 4.8 km as the area has a squared shape because the datum is a single point.

B.7.3 Cells Grid

The grid was built with a cell width of 100 m. Therefore, the 23.04 km^2 were divided into 48 × 48 cells.

A two dimensional normal distribution curve was fitted to the single point datum reference table provided by the IAMSAR manual (Figure B.1).

The fitted curve of the probability (Figure B.8), that gives the reward of each cell is given by:

$$\phi_{mn} = 0.002946 \exp\Big(- \Big(\frac{(m-23.5)^2}{108.28} + \frac{(n-23.5)^2}{108.28} \Big) \Big) \tag{B.19}$$

where m and n are the horizontal and vertical indexes of the cell, respectively.

B.7.4 MPC Parameters

The boundaries and constraints of the control problem were chosen as follows.

The airspeed range was chosen to be between 12 to 22 m/s. The reason for this choice was to keep the airspeed around the cruise speed, so that the battery consumption does not get too high. The roll angle range was chosen to be between -45 and 45 degrees so that the aircraft performs smoother maneuvers but still with freedom. The safe distance between UAVs was chosen to be 100 m and a wind of 9.9 m/s pointing to 45 deg was considered both in the optimization and in the flight dynamics simulation. The time horizon of 20 s and 20 horizon steps were the parameters chosen for the MPC problem. With, for example, a ground speed of 17

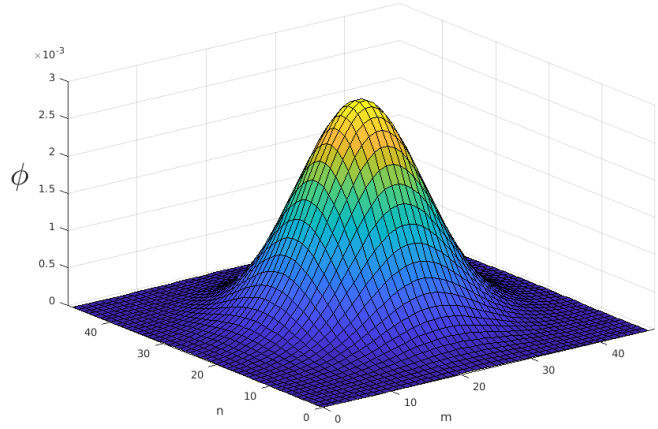

Figure B.8: Reward of cells.

m/s, this means 340 m of straight distance, or a 180 deg turn. The weighting factor a was chosen to be 10000, because the rewards are of a very low value (the sum of all cells rewards is equal to one). The weighting factors b and c were chosen to be 0, so the algorithm does not consider the airspeed and roll angle constraints for aggressive maneuvers. Therefore, the algorithm is free to only consider the search performance in the optimization.

Regarding the PSO parameters for the optimization, a total of 384 particles was used and the algorithm runs 35 iterations with local and global coefficients of 1.

B.7.5 Simulation platform

With these parameters, each UAV is able to run the optimization in around 400 ms when 3 UAVs perform the optimization at the same time. The optimization algorithm was written in CUDA C programming language in order to benefit from the parallelism, with the goal to embedded it on a NVIDIA Jetson board in the future for field tests.

The simulations were run in a laptop with the NVIDIA 940MX graphics card, which has around five times processing power more than the NVIDIA Jetson TX2, according to performance tests available in the manufacturer's website. Therefore, it is expected that the embedded board will also be able to run the optimization at 400 ms with just a fine tunning of the parameters. Another possibility is to implement a optimization stopping feature that will run as many iterations as possible within a given time, instead of a fixed number of iterations.

It is also relevant to mention that the optimization time was adjusted to 400 ms also when using only one or two UAVs. This was done by inserting a delay, so the optimization time in each UAV is the same for simulations when one, two or three UAVs are used. Therefore, this gives a fair comparison of the results.

B.8 Results and Discussion

Three operational profiles were evaluated for the mission scenario: employing only one UAV; employing two UAVs; or employing three UAVs. Five missions were executed for each one of the profiles in order to obtain the average performance.

The reference search area was the Total Adjusted Search Area (A_t) for one UAV facility and Probability of Detection (POD) equal to 1, as described in the previous sections.

The area was kept the same when employing two or three UAVs in order to allow a proper performance comparison between the profiles. Figure B.9 illustrates one mission with three UAVs being monitored by the Command and Control software Neptus. The light red area is the search area and the dark red cross in the middle is the single point datum.

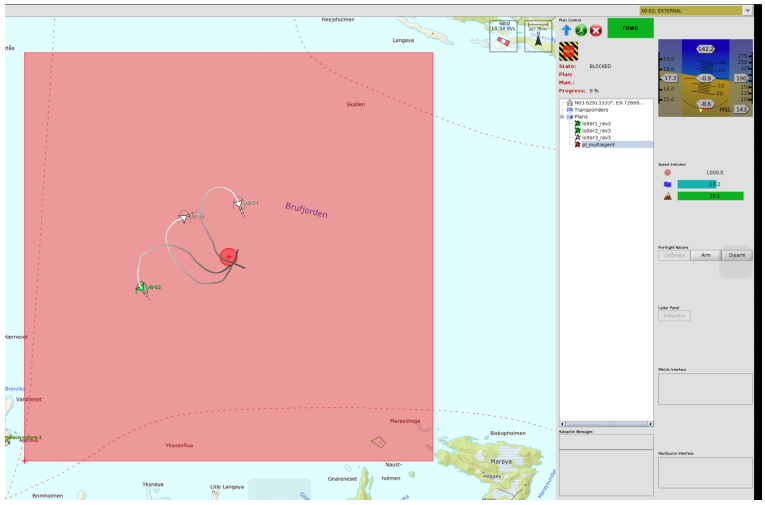

Figure B.9: Snapshot of a mission with 3 UAVs being monitored with Neptus.

In all missions the UAVs departed from the same region (southeast of the search area as shown in Figure B.10) where they were loitering and waiting for the command. After receiving the command, the UAVs departed to the search area and the mission time started to count from when the first UAV collected the first reward.

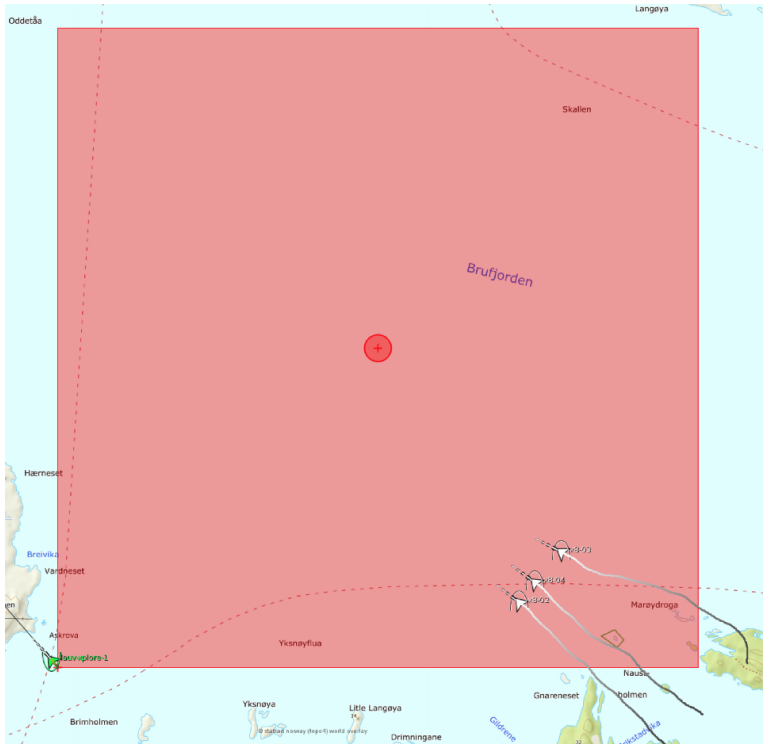

Figure B.10: Snapshot of the beginning of a mission.

The IAMSAR manual describes the Probability of success (POS) as the probability of finding the search object with a particular search. For each sub-area searched, $POS = POD \times POC$. It is therefore the way to measure search effectiveness. As the Probability of detection (POD) is kept at 1, the POS is equal to the POC of the searched area, which in this work is the sum of all rewards collected by the group of UAVs.

The boxplot of the time to reach 50% of POS is shown in Figure B.11 for the three operational profiles: employing one; two; or three UAVs. It is possible to notice that the gain when a pair of UAVs is used is very significant when compared to the single UAV profile, reaching 50% of POS 75% faster. When adding a third UAV, the gain was less significant: on average, the group reached 50% of POS 28% faster than when employing a pair of UAVs. The decrease on the gain is probably due to the fact that the UAVs are often flying over areas that have already been flown. A possible solution to avoid this situation is to reduce the width of the cells, increasing the resolution of the grid. Therefore, the UAVs would better tune their maneuvers and still have the cells inside the UAVs' sensor radius. However, this will increase the required computational power. This issue could be mitigated by

optimizing the algorithm, for example.

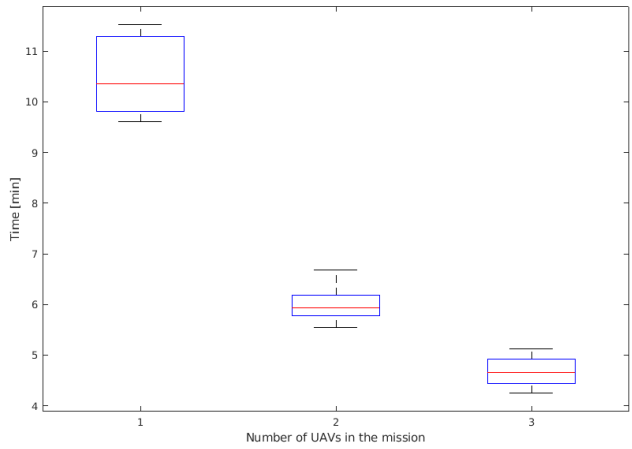

Figure B.11: Time to reach 50% of Probability of success (POS).

Figure B.12 shows the average POS during 20 min of mission. It is possible to notice that the results match the observed behavior when the missions were monitored. From the mission start to around 4 min the UAVs fly to the area close to the datum, where the reward (Probability of containment) is higher. When two UAVs are employed, they fly parallel so that they cover more cells than when employing a single UAV. However, when three UAVs are employed, even if they form a parallel path, they fly close to each other and, therefore, do not visit more cells than the pair of UAVs. This happens because in case the three UAVs get far enough from each other to not visit the same cells, they would take a longer path to arrive at the central area (highest rewards), not being a cost beneficial solution.

After reaching the area close to the datum at around 4 min, the curve of rewards collection grows steadily and the difference between the three operational profiles is clear. When three UAVs were employed, the group reached 50% of POS 2.25 times faster than the single UAV. The gain, however, reduces over time. For example, to reach 65% of POS, the group of three UAVs did it 2.04 times faster than the single UAV. The reason of the decrease on the gain is that the more cells are already visited and rewards collected, further the UAVs have to fly to visit new cells and collect new rewards (that are also lower in value). Therefore, the closer it is to the end of the missions, smaller is the difference between the performance of the different operational profiles.

Figure B.13 shows the boxplot of the POS after 20 min of mission for the three

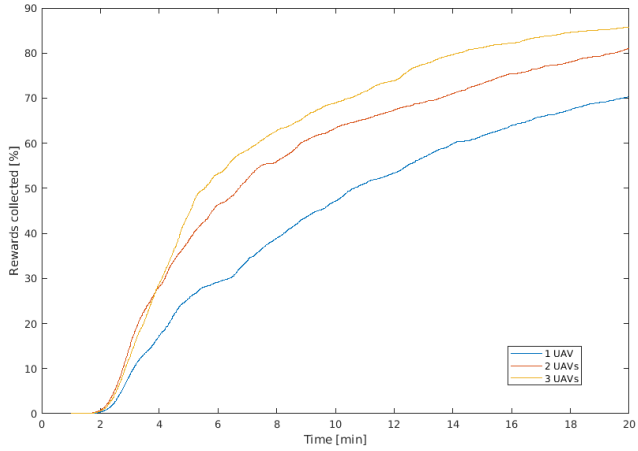

Figure B.12: Average Probability of Success in time.

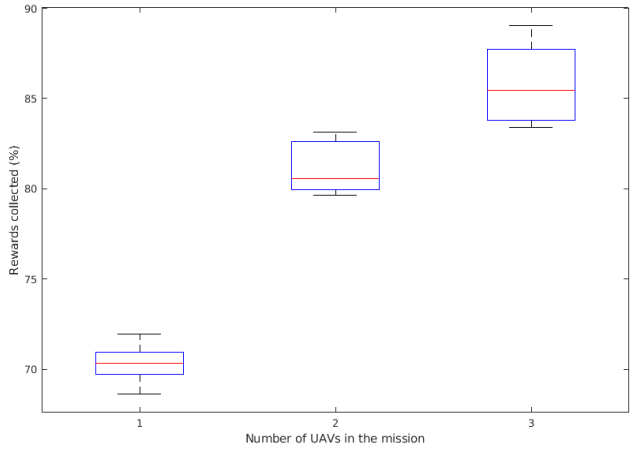

Figure B.13: Probability of success (POS) in 20 minutes of mission.

operational profiles. According to the IAMSAR Manual calculations, the single UAV is expected to reach 100% of POS in 60 min. It is possible to notice that the group of three UAVs is able to reach close to 90% of POS in 20 min, showing that the improvement of adding extra UAVs is approximately linear.

Finally, a pre-made path where the UAV flies from the origin to the grid midpoint then flies a spiral path was created (Figure B.14) in order to compare to the performance of the single UAV with the real-time MPC optimization. This spiral

path is close to the standard path suggested by the IAMSAR Manual.

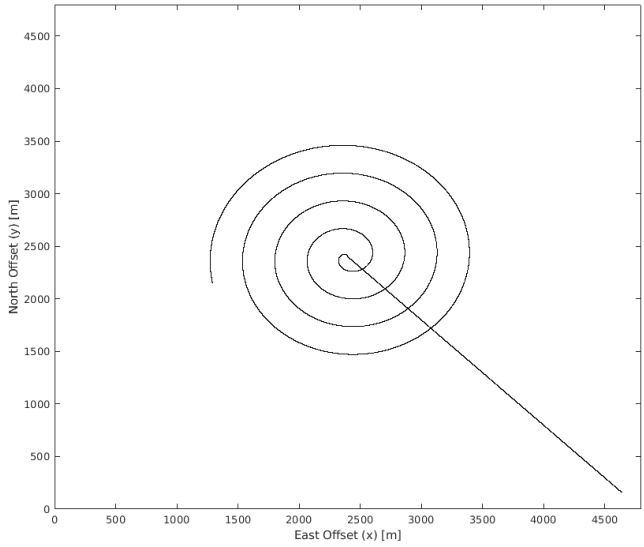

Figure B.14: Spiral path.

In the spiral path, the lanes are equally spaced allowing the best coverage by the sensor's footprint. This would be the best possible simple standard path for the mission scenario being investigated. Also, the UAV is assumed to first fly to the center of the area and then start the spiral path.

Figure B.15 shows that for the same average airspeed of 15.5 m/s, the performance of the MPC path-planning was superior in the first 20 minutes of mission. Also, in the spiral path, 50% of POS was reached in around 13 min, while it took less than 11 min when the MPC optimization was used.

In the spiral path, wind was not considered and the UAV keeps the ground speed constant, while in the MPC path-planning the UAV optimizes its speed to reach higher coverage, for example reducing the airspeed to achieve a steeper turn when needed. Another advantage, that is perhaps the most important, is that the MPC solution has the capability to deal with dynamic changes in the environment and mission parameters during the mission, as it is a real-time optimization. These changes can be wind variations, updated search and rescue reports or even the lost of one UAV in the middle of the mission due to technical problems or the addition of extra UAVs that arrived later when the mission had already started.

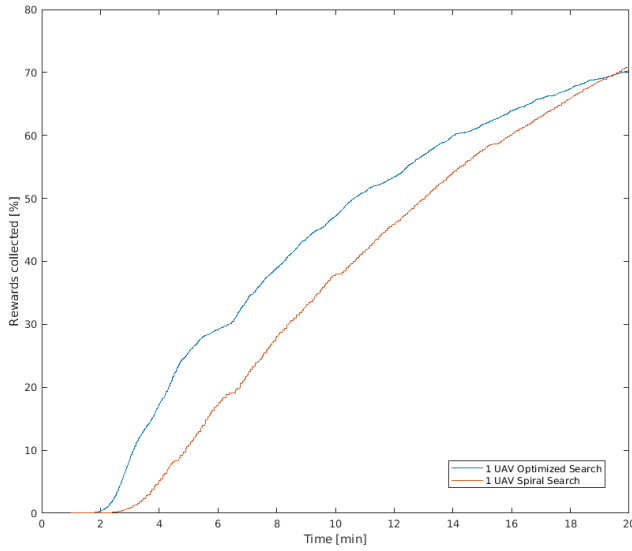

Figure B.15: Probability of Success.

B.9 Conclusions

In this chapter, a real-time path-planning for search and rescue with Model Predictive Control solved by Particle Swarm Optimization was proposed. The solution was implemented on a fully embedded software and tested in a Software-In-The-Loop environment with flight dynamics simulations. The search area was defined using the International Aeronautical and Maritime Search and Rescue (IAMSAR) directives. Also, the area was divided into a grid of cells, where each cell had a correspondent reward, referred to the IAMSAR's Probability of containment. Results were analyzed for missions where one, two or three Unmanned Aerial Vehicles (UAVs) were employed. To reach 50% of Probability of success, the performance of the group of three UAVs was on average 2.25 times faster than the single UAV search. The performance of the single UAV was also compared to a standard search pattern based on the IAMSAR's suggested pattern. The search using the proposed solution outperformed the standard search pattern in the first 20 min, with the additional advantage of being a real-time method that can deal with environmental dynamic changes and new mission directives.

Appendix C

A Survey of Design Considerations of Optical Imaging Stabilization Systems for Small Unmanned Aerial Systems

Optical imaging systems are one of the most common sensors used for collecting data with small Unmanned Aerial Systems (sUAS). Plenty of research exists which present custom made optical imaging systems for specific missions. However, the research commonly leaves out the explanation of design parameters and considerations taken during the design of the optical imaging system, specially the image stabilization strategy used, which is a significant issue in sUAS imaging missions. This paper surveys useful methodologies for designing a stabilized optical imaging system by presenting an overview of the important aspects that must be addressed in the designing phase and which tools and techniques are available and should be chosen according to the design requirements.

C.1 Introduction

The use of small Unmanned Aerial Systems (sUAS) has increased rapidly during the last years. While some hobby users operate sUAS without any particular purpose, research institutes and corporations commonly operate sUAS for the purpose of collecting information about the environment. Environmental data that can be of interest include readings of the Earth's magnetic field, elevation data acquired by a lidar, and various wavelengths of transmitted and reflected light acquired by a camera system.

Optical imaging systems are one of the most common sensors used for collecting data with sUAS, and their images can be used to take snapshots of beautiful scenery, provide situational awareness to an operator during a mission, and in various photogrammetry applications. Several commercial off-the-shelf optical imaging systems for sUAS exist, in particular, for missions with high requirements on the visual appeal of the images rather than the accuracy of the world time, position, and attitude of the camera when the image was acquired. This is often the case for TV and video production, photographers, and hobby users.

Image meta data such as world time, position, and attitude are however of high importance in many sUAS missions performed by corporations and research institutes. With the fast development of new sensors and methods to improve the accuracy and decrease the cost of acquiring this meta data together with a lack of off-the-shelf customizable imaging systems to test the latest technology with, many have created their own payloads. Plenty of research exists which present custom made optical imaging systems for specific missions [37] [**?**] [87] [**?**] [**?**]. The research shows proofs of concept, which can be very valuable since the image acquisition process is highly complex – experimental data from multiple systems can show how design parameters affect the data quality in general, or it can be used to replicate the system for a similar mission. However, the research commonly leaves out the explanation of design parameters and considerations taken during the design of the optical imaging system, specially the image stabilization strategy used, which is a significant issue in sUAS imaging missions. On the other side of the spectrum, there is research explaining intricate details of the design of inertially stabilized platforms [69] [96].

The present paper aims to contribute with filling this gap in the literature by providing useful guidelines and methodology for designing a stabilized optical imaging system. However, it does not consider more advanced topics for making a finished product such as structural analysis, or broad, non-specific topics such as software design. Therefore, the goal of this article is to give an overview of the important aspects that must be addressed when designing a stabilized optical imaging system and which tools and techniques are available and should be chosen according to the design requirements.

This paper is structured as following. In section 2, the main vibration sources are discussed and the main techniques used to identify and evaluate them, as well as their effect on image quality. As there are different ways to administer the vibration issue, the main techniques are presented in the following sections. First, the mechanical installation of dampers is presented, followed by optical image stabilization and software solutions. Finally, sections 6 and 7 are focused on gimbal

design, including the design considerations, followed by the impact of stabilized image systems on the sUAS aerodynamics. Therefore, in the end, the reader can make the appropriate choice of which techniques to be explored, according to the project requirements and limitations.

C.2 Vibration sources and effect

Vibration is one of the main concerns when designing sUAS camera systems: it potentially adds blur, decreasing the image quality and the potential to distinguish detail in the image, and consequently has the potential to compromise the entire mission. Therefore, it is important that the causes of vibration are understood so that the proper mitigation actions are taken.

C.2.1 Vibration sources in sUAS platform

This section goes through the main sources of vibration in the two main popular designs of sUAS platforms: fixed-wing and rotary-wing small Unmanned Aerial Systems. Some sources are shared between them, such as rotors/propellers, and other sources are fairly unique to each platform (e.g. combustion engine of fixed-wing sUAS).

Fixed-wing platform

In [92], with the objective to choose the most suitable sUAS for LiDAR mapping, the authors studied the vibration, capacity, reliability and stability of many sUAS platforms. With the acquired knowledge about the different platforms, they developed two sUAS especially optimized for the LiDAR mapping. With respect to the sources of vibration on fixed-wing sUAS, the authors based their theoretical analysis on a study performed by [94] about positioning errors on LiDAR systems caused by manned aircrafts platform vibration. In this study, the author enumerates four main sources of vibration on manned fixed-wing aircrafts: engine; external wind flow; internal wind flow within open cavities; and (4) airframe structural motions. Regarding the combustion engine, its noise impinges on the aircraft structures, causing vibrations mainly on the frequency of the engine's rotation speed and also on double frequency, from the reciprocating motion of the piston. The second and third main sources of vibration are both due to turbulent aerodynamic flow. One is caused by the flow over external aircraft structures and the other is caused by the flow and acoustic resonance phenomena within cavities open to the external airflow. However, according to [140], these vibrations can be considered less significant for sUAS due to lower speeds compare to the commercial and military aircraft. Finally, the fourth main source of vibration pointed by [94] is with regards to airframe structural motion caused by maneuvers, aerodynamic buffet, landing,

taxi, etc. Vibration can also be also caused by specific installed items, however, according to the authors, the effect is only locally on the surroundings of the item.

Rotary-wing platform

Battery powered rotary-wing sUAS have the rotors as the main source of vibration [156] [144]. In [144], measurements were performed for three setups: motor without propeller; plastic propeller; and wooden propeller. For the first setup, where no propeller was mounted, low force levels for both radial and axial vibrations were recorded, indicating that propellers are the main sources of vibration. In that case, the frequency of vibration is related to the rotation speed of the rotors/propellers. According to [156], the second main source of vibration on rotary-wing sUAS corresponds to the vibration of the sUAS' structure, mainly the platform and extension arms. However, the frequencies of structural natural frequency vibrations depend on the sUAS structure. [144] compared numerical simulations of the vibrations on a hexacopter structure using finite elements (FE) model with experimental results obtained by the impulse hammer excitation method. The results were satisfactory, achieving a vibration frequency accuracy between 0.047% and 2.852%. In addition, a third source of vibration was identified by [156], caused by the vibration of the payload, such as batteries and other weight sources located on the bottom of the sUAS.

C.2.2 Vibration effect on sUAS image quality

There is not a significant number of studies about the effect of sUAS vibration on image quality. [89] investigated the effects of sUAS vibration on Binary Optical Elements (BOE). BOE is a diffraction imaging element and the diffraction efficiency can be impinged by the vibration of the platform, affecting the image quality. In other words, the relative position between the object point and the optical system changes by the movement of the platform, deteriorating the quality of the image. Therefore, the study simulates the effect of one dimension sinusoidal vibrations with different amplitudes and frequencies on an image with pixel size of 9 µm and integration time of 20 ms (Figure C.1). First, different amplitudes at a constant frequency of 50 Hz are applied (Figure C.2). For 5 µm of amplitude, no significant changes on the quality can be noticed. For 10 µm of amplitude, the image quality is affected, however, a more significant degradation is noticed on the edges of the image than on its center. For 20 µm of amplitude, the whole image gets blurred, and for 40 µm of amplitude, the image quality is heavily affected.

Figure C.3 shows the result when the same vibration amplitude (15 µm) is applied to the image, but with different frequencies. There are not significant differences between Figure C.3a and Figure C.3b. The conclusion is that when a vibration

Figure C.1: Original image [89].

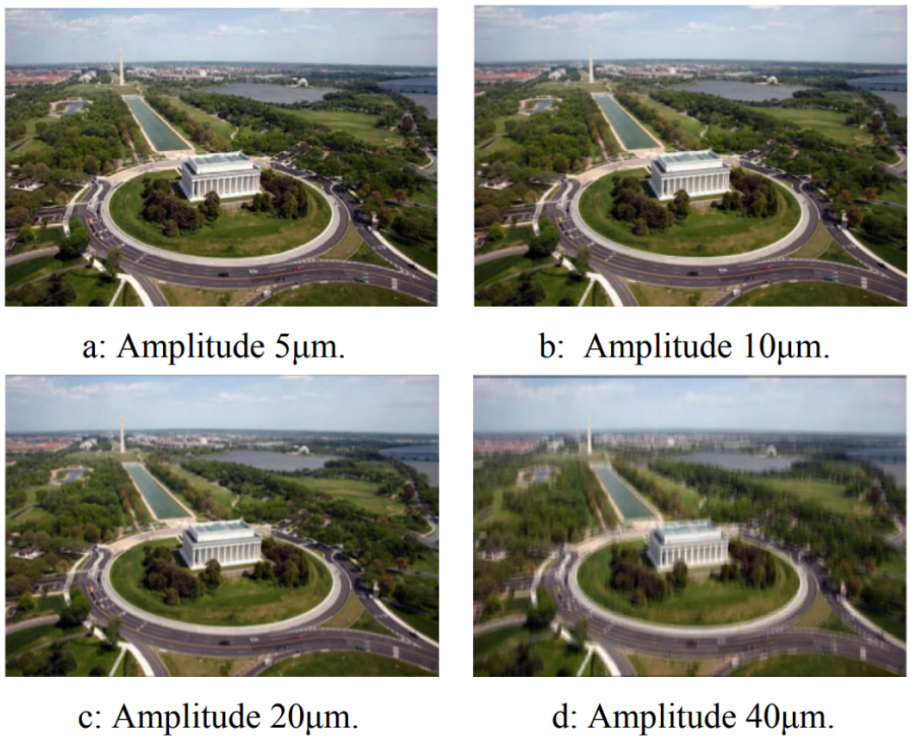

Figure C.2: Vibration simulations with different amplitudes [89].

period is lower than the integration time, increasing the vibration frequency has little effect on the image quality. Figure C.3c and Figure C.3d have the same frequency and amplitude, but the vibration was applied on different moments. This may be due to the varying speed of the camera during sinusoidal vibration. This means that, in case of low-frequency vibrations, the resulting image quality can be different for different time periods since the phase between the vibrations

and the image integration period is likely to shift randomly during a flight.

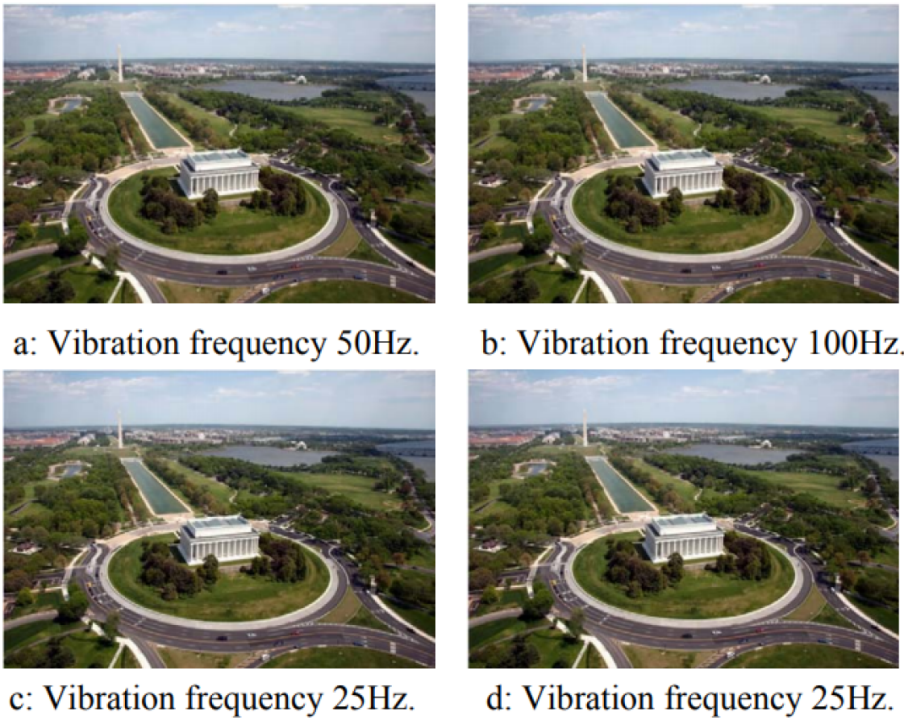

Figure C.3: Simulation with different frequencies [89].

Based on the results, (Li & Tan, 2018) proposes two modifications on the optical system to reduce the effect of vibration on the image quality. As small amplitudes of vibration cause minor effects, one way to reduce the degradation of image quality is to reduce the focal length and increase the pixel size. However, this will result in a decrease in the angular resolution of the optical system, . Another way is to use a CCD (charge-coupled device) with a shorter integration time, so that the vibration period is lower than the integration time.

Other studies that investigated the effect of sUAS vibration on image quality were performed by [56] and [57]. In the latter, the study was not focusing on vibration but also investigating other aspects such as lens calibration, orthorectification and mapping. Both studies worked with images taken on the same research mission and by a Point Grey Research "Flea" camera with a Fujinon YV 2.2 × 1.4 A-2 fish-eye lens mounted both on a sUAS and on a manned aircraft (Cessna 172). In the sUAS setup, the camera was mounted on a small supporting platform that was isolated from vibrations using a special anti-shock material. In the manned aircraft, the camera was mounted on a simple mounting bracket. The main problem

caused by the aircraft vibration was the movement of the lens relative position to the camera (Figure C.4). The authors concluded that the non-interference fit between the camera and the lens housing is responsible for the vibration effect. Also, the problem of vibration is more noticeable on the sUAS, because of its small size, making it more susceptible to maneuvers and turbulence. The comparison between the roll angle noise of the sUAS and the manned aircraft can be seen in Figure C.5. The sUAS has variations approximately twice of the variations on the Cessna 172. In [56], where the focus of the investigation was on vibration effects and compensation, the vibration was divided into rotation and translational vibrations. The largest translational movement detected was ±5 pixels measured from randomly selected images. That is a big issue since vibrations causing only a one-pixel shift in a fisheye image captured by a sUAS operating at an altitude of 1000 ft above the ground would result in a displacement of approximately 2.5 m, using a 0.8 megapixel resolution camera.

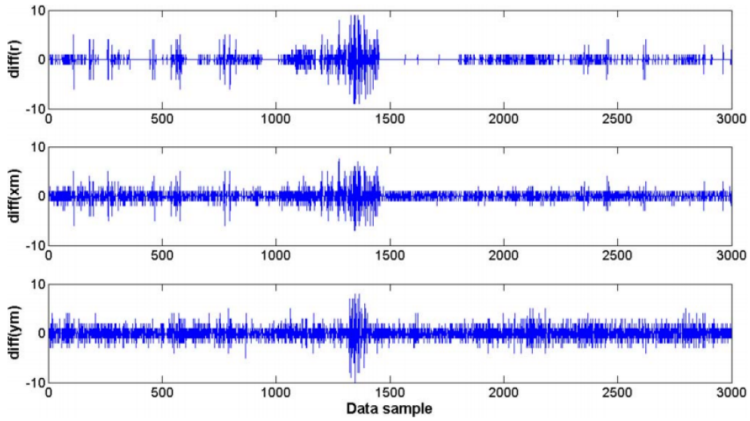

Figure C.4: Estimated displacement of the center of the fish-eye image in pixels (xm,ym) and the estimated radius of the entire fish-eye lens image circle boundary (r) [57].

The available literature about sUAS vibration and image quality is very limited. However, there are a few studies about the effect of mechanical platform vibration on satellite imaging, such as in [60]. In this case, vibrations limit the maximum resolution and performance of remote sensing and are caused by turbines, motors, reaction wheels, actuators etc. The study performed by [60] was based on [152], which analyzed the relation between blur, vibration, exposure time and resolution, with focus on vehicular or airborne imaging systems and in robotic systems. The calculations can be used to determine the most appropriate sensor for a given task, and the number of images of the same scene that are necessary to achieve a required resolution.

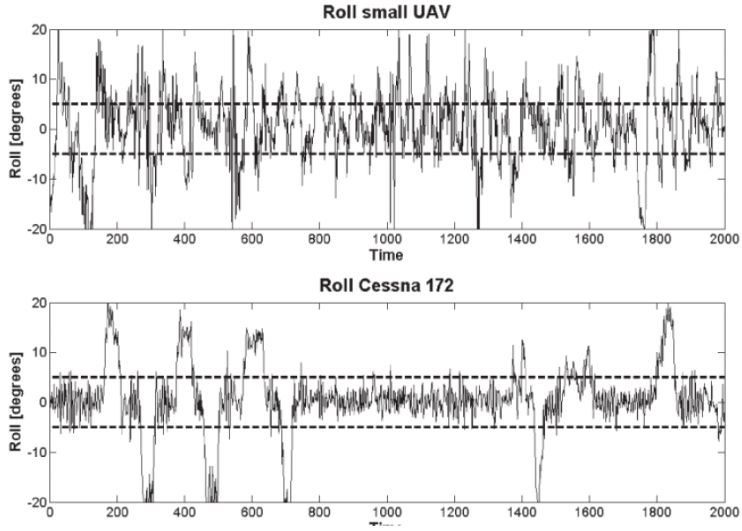

Figure C.5: Comparison of roll angles on sUAS and manned aircraft [57].

C.3 Mechanical Vibration Mitigation

Dampers are very popular devices for vibration mitigation. A wide selection of vibration dampers are available off-the-shelf. The knowledge of how to select the best damper is however not widespread, and it is common to just try a few and see which one works best. By using a more systematic design method together with collected vibration data (or estimated from the vibration sources), it is possible to remove targeted vibration frequencies more efficiently. Since trial-and-error might be resource-intensive in both man-hours and components, a systematic approach is likely to reduce both cost and time of developing a stabilizing system.

Also, to reduce the vibration effects, actions can be taken in the sUAS platform design phase, when selecting the materials and when designing the structure.

C.3.1 Dampers on the optical imaging system

Dampers can be used for vibration isolation, to lower the natural frequency of the system to below the excitation frequency, and for vibration damping, where the aim is to absorb the mechanical energy and convert it to other energy forms, such as heat. Three types of dampers (Silicone Foam; Kyosho Zeal; and Sorbothane 30 Durometer Sheets) (Figure C.6) were tested by [156] to mitigate the vibration on a rotary-wing sUAS. In total, six aspects were taken into consideration when choosing the dampers: 1. Electrical insulator to avoid short-circuit; 2. Soft and flexible; 3. Natural frequency outside sUAS structural resonance zone; 4. Low compression set

and low creep; 5. Good resistance to outdoor conditions; and 6. Easy installation and adjustment.

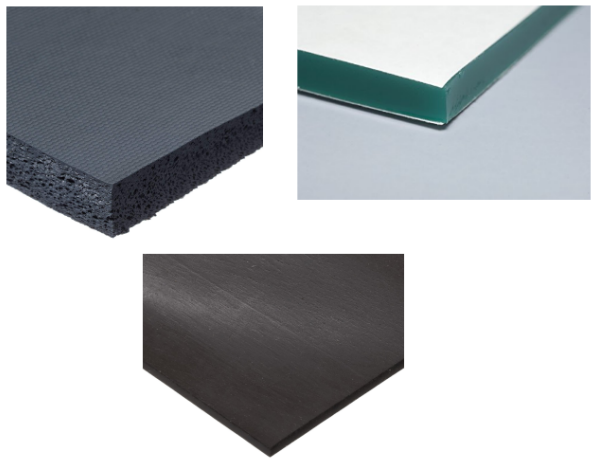

Figure C.6: Silicone Foam (top left); Kyosho Zeal (top right) and Durometer Sheet (bottom) (Adapted from Amazon.com)

To study the effect of the dampers on the sUAS vibration mitigation, a structural vibration analysis was done before the installation of the dampers. In the first step, the sUAS structure was modeled in SolidWorks simulation, considering also the materials properties. The frequency analysis was carried out and the high vibration frequencies observed were 39.90 Hz on the x and y axes, and 80.48 Hz on the z axis. Similar behavior also existed for 160.17 Hz and 321.82 Hz respectively, which the author suspects are the 3rd and 4th mode natural frequencies, related to the payload. Small vibrations were obtained between 100 to 200 Hz and a stronger one at 273.16 Hz. The last ones are probably related to the structure, such as arm extensions and components. After the simulation, flight tests were performed and the vibrations were measured by an additional IMU with a sampling rate above 800 Hz. Results (Figure C.7) show that the vibration data obtained on the flight tests was very similar to the simulated one. Peaks (A) related to the payload were verified on the vibration frequencies of 40, 80, 160 and 320 Hz, a peak (C) related to the structure was verified on around 270 Hz, and another peak (B) was verified on around 50 Hz, which is related to the rotation of the rotors. The last one was not verified in the simulations because the vibration related to the rotation of the rotors was not included on the simulated model.

The tests of the effectivity of the dampers were performed on a lab vibration table for a frequency range from 10 to 300 Hz. Different sizes of each of the three dampers were used in order to change the transmissibility curve. Among the selections,

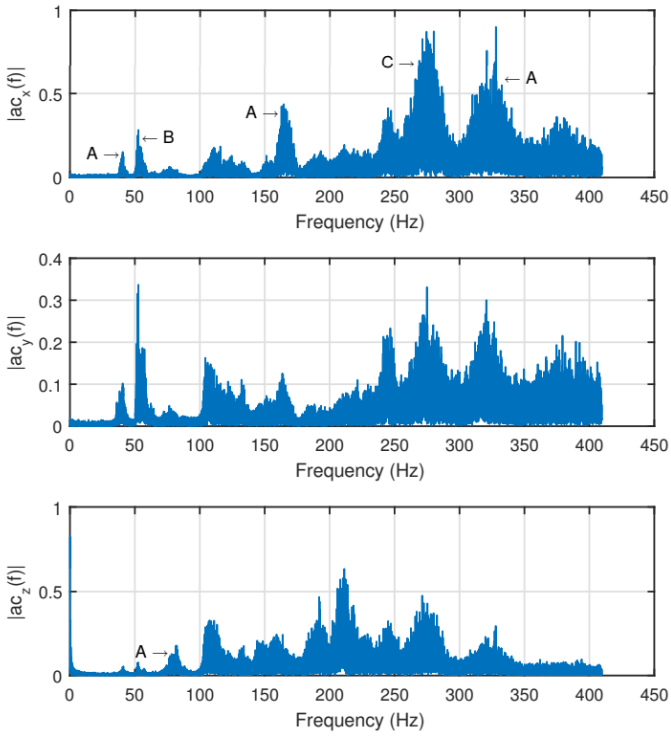

Figure C.7: sUAS vibration measured by an IMU before the damper installation [156].

Kyosho Zeal Sheet had the best performance. Therefore, it was installed on the sUAS to mitigate the vibrations on the additional IMU. The size of the damper was chosen so that the natural frequency of the damper (around 50 Hz) was further apart as possible from the highest disturbing frequencies (around 270 Hz) to be mitigated. Results of the flight experiment (Figure C.8) show a significant reduction on the vibrations. However, as expected from the transmissibility curve of the damper, vibration caused by the rotors at around 50 Hz was slightly amplified.

C.3.2 Other mechanical solutions

In addition to the use of dampers on the optical imaging system, other actions can be taken to reduce vibrations on sUAS. In rotary-wing platforms, an accurate balancing of the propeller blades may reduce the propeller-induced vibrations significantly [100]. Other suggestions are given by [140], focusing on the reduction of noise produced by sUAS, but, as in many cases the noise is related to the vibration of parts of the platform, the same actions can be applied to vibration mitigation. The author categorizes the methods into five groups: conventional noise

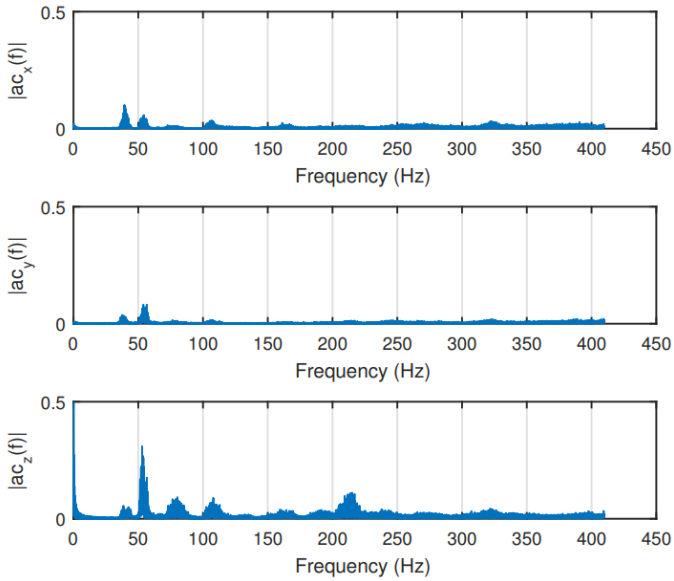

Figure C.8: sUAS vibration measured by an IMU after the damper installation [156].

control methods by modifying the structure; futuristic methods; reduction of engine noise; operation time adjustment based approach; and noise reduction targets of the federal agencies. The first method consists on passive and active techniques. An example of a passive technique is to use vibration-absorbing materials on the structure and therefore reduce the vibration on a specific frequency band. Actives techniques are, e.g., closed loop adaptive feedforward control techniques with electromechanical systems, such as piezoelectric actuators, to reduce the vibration of surfaces [32]. The second category is regarding the design and selection of materials that could reduce the vibration, such as "owl wings". Engine noise mitigation is the third category and the author points out some methods from the literature, such as structural modifications; active noise control systems; slightly changes the phase between the propeller sets; and modifying blades and controlling the rotation speed. All these techniques are to be considered during the design and manufacturing phases and should be taken into account if the purpose of the sUAS being developed is sensitive to vibrations. The last two categories discussed by the author are not related to vibration mitigation.

Flow-induced oscillations

During the design of a optical imaging system it may prove beneficial to consider the effects of flow induced oscillations on the structure. By minimizing the occurrence

of the oscillations, the overall system performance may increase, while the need for mitigation through dampening could be reduced. Here the most relevant aspects with regards to the stabilized imaging system design are discussed. Vortex-induced vibrations (VIV) is a phenomena where the generated vortices cause vibrations of the object. This is caused by the asynchronous periodical release of vortices along the object. The magnitude and impact of VIV is highly dependent on the flow conditions and the shape of the body.

Because the optical imaging sensor is mounted on the airframe, it may experience vibrations that are not necessarily caused by the optical imaging sensor itself, but by the airframe or components that are installed on the airframe. Besides more obvious sources of vibrations, the aircraft may suffer from secondary aerodynamic effects. One prominent example of this is *dutch roll*. This is an oscillatory movement caused by a change in the aircraft's yaw, which is coupled into a roll movement. Because a yaw movement forces one wing forward in relation to the other, a differential in that wing's lift and drag occurs. This causes the aircraft to wiggle. The dynamics behind dutch roll are considered a difficult dynamic mode to analyze [154]. However, if the performance of the optical imaging sensor suffers from the effects of dutch roll, the typical remedies include an increase of the aircraft's vertical tail, or the installation of a yaw dampener [110]. The occurrence of dutch roll can be recognized by an oscillatory motion, where the roll motion lags behind the yaw motion by approximately $\pi/2$.

C.4 Optical Image Stabilization

In imaging missions, an alternative or supplement to mechanical vibration mitigation is Optical Image Stabilization (OIS) [155]. This technique consists of using motion sensors readings to detect vibration and to move the lens or sensor in order to correct the jitter. Nowadays, many camera systems, especially the ones installed on the most modern phones come with this capability. Basically, actuators move the camera system parts according to the detected vibrations, cancelling the effect. OIS is considered superior to digital image stabilization as it acts before the image acquisition and therefore there is no image distortion or degradation. Despite its advantage, not all imaging systems have this feature and the installation of OIS on the existing imaging systems is very challenging as the intervention happens in the hardware of the imaging system. OIS can also alter camera parameters, reducing the accuracy of remote sensing data.

[91] evaluated the performance of an OIS system using fuzzy sliding-mode controller under the effect of sinusoidal signals of 6 Hz, 8 Hz, 10 Hz and 12 Hz. The camera acquired images of a standard ISO-12233 chart with OIS ON and OFF. Figure C.9

shows the comparison between the chart picture taken from a camera with and without OIS turned on for vibrations of ±0.15 degrees on the vertical axis.

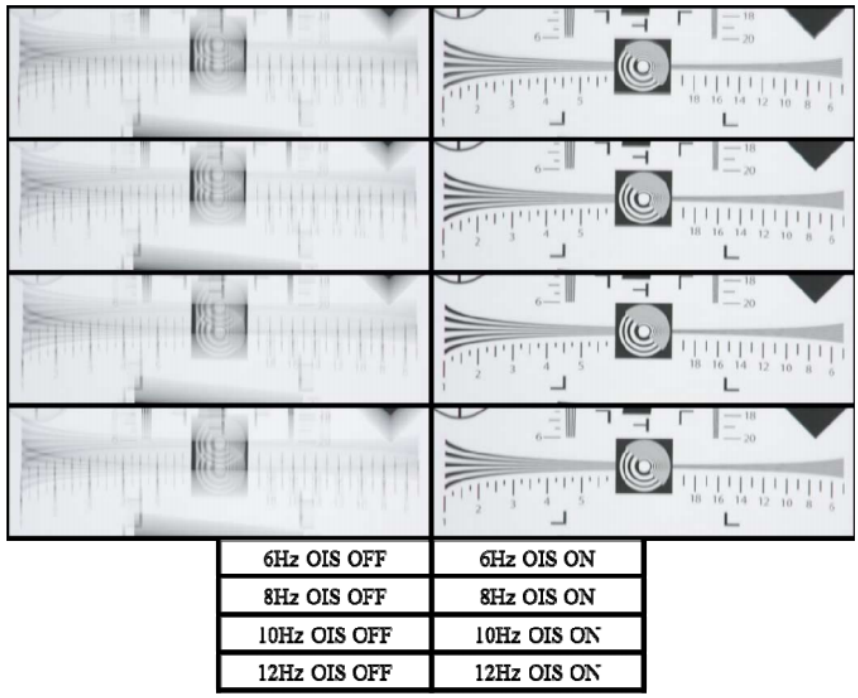

Figure C.9: Comparison of OIS OFF and ON on a standard ISO-12233 chart [91].

C.5 Software Image Stabilization

Image stabilization algorithms are also a way to reduce the effect of vibration on images. This category of image processing is usually referred to as Digital Image Stabilization (DIS). It is important to make a distinction between DIS and digital video stabilization. Digital video stabilization consists of removing the effects of unwanted camera motion from video data; and Digital Image Stabilization (DIS) consists of correcting the effects of unwanted motions that are taking place during the integration time of a single image or video frame [135], by estimating the motion between frames in sequential imaging and then removing unwanted camera motions.

C.5.1 Digital Image Stabilization

In DIS, motion estimation techniques can be classified into two categories: feature based [111] or direct pixels based [78] (also called "image based"). The main differ-

ence is that feature based approaches extract characteristics of the frames such as corners, edges, etc, while direct pixels based approaches use every single pixel on the calculations. Therefore, techniques using the feature based approach are usually faster and more effective but implies non optimal use of the available information. Also, in images where the degradation caused by vibrations is too accentuated, the number of detectable features is small and the features may not be sufficiently reliable, therefore, a direct pixels based approach would be more suitable because it uses the intensity of every single pixel of the image. The motion estimation is usually done by estimating a parameter vector, which is a two-dimensional mapping function that overlaps input images over a reference image [135]. The reference image has to be chosen among a sequence of images and a good candidate to be a reference image may be the one the least affected by blur. To identify such image, a sharpness measure can be used.

Figure C.10 shows an example of a comparison between an image captured with exposure time of 1.8 seconds where DIS was not applied (Figure C.10a) and a resulted DIS image (Figure C.10b) using 4 frames captured with 0.3 seconds of exposure time each. It is possible to notice that the image for which the DIS algorithm was applied is less blurry.

(a) (b)

Figure C.10: (a) non stabilized image taken with exposure time of 1.8 sec; and (b) stabilized image by fusing four frames with exposure time of 0.3 sec each [135].

C.5.2 Digital Video Stabilization

In digital video stabilization, where the goal is to make the video flow less trembled due to the movement of the camera, the motion between frames is also estimated by calculating the rotation and translation between frames. Then, the opposite motion can be applied to counteract image shake and realign the frames in order to make the transition between frames smoother [12]. This is a very popular topic

on sUAS imaging because video taken from sUAS frequently suffers from unwanted motion of the sensors.

In [133], Scale Invariant Feature transform (SIFT) was used for key point detection and matching between successive frames taken by a sUAS. Then, an affine transformation model was used to estimate the global motion parameters between two successive frames. After that, the undesired motions were compensated and spatio-temporal filtering was used to remove the noises in the video. Finally, all frames were transformed to obtain stabilized video frames.

A fast video stabilization for sUAS was proposed by [122]. A polynomial fitting and predicting method was proposed to estimate the global motion parameters and to select undesired frames. After that, the undesired frames are compensated and all frames are transformed to obtain stabilized images. Figure C.11 shows the compensation (Figure C.11d) of an undesired frame (Figure C.11c).

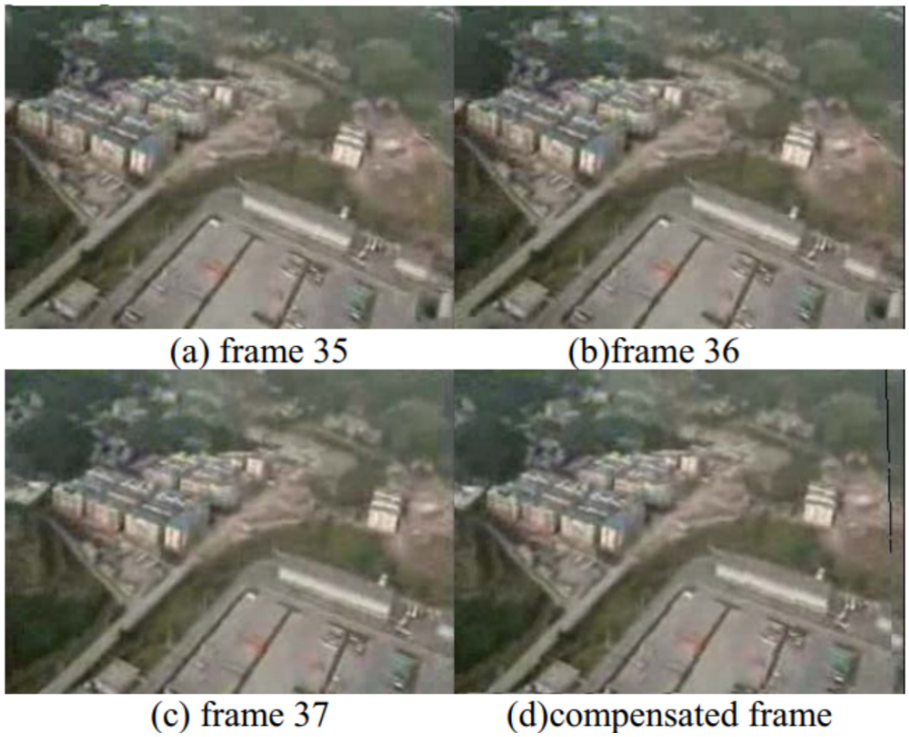

Figure C.11: Compensation of an undesired frame for video stabilization [122].

As most of sUAS are equipped with inertial measurement units (IMU), an alternative to the feature or pixel based motion estimation for digital video stabilization is to use the IMU readings to calculate the camera motion between frames and

use this information to stabilize the camera feed [**?**]. IMU readings can also be integrated with conventional motion estimation methods to increase the speed and accuracy [118]. In this case, the results can be improved significantly as the accuracy of the motion estimation increases. A timing and navigation solution was developed by [2], which made it possible to synchronize the camera images with the UAV's position with high accuracy by using dedicate hardware time synchronization of GNSS, IMU and camera sensors readings.

C.6 Gimbal Stabilization

sUAS gimbal systems are electromechanical devices that can be used to stabilize a platform on a given attitude. Therefore, they are suitable to mitigate unwanted camera rotations caused by the UAS motion and also for pointing the platform on a desired direction, controlling the sensor's line of sight (LoS). Such systems have already been used in many areas before, such as spacecrafts, manned aviation and cinematography. However, due to the recent availability of small UAS and its market growth, there is a new demand for small and precise gimbal systems specifically optimized for particular requirements regarding size and precision. Also, this topic is benefiting from the advances in the miniaturization of key technologies such as high-performance gyros and drivetrain components, fast embedded microcontrollers and small cameras. Therefore, small gimbal system design is a topic just recently being researched, which the main challenges are regarding the limited size and weight of the device. In order to evaluate the different gimbal designs, [99] has undertaken a number of trade studies, investigating various gimbal configurations, sensors, encoders, drivetrain configurations, control system techniques, packaging etc.

C.6.1 Gimbal Systems Classification

[99] classifies the gimbal systems according to stabilization performance related to the LoS Jitter (µrad RMS). Low performance gimbal systems are the ones with more than 250 µrad RMS of LoS Jitter. Medium quality with from 25 to 250 µrad RMS and high quality with less than 25 µrad RMS. [15] classifies the gimbal systems by crossing size and LoS stabilization performance in degrees. Small gimbal systems weight up to 4.5 kg and can achieve a LoS stabilization performance on the order of ±0.5 to ±0.1 degrees. Medium and larger gimbal systems weight from 4.5 to 9.0 kg and greater than 22.5 kg can and can achieve less than ±0.1 degrees of LoS stabilization performance.

C.6.2 Gimbal Systems Design Considerations

Regarding sUAS gimbal systems design, while [99] did a wide comparison between different configurations, in order to provide a broad overview of the design concepts, [15] focused his work on studying the topic to define the best approach for the development of his specific gimbal system, designed to meet size, weight and performance requirements previously defined.

According to [99], the first aspect of gimbal system design is to decide the number of gimbal axes needed for a desired LoS control and field-of-regard (FoR), which is the area over which the gimbal can point. A minimum of two axes are required for controlling two degrees of freedom and point the LoS in a two-dimensions (vertical/tilt/pitch and horizontal/pan/yaw) desired direction. To control a third degree of freedom, such as the image orientation, a third axis is needed. In small sUAS, two-axis gimbal systems are most commonly used. In fixed-wing sUAS, it is common to use gimbal systems with an outer azimuth gimbal axis to control the pan so that it is able to rotate 360 degrees and therefore have a wider FoR.

Another important design aspect is to correctly align the center of gravity with the gimbal motors. By doing this, the required torque and power to make precise angular rotations can be greatly reduced [19].

Thermal considerations must also be addressed because sUAS gimbal systems are commonly too small to package cooling fans or heat exchangers. Therefore, correct electronics layout and proper materials selection are the best measures to mitigate thermal problems.

C.6.3 Stabilization

As the gimbal system will be mounted on a sUAS, which is subject to vibrations caused by rotors, engine or turbulent aerodynamic flows, the gimbal system vibration isolation must be addressed. Combustion engine powered sUAS produce large torque pulses, due to the non-continuous nature of their operation, often in the range of 50-80 Hz. This can cause significant image blurring and/or excitation of jitter in the gimbal's control system, if no specific vibration isolation is provided. Electric powered sUAS produce higher frequencies, which are easier to mitigate and have less of effect on the image quality.

Gimbal system stabilization can be active or passive. Passive stabilization is related to the fact that the platform, sensor, and target LoS move within inertial space. Therefore, low friction joints and high inner axis inertia can passively contribute to maintaining the desired LoS/attitude [15]. Active stabilization is done when the drivers will act based on sensor readings to keep the platform's desired

attitude/LoS. Therefore, to mitigate these vibration effects, [15] designed an active inertial dampening to take care of frequencies of less than 5 Hz and the gimbal system mechanical design provides a good passive inertial dampening for frequencies on the order of 5-20 Hz. For higher frequencies, the gimbal mounting system is responsible for dampening them out. According to [99], an option to mitigate severe effects of sUAS vibration could be to decouple the gimbal system from the sUAS by vibration isolation, isolating its parts from the UAV structure, however, this solution may degrade the accuracy of any type of pointing relative to the vehicle, and can induce angular motion inputs. This degradation occurs due to the necessity of accurate measurements the gimbal position relative to the sUAS in order to send the correct controls to the drive systems.

Regarding the vibration caused by the gimbal system structure itself, fortunately, the frequency of the gimbal system structural resonance is typically higher for smaller gimbals than larger gimbals [99]. Therefore, structural vibration effects are often much less a design issue in small sUAS gimbal system design but nonetheless important to consider. The most common approach to deal with this is to include structural notch filters, which helps to improve the loop gain margin at the resonant frequency. [69] does a deeper analysis of the gimbal structural interactions and suggests to stiffen the structure, as a first attempt to attenuate LoS motion due to bending and to modify the relevant structural transfer functions. The author also suggests to stiffen the torsional response of the mounting structure, to add mass to the stationary gimbal structure, and to employ the notch filters in the pointing servo system to achieve a better interaction of the control system with the structure.

Drive System

The gimbal drive system can be direct, where the motor controls the axis directly, or indirect, via cables, gears or belts. Gimbals with brushless DC direct drive have the highest performance, being able to achieve very low friction and no reflected inertia [99]. However, it is usually heavier, bigger and more expensive than the other approaches to achieve the same torque, and needs more complex electronics. If an indirect drive with gears or belts is chosen, the solution is cheaper and smaller, but has increased backlash, hysteresis, cogging and compliance as result. The cable drive approach has a performance between the direct drive and gears/belts approaches but it has higher friction and lower stiffness, and the difficulty to achieve 360 degrees continuous motion for the yaw axis.

[15] designed the gimbal system using brushless DC servomotors with belts, pulleys and gears for its axes. The first design attempt achieved too high backslash in the pan axis. Therefore, the final decision was to use the motor without a gearbox

driving a small rubber wheel directly on an interior bearing surface.

As part of a fixed-wing sUAS imaging system design, [125] designed and produced a new gimbal system aiming to achieve a better stabilization, wire handling, repairing capability and robustness than the off-the-shelf gimbal systems. As self stabilizing direct drive gimbals using speedy brushless motors became available in the market for multirotors, the authors decided the use this kind of motor on their new gimbal system design specially because they allow gimbals to move fast enough to stabilize the camera from low frequency vibrations. The commercial brushless gimbal systems are often supplied with a dedicated controller which uses input from an IMU to be mounted on the camera. However, according to the authors, angular drift in heading is a potential worry when using a brushless motor for the yaw rotation, specially because of the bias instability of the IMU. A possible solution to remediate this problem could be to implement an estimator between the IMU and the controller board, integrated to the sUAS' heading estimator. Another advantage with using brushless motors and IMU is no need to index the gears when disassembling the gimbal. Therefore, as long as the IMU is reinstalled in the same location and orientation, the gimbal will calibrate itself on startup.

The minimum torque of a motor used to stabilize a given sensor is the sensor's moment of inertia times the desired angular acceleration.

$$T = J\alpha, \tag{C.1}$$

where T is the torque, J is the moment of inertia and α is the angular acceleration.

Therefore, the first steps when choosing the right motor is to calculate the moment of inertia and to choose the desired angular acceleration.

[15] derives the equations detailed by [80] which includes all torque contributions and consequences. In the same axis, the contributions are from the torque of friction and cable restraint and the mass imbalance torque. In case of the inner axis (e.g elevation), where the gimbal is mounted on the sensor body, the mass imbalance torque is caused by the asymmetry of the sensor. In the outer axis (e.g azimuth), where the gimbal is mounted on the inner gimbal mounting that is connected to the sensor body, the mass imbalance torque is caused by the asymmetry of the sensor plus the inner gimbal mounting asymmetry.

In [19], where a gimbal system to house two imaging sensors was designed, the authors also opted to use brushless DC motors to directly drive the gimbal axes because of their superior small angular rotations compared to servos. Low weight motors (109 g per motor) capable to carry the payload (around 400 g) were chosen.

Motion Sensors

Gyros are the main rotational sensors used in gimbal systems. They measure gimbal angular velocities, and are used as system's feedback. Gimbal gyros are usually based on Micro-Electro-Mechanical Systems (MEMS) technology and should have the lowest noise and bias instability that the design constraints allow.

Resolvers and encoders are the most common gimbal angle transducers [99]. They are used to detect the orientation and to report the absolute position of the axes. Resolvers are more robust but incremental encoders are becoming very popular for gimbal angle measurement because they are smaller, lighter and cheaper and can achieve comparable resolution and accuracy. Encoders can be optical, capacitive or magnetic. [15] used a 12 bits of resolution magnetic encoder for each axis of the gimbal system design.

C.7 Impact of the stabilized imaging system on sUAS Aerodynamics

Implementing a stabilized imaging system that is optimized for airborne vehicles requires consideration of its effects on the in-flight performance. Studying the effects early in the design process may enable a reduction in the negative impact on the in-flight performance. Presented in this section are the system design trade-offs in relation to the overall aircraft performance. Besides the energy consumption of the electrical components, the in-flight performance of the aircraft is primarily affected by the system's mass, shape and position. In addition to the flow-induced oscillations, as described in section 2.1.3, these parameters are elaborated to such an extend that it gives the essentials in design considerations in the context to aircraft performance.

C.7.1 Impact of weight

Aerial vehicles stay afloat in the air by generating a force that is equal and opposite to earth's gravitation force. In the case of conventional fixed-wing and rotary-wing aircraft creating such a force requires the consumption of energy. To generate such a thrust force the rotary-wing aircraft utilize one or more powered propellers which are positioned so that it directly counteracts the gravitation force. Fixed-wing aircraft utilize one or more propellers to generate a forward motion, which results in the main wings to generate a lift force that opposes the gravitational force. As the total mass of the aircraft increases, so does the required lift force. This results in an increase in energy consumption.

In an attempt to demonstrate the importance of weight reduction, the effects of

weight on the energy consumption of the aircraft are quantified. For both fixed-wing and rotary-wing sUAS, the maximum range by approximation is reduced proportional to the increase in weight. For sUAS with constant mission variables, the maximum endurance is reduced by a factor of approximately $W^{3/2}$, where W is the weight, for both fixed-wing [110] [72] and rotary-wing [88]. Therefore, an increase of 5% on weight, for example, means a reduction of approximately 7% of endurance.

C.7.2 Impact of shape and size

Moving objects placed inside a viscous medium, such as air, are bound to create external forces. Overcoming the effects of such forces typically increases the in-flight power requirements. A stabilized imaging system that is placed inside moving air will contribute to the total drag force and will thus typically reduce the overall in-flight efficiency. It is therefore warranted to optimize the design of the system to reduce the impact through aerodynamic considerations.

Impact of shape and size on fixed-wing aircraft

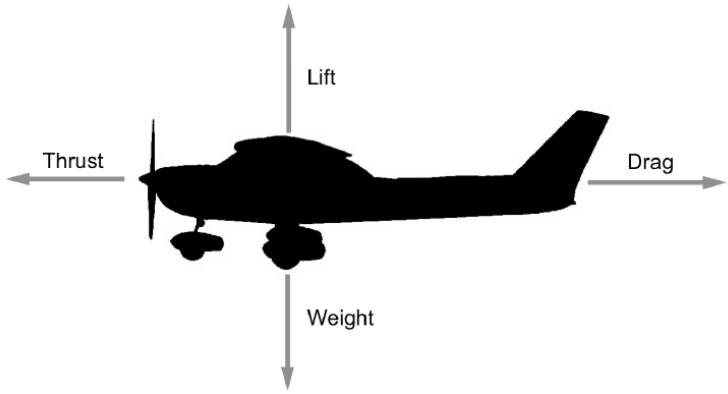

Figure C.12: Aerodynamic forces acting on an airplane - Thrust, Lift and Drag.

Aerodynamic drag, also known as air resistance, is the force parallel to the airspeed [52] (Figure C.12). With an increase in drag, the aircraft needs to compensate the energy losses by producing more thrust in order not to lose speed or altitude. Considering that a typical stabilized imaging system is not intended to generate a lift force, it may be assumed that the in-flight performance benefits from minimizing the total aerodynamic drag generated by system. To be able to reduce the aerodynamic drag it is important to understand how it is built up and how it is affected. The total drag force D generated by an object can be determined through:

$$D = C_D \frac{1}{2} \rho v_a^2 A, \tag{C.2}$$

where

$$C_D = C_{DP} + C_{DI}, \tag{C.3}$$

where ρ is the air density in kilogram per cubic meter, v_a is the speed of the moving air before being affected by the object in meters per second, A is the cross-sectional area of the object in square meters, and finally C_D is a dimensionless drag coefficient that relates the object's shape, inclination and flow conditions to the resulting drag force.

The takeaways from Eq. (C.2) in the context of stabilized imaging systems design are that the drag generally can be reduced by minimizing the size of the object, and that the drag increases exponentially with airspeed. Thus, fast flying aircraft suffer much more from poor design choices than slow flying aircraft. Finally, the drag coefficient C_D ought to be minimized. This can be done by optimizing the shape or placement of the object in such a way that it causes the least interference with the moving air. It should be noted that the complete theoretical basis of aerodynamic flow optimization falls beyond the scope of the study presented here, and is therefore limited to the most relevant aspects. Assuming that the casing of the camera system is not designed to generate lift, the lift-induced drag (C_{DI}) is negligible. The remaining parasitic drag (C_{DP}) can be categorized into:

1. *Form drag:* The form drag is influenced by the shape of the object (Figure C.13). Although the droplet shape offers the most favourable aerodynamic characteristics, when pointed straight into the direction of the moving air, it also offers challenges related to possible viewing angles of the camera system. Therefore, the aerodynamic considerations may be considered a performance parameter within the overall geometrical optimization of the camera system.
2. *Skin friction drag:* As air moves over the surface of the body, close to the surface the flow will lose energy due to viscous effects. This type of drag is called skin friction drag. A turbulent boundary layer that is induced by a rougher surface may stay attached longer than a laminar boundary layer, thus reducing the form drag. This generally holds true for smaller object in relatively low air speeds [110]. Therefore, for smaller objects the negative effects of higher skin friction drag, which is caused by a rougher surface, may potentially be offset by a lower overall profile drag. Finally, it should be noted that such potential benefits are highly dependent on the specific design

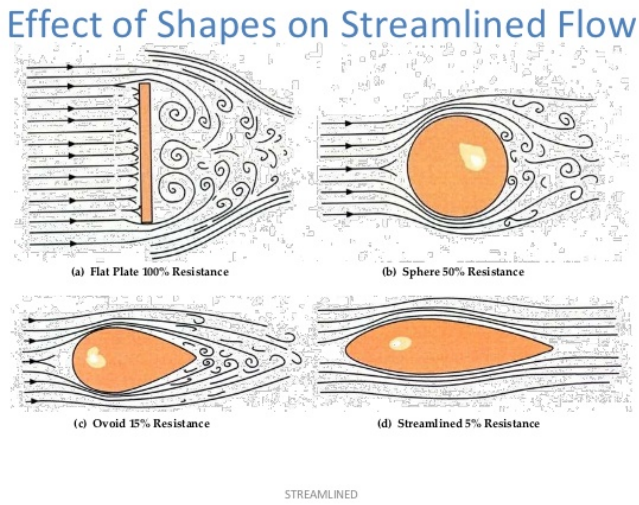

Figure C.13: Flow visualization over different shapes (EASA).

and flow conditions, and therefore require an in-depth aerodynamic analysis. Projects where such analyses is not within reach, may benefit from focusing on the form drag and interference drag instead.

3. *Interference drag:* In the context of aerodynamics, the interference drag can be explained as the airflow over one object disturbing the airflow over another object unfavourably. The actual effects of interference drag depend to large extend on the airspeed. Therefore in the context of aircraft performance it cannot be said that a closed and shielded system is necessarily superior to a system with exposed components as it may also be heavier. It is dependent on mission-specific parameters. The following section suggests methods to study the effects of on-board camera designs, including the interference drag characteristics.

To quantify the actual impact of a camera design on the aircraft performance, there are three methods that ought to be considered. The first is through wind tunnel testing. Inside a wind tunnel the effects of moving air over an object are recreated, and the generated forces and moments are captured. The camera can be placed inside the wind tunnel without the airframe. However, in that case the aerodynamic interactions between the aircraft body and stabilized imaging system are not included. If executed and post-processed correctly, a wind tunnel test can give an accurate indications of the impact of the camera system on the flight performance. Also the airflow around the bodies can be visualized, which provides information

for further optimizing the airflow. However, modelling through wind tunnel experiments are complex and require dedicated equipment. This causes wind tunnel experiments to be relatively expensive and time consuming. Also the iterative design process is commonly slow when compared to its alternatives.

Nowadays, designers have embraced *Computational Fluid Dynamics* (CFD). This is a computer-based method that can approximate the behaviour of fluids, such as air, over an object. It may prove useful for design optimization as it allows for quicker iterative development. In popular terms it is sometimes called a *virtual* wind tunnel. It is to be noted that setting up such a simulation environment requires in-depth knowledge on the theory of fluid dynamics. Also, when results with a high accuracy are required, then a verification of the model is necessary. This is commonly done inside a wind tunnel. This is especially true for low velocities and/or smaller objects, such as camera systems, as the modelling of drag then becomes increasingly problematic.

The final method discussed here is through actual flight tests where the performance is compared with and without the camera system installed. Measuring the consumed energy in cruise flight may serve as an indicative measurement for the impact on the in-flight performance of the aircraft. Such in-flight comparisons are only valid when all mission parameters, including airspeed, altitude, atmospheric conditions and battery charge, are the same in each benchmark flights. Since this may be hard to accomplish and verify, it is important to note that the obtained results are non-conclusive, and can only serve as an approximation. The advantage of this method is that it is accessible and does not require in-depth knowledge of fluid dynamics. This may serve as a suitable method when an approximation is sufficient.

Impact of shape and size on rotary-wing aircraft

For rotary aircraft operating in *stationary* flight there is no forward motion of the vehicle. As the air in front of the rotor is accelerated by the rotors itself, the before mentioned aerodynamic effects require additional design considerations. By locating the camera system outside of the propeller slipstream (v_s), the impact of the aerodynamic effects are limited (Figure C.14). When the aerodynamic effects as a result become small, such a system may not require further aerodynamic optimization. Note, however, that when operating in atmospheric winds the aerodynamic effects remain. For rotary-wing aircraft, a center position ought to be considered. For conventional rotary aircraft, which typically utilize one main rotor, the camera mounting points are commonly found under the main body. As the aircraft's main body shields the camera system to a large extend from the propeller slipstream, the need for aerodynamic optimization decreases. However, due to other design con-

siderations, such as clearance to the ground, these mounting locations may not be feasible. For conventional rotary-wing aircraft the camera systems are often found to be mechanically suspended in front or along the side of the aircraft body. In such cases the aircraft performance benefits from a minimized wetted area, which is the area exposed to the airflow, in order to reduce the interference drag and propeller blockage.

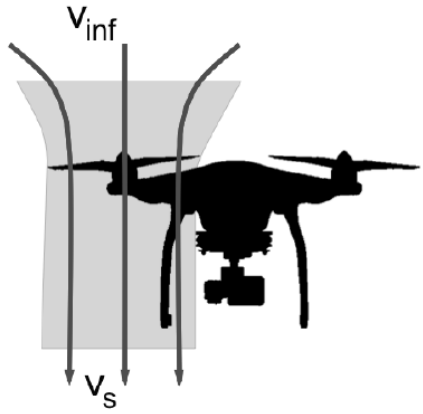

Figure C.14: Visualization of the propeller induced slipstream vs in relation to the camera location (in red).

C.7.3 Impact of Position

For fixed-wing and rotary-wing aircraft to be controllable in flight, it relies on the ability of the aircraft to compensate the generated forces which are experienced. Each individual component installed on an aircraft has a mass. When these components are exposed to the moving air it will create a drag force, while lifting bodies may also generate a lift force. First, for the aircraft to maintain altitude in the air, the aircraft needs to be able to generate enough lift force (or thrust) to compensate the aircraft's total weight. In other words, for level flight the sum of the vertical forces equals zero. In addition, all these individual forces, such as lift and drag will generate a moment around the aircraft's center of gravity (C.G.).

C.8 Conclusions

Vibration is one of the main concerns when designing sUAS optical imaging systems. In fixed-wing platforms equipped with a combustion engine, the engine is the main source of vibration, followed by the turbulent aerodynamic flow. Rotary-wing platforms have the rotors as the main source of vibration. To mitigate the effects of vibration, mechanical solutions such as dampers can be used. Also, it is possible to

use optical stabilization by installing motion sensors to measure the jitter and use actuators to move the lens in order to correct it. Software solutions are also available, such as digital image stabilization or digital video stabilization algorithms. Gimbal stabilization platforms can be used for stabilization and also for pointing. The most important components in these platforms are the drive systems and the motion sensors. The installation of a stabilization platform may affect the sUAS aerodynamics and the impact of weight, shape, size and position must be taken into consideration in the design phase.

Appendix D

Particle Swarm Optimization

Particle Swarm Optimization (PSO) [34] is a technique that uses a population of solutions that explores the hyperspace of a problem at a defined speed, which is adjusted according to the best individual historical solution p_{best}, and with the best historical global solution g_{best}. This evaluation is performed by calculating the cost function. Calculating the cost function according to the position of the particle makes it possible to identify whether the new position is better than that previously occupied by the particle. Thus, at each iteration a new velocity, i.e., the movement in the domain space, is adjusted as a function of p_{best} and g_{best}. This is done so that each particle explores the hyperspace optimally, as it takes into consideration the historical performance of the population. This procedure is illustrated in figure D.1. Through this method the movement of each particle is considered to naturally evolve into the optimal (solution) position.

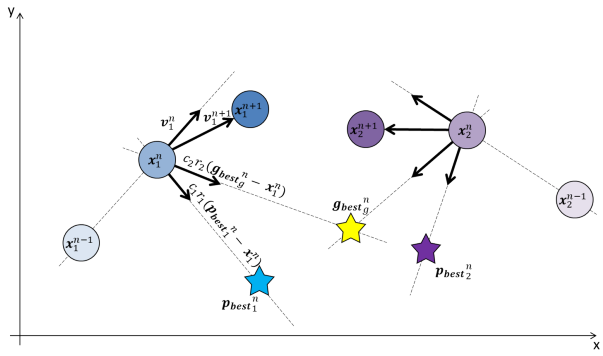

Figure D.1: Behavior of two particles in an arbitrary two-dimensional space

This technique is notable for its simplicity as the behavior of each particle, and therefore the set of presumed solutions, is defined by only two iterative equations.

These determine the position x_i^n and velocity v_i^n of the particle i at time n, resulting in:

$$\begin{aligned} v_i^{(n+1)} = v_i^n + \ & c_1 \ r_1({p_{best_i}}^n - x_i^n) \\ + \ & c_2 \ r_2({g_{best_g}}^n - x_i^n) \end{aligned} \tag{D.1}$$

$$x_i^{(n+1)} = x_i^n + v_i^{(n+1)} \tag{D.2}$$

where c_1 and c_2 are called "acceleration coefficients", which are related to the local and global portion, respectively; and with r_1 and r_2 representing the stochastic factor of these accelerations. These are usually chosen as a uniformly distributed random value between 0 and 1.

The PSO algorithm corresponds to the pseudocode shown in Algorithm 1:

Algorithm 1 PSO

```
Initialize a swarm with random positions and velocities
while Stop criteria is not satisfied do
    for Each particle i do
        Calculate the new velocity
        Update the position
        Evaluate the cost function f(x_i)
        if f(x_i) < f(p_best_i) then
            p_best_i ← x_i
        end if
        if f(x_i) < f(g_best_g) then
            g_best_g ← x_i
        end if
    end for
end while
```

Several authors proposed modifications to the basic algorithm. In this study two small modifications proposed by the original creators of the algorithm are adopted; position and velocity boundary constraints as described in [36], and linear inertia weight as described in [35].

The PSO algorithm evolves by updating the particle position for each iteration in relation to the velocity vector. Such updates have stochastic gains, where it is undesirable that the particles move uncontrollably. A particle that has a high velocity in relation to the total domain size, may eventually jump to a distant point inside the domain. This results in the particle no longer performing a minutely

search for the optimum. To avoid this problem, the concept of position and velocity constraints was developed.

Another fundamental strategy is to limit the search domain in relation to the optimization problem in question. To prevent the particle from exploring distant regions away from the region that has the optimal solution, or to prevent from bringing solutions outside the problem domain.

Here the basic idea is to avoid for the particle to leave the domain where the optimal solution resides.

The constraints can be implemented through:

$$v_i = \begin{cases} V_{max} & \text{if } v_i > V_{max} \\ -V_{max} & \text{if } v_i < -V_{max} \\ v_i & \text{otherwise} \end{cases} \tag{D.3}$$

The following conditions are added to the algorithm:

$$x_i = \begin{cases} X_{max} & \text{if } x_i > X_{max} \\ X_{min} & \text{if } x_i < X_{min} \\ x_i & \text{otherwise} \end{cases} \tag{D.4}$$

The final modification is to permit a better control of the search domain. The inertia weight, indicated in the following equation as w^n, is applied to the current velocity v_i^n, during the process of calculating the new velocity of the particle:

$$\begin{aligned} v_i^{(n+1)} = w^n v_i^n + c_1\, r_1 ({p_{best_i}}^n - x_i^n) \\ + c_2\, r_2 ({g_{best_g}}^n - x_i^n) \end{aligned} \tag{D.5}$$

When a constant value is chosen for the inertia weight, high values imply high velocities, which can make the particle to traverse the entire search domain more quickly; while low values slow down, limiting the search domain of the particle to its neighborhood. Initially, a constant value was proposed for the inertia weight. However, proposals of dynamic values that varied linearly appeared later.

In this specific case the consensus is that initially it is more convenient for the particle to have a global search power, and only afterwards perform a more local exploration. In the linear inertia weight, if N is the maximum number of iterations,

nd w_{ini} and w_{fin} are the values of the initial and final inertia weight, the inertia weight for the iteration n is determined by:

$$w^n = (w_{ini} - w_{fin})\frac{(N-n)}{N} + w_{fin} \tag{D.6}$$

References

[1] W. H. Al-Sabban, L. F. Gonzalez, and R. N. Smith. Wind-energy based path planning for unmanned aerial vehicles using markov decision processes. In *Robotics and Automation (ICRA), 2013 IEEE International Conference on*, pages 784–789. IEEE, 2013.

[2] S. Albrektsen and T. Johansen. User-configurable timing and navigation for uavs. *Sensors*, 18(8):2468, 2018.

[3] J. Anderson. *Aircraft performance and design*. McGraw-Hill international editions: Aerospace science/technology series. WCB/McGraw-Hill, 1999. ISBN 9780070019713.

[4] J. Anderson. *Introduction to Flight*. Anderson series - International edition. McGraw-Hill, 2012. ISBN 9780071086059.

[5] F. A. A. Andrade, A. R. Hovenburg, L. N. Lima, C. D. Rodin, T. A. Johansen, R. Storvold, C. A. B. Correia, and D. B. Haddad. Autonomous unmanned aerial vehicles in search and rescue missions using real-time cooperative model predictive control. Submitted for publication.

[6] ANSYS. Ansys fensap-ice user manual 18.2, 2017.

[7] G. Avanzini and F. Giulietti. Maximum Range for Battery-Powered Aircraft. *Journal of Aircraft*, 50(1):304–307, 2013. doi: 10.2514/1.C031748.

[8] R. W. Beard and T. W. McLain. *Small unmanned aircraft: Theory and practice*. Princeton university press, 2012.

[9] R. Bencatel, M. Faied, J. Sousa, and A. R. Girard. Formation control with collision avoidance. In *2011 50th IEEE Conference on Decision and Control and European Control Conference*, pages 591–596. IEEE, 2011.

[10] S. Benders, A. W. Wenz, and T. A. Johansen. Adaptive path planning for unmanned aircraft using in-flight wind estimation. In *2018 International Conference on Unmanned Aerial Systems*, 2018.

[11] J. Berndt. JSBSim: An open source flight dynamics model in c++. In *AIAA Modeling and Simulation Technologies Conference and Exhibit*, page 4923, 2004.

[12] A. Bosco, A. Bruna, S. Battiato, G. Bella, and G. Puglisi. Digital video stabilization through curve warping techniques. *Consumer Electronics, IEEE Transactions on*, 54:220 – 224, 06 2008. doi: 10.1109/TCE.2008.4560078.

[13] J. Braga, R. Praveen Jain, A. Pedro Aguiar, and J. Sousa. Self-triggered time coordinated deployment strategy for multiple relay UAVs to work as a point-to-point communication bridge. In *Research, Education and Development of Unmanned Aerial Systems (RED-UAS), 2017 Workshop on*, pages 0–0. IEEE, 2017.

[14] M. B. Bragg, A. P. Broeren, and L. A. Blumenthal. Iced-airfoil aerodynamics. *Progress in Aerospace Sciences*, 41(5):323–362, 2005.

[15] N. J. Brake. Control system development for small uav gimbal. Master's thesis, California Polytechnic State University, San Luis Obispo, 08 2012.

[16] Ø. Breivik, A. A. Allen, C. Maisondieu, and J. C. Roth. Wind-induced drift of objects at sea: The leeway field method. *Applied Ocean Research*, 33(2): 100–109, 2011.

[17] E. F. Camacho and C. B. Alba. *Model predictive control*. Springer Science & Business Media, 2013.

[18] E. F. Camacho, D. R. Ramírez, D. Limón, D. M. De La Peña, and T. Alamo. Model predictive control techniques for hybrid systems. *Annual reviews in control*, 34(1):21–31, 2010.

[19] Z. D. Caratao, K. F. Gabel, A. Arun, B. Myers, D. L. Swartzendruber, and C. W. Lum. Micasense aerial pointing and stabilization system: Dampening in-flight vibrations for improved agricultural imaging. In *2018 AIAA Information Systems-AIAA Infotech@ Aerospace*, page 1239. 2018.

[20] A. Chakravarty. Four-dimensional fuel-optimal guidance in the presence of winds. *Journal of Guidance*, 8:16–22, 1985. doi: 10.2514/3.19929.

[21] P. Chandler, S. Rasmussen, and M. Pachter. UAV cooperative path planning. In *AIAA Guidance, Navigation, and Control Conference and Exhibit*, pages 1255–1265, 2000.

[22] M. Coombes, W.-H. Chen, and P. Render. Reachability analysis of landing sites for forced landing of a UAS inWind using trochoidal turn paths

matthew. In *2015 International Conference on Unmanned Aerial Systems (ICUAS)*. ICUAS 2017, June 2015.

[23] M. Coombes, W.-H. Chen, and P. Render. Landing site reachability in a forced landing of unmanned aircraft in wind. *Journal of Aircraft*, 54:1415–1427, 2017. doi: 10.2514/1.C033856.

[24] F. A. de Alcantara Andrade, C. D. Rodin, A. R. Hovenburg, T. A. Johansen, and R. Storvold. Path planning of multi-UAS communication relay by decentralized MPC. In *2018 OCEANS-MTS/IEEE Kobe Techno-Oceans (OTO)*, pages 1–8. IEEE, 2018.

[25] D.Greatrix. *Powered Flight*. Springer, 2012. ISBN 978-1-4471-2484-9.

[26] B. Di, R. Zhou, and H. Duan. Potential field based receding horizon motion planning for centrality-aware multiple UAV cooperative surveillance. *Aerospace Science and Technology*, 46:386–397, 2015.

[27] C. Dixon and E. W. Frew. Maintaining optimal communication chains in robotic sensor networks using mobility control. *Mobile Networks and Applications*, 14(3):281–291, 2009.

[28] U. DoD. Department of defense dictionary of military and associated terms. *Joint Publication*, pages 1–02, 2007.

[29] D. Doerffel and S. Sharkh. A critical review of using the Peukert equation for determining the remaining capacity of lead-acid and lithium-ion batteries. *Journal of Power Sources*, 155:395–400, 2006. ISSN 03787753. doi: 10.1016/j.jpowsour.2005.04.030.

[30] T. Donateo and A. Ficarella. Designing a hybrid electric powertrain for an unmanned aircraft with a commercial optimization software. In *SAE International Journal of Aerospace*, volume 10, 2017.

[31] T. Donateo, A. Ficarella, L. Spedicato, A. Arista, and M. Ferraro. A new approach to calculating endurance in electric flight and comparing fuel cells and batteries. *Applied Energy*, 187:807–819, 2017. ISSN 03062619. doi: 10.1016/j.apenergy.2016.11.100. URL http://dx.doi.org/10.1016/j.apenergy.2016.11.100.

[32] M. J. Doty, C. R. Fuller, N. H. Schiller, and T. L. Turner. Active noise control of radiated noise from jets. *NASA, Langley Research Center, Hampton, Virginia, USA*, 2013.

[33] M. Drela and H. Youngren. AVL 3.36 user primer. web.mit.edu/drela/Public/web/avl/avl_doc.txt, 2017.

[34] R. Eberhart and J. Kennedy. A new optimizer using particle swarm theory. In *Micro Machine and Human Science, 1995. MHS'95., Proceedings of the Sixth International Symposium on*, pages 39–43. IEEE, 1995.

[35] R. C. Eberhart and Y. Shi. Comparing inertia weights and constriction factors in particle swarm optimization. In *Evolutionary Computation, 2000. Proceedings of the 2000 Congress on*, volume 1, pages 84–88. IEEE, 2000.

[36] R. C. Eberhart, Y. Shi, and J. Kennedy. *Swarm intelligence*. Elsevier, 2001.

[37] B. Eggleston, B. McLuckie, W. R. Koski, D. Bird, C. Patterson, D. Bohdanov, H. Liu, T. Mathews, and G. Gamage. Development of the brican td100 small uas and payload trials. *ISPRS - International Archives of the Photogrammetry, Remote Sensing and Spatial Information Sciences*, XL-1/W4:143–149, 2015.

[38] FAA. 14 cfr parts 25 and 29, appendix c, icing design envelopes, 2002. DOT/FAA/AR-00/30.

[39] A. Filippone. *Flight Performance of Fixed and Rotary Wing Aircraft*. Butterworth-Heinemann, 2006. ISBN 978-0-7506-6817-0.

[40] E. J. Forsmo, E. I. Grøtli, T. I. Fossen, and T. A. Johansen. Optimal search mission with unmanned aerial vehicles using mixed integer linear programming. In *2013 International conference on unmanned aircraft systems (ICUAS)*, pages 253–259. IEEE, 2013.

[41] A. Franco, D. Rivas, and A. Valenzuela. Optimization of unpowered descents of commercial aircraft in altitude-dependent winds. *Journal of Aircraft*, 49 (5):1460–1470, 2012. ISSN 0021-8669. doi: 10.2514/1.C031737.

[42] A. Franco, D. Rivas, and A. Valenzuela. Optimal aircraft path planning considering wind uncertainty. *European Conference for aeronautics and Space Sciences (EUCASS)*, 2017. doi: 10.13009/EUCASS2017-254.

[43] E. W. Frew and T. X. Brown. Networking issues for small unmanned aircraft systems. *Journal of Intelligent and Robotic Systems*, 54(1-3):21–37, 2009.

[44] B. Fuller and E. Mark. Generic battery rate-effect model. Technical report, NAVAL UNDERSEA WARFARE CENTER DIV NEWPORT RI AUTONOMOUS AND DEFENSIVE . . . , 2012.

[45] Y. Gabriely and E. Rimon. Spanning-tree based coverage of continuous areas by a mobile robot. *Annals of mathematics and artificial intelligence*, 31(1-4): 77–98, 2001.

[46] A. E. Gill. *Atmosphere—ocean dynamics*. Elsevier, 2016.

[47] B. Girardet, L. Lapasset, D. Delahaye, and C. Rabut. Wind-optimal path planning: Application to aircraft trajectories. *13th International Conference on Control Automation Robotics and Vision, ICARCV 2014*, pages 1403–1408, 2014. doi: 10.1109/ICARCV.2014.7064521.

[48] R. Glassock, J. Y. Hung, L. F. Gonzalez, and R. A. Walker. Design, modelling and measurement of hybrid powerplant for unmanned aerial systems (uas). In *5th Australasian Congress on Applied Mechanics, ACAM 2007*, 2007.

[49] Z. Goraj. An overview of the deicing and anti-icing technologies with prospects for the future. In *24th international congress of the aeronautical sciences*, volume 29, 2004.

[50] A. Grancharova, E. I. Grøtli, D.-T. Ho, and T. A. Johansen. UAVs trajectory planning by distributed MPC under radio communication path loss constraints. *Journal of Intelligent & Robotic Systems*, 79(1):115, 2015.

[51] K. Gryte, R. Hann, M. Alam, J. Roháč, T. A. Johansen, and T. I. Fossen. Aerodynamic modeling of the skywalker x8 fixed-wing unmanned aerial vehicle. In *2018 International Conference on Unmanned Aircraft Systems (ICUAS)*, pages 826–835. IEEE, 2018.

[52] S. Gudmundsson. *General Aviation Aircraft Design: Applied Methods and Procedures*. Elsevier Science, 2014. ISBN 9780123973290.

[53] S. Gudmundsson. *A Biomimetic, Energy-Harvesting, Obstacle-Avoiding, Path-Planning Algorithm for UAVs*. PhD thesis, Embry-Riddle Aeronautical University, 2016.

[54] S. Gudmundsson, V. Golubev, S. Drakunov, and C. Reinholtz. Biomimetic opportunistic approaches in energy-conserving/harvesting flight-path modeling for UAS. *AIAA Modeling and Simulation Technologies Conference*, 2016. doi: 10.2514/6.2016-3676.

[55] J. Gundlach. *Designing Unmanned Aircraft Systems: A Comprehensive Approach*. AIAA education series. American Institute of Aeronautics and Astronautics, 2014. ISBN 9781624102615.

[56] A. Gurtner, R. Walker, and W. Boles. Vibration compensation for fisheye lenses in uav applications. In *Digital Image Computing Techniques and Applications, 9th Biennial Conference of the Australian Pattern Recognition Society on*, pages 218–225. IEEE, 2007.

[57] A. Gurtner, D. G. Greer, R. Glassock, L. Mejias, R. A. Walker, and W. W. Boles. Investigation of fish-eye lenses for small-uav aerial photography. *IEEE Transactions on Geoscience and Remote Sensing*, 47(3):709–721, 2009.

[58] W. G. Habashi, F. Morency, and H. Beaugendre. Fensap-ice: a comprehensive 3d simulation tool for in-flight icing. In *7th International Congress of Fluid Dynamics and Propulsion, Sharm-El-Sheikh, Egypt, December*, pages 1–7, 2001.

[59] W. G. Habashi, M. Aubé, G. Baruzzi, F. Morency, P. Tran, and J. C. Narramore. Fensap-ice: a fully-3d in-flight icing simulation system for aircraft, rotorcraft and uavs. In *24th International Congress of The Aeronautical Sciences*, pages 2004–7, 2004.

[60] J. Haghshenas. Effects of satellite platform's vibrations on the image quality of a remote sensing payload: system level design and challenges. In *Optical Systems Design 2015: Optical Design and Engineering VI*, volume 9626, page 96262P. International Society for Optics and Photonics, 2015.

[61] F. J. Hale and A. R. Steiger. Effects of wind on aircraft cruise performance. In *1978 AIAA Aircraft Systems and Technology Conference*. American Institute of Aeronautics and Astronautics, Aug. 1978.

[62] M. Hals and M. Skjønhaug. Optimization of coordinated path planning for autonomous vehicles in ice management. Master's thesis, NTNU, 2017.

[63] R. Hann. Uav icing: Comparison of lewice and fensap-ice for ice accretion and performance degradation. In *2018 Atmospheric and Space Environments Conference*, page 2861, 2018.

[64] R. Hann. Uav icing: Comparison of lewice and fensap-ice for anti-icing loads. In *AIAA Scitech 2019 Forum*, page 1286, 2019.

[65] R. Hann. Uav icing: Ice accretion experiments and validation. In *SAE Technical Paper*, 2019.

[66] R. Hann, K. Borup, A. Zolich, K. Sorensen, H. Vestad, M. Steinert, and T. Johansen. Experimental investigations of an icing protection system for uavs. Technical report, SAE Technical Paper, 2019.

[67] A. Hausmann and C. Depcik. Expanding the Peukert equation for battery capacity modeling through inclusion of a temperature dependency. *Journal of Power Sources*, 235:148–158, 2013. ISSN 03787753. doi: 10.1016/j.jpowsour.2013.01.174.

[68] Z. He and L. Zhao. The comparison of four UAV path planning algorithms based on geometry search algorithm. In *2017 9th International Conference on Intelligent Human-Machine Systems and Cybernetics (IHMSC)*, volume 2, pages 33–36. IEEE, 2017.

[69] J. Hilkert. Inertially stabilized platform technology concepts and principles. *IEEE Control Systems Magazine*, 28(1):26–46, feb 2008.

[70] A. R. Hovenburg, F. A. A. Andrade, R. Hann, C. D. Rodin, T. A. Johansen, and R. Storvold. Long range path planning using an aircraft performance model for battery powered sUAS equipped with icing protection system. Submitted for publication.

[71] A. R. Hovenburg, F. A. de Alcantara Andrade, C. D. Rodin, T. A. Johansen, and R. Storvold. Contingency path planning for hybrid-electric UAS. In *2017 Workshop on Research, Education and Development of Unmanned Aerial Systems (RED-UAS)*, pages 37–42. IEEE, 2017.

[72] A. R. Hovenburg, T. A. Johansen, and R. Storvold. Mission performance trade-offs of battery-powered sUAS. In *2017 International Conference on Unmanned Aerial Systems (ICUAS)*. ICUAS 2017, June 2017.

[73] A. R. Hovenburg, F. A. de Alcantara Andrade, C. D. Rodin, T. A. Johansen, and R. Storvold. Inclusion of horizontal wind maps in path planning optimization of UAS. In *2018 International Conference on Unmanned Aircraft Systems (ICUAS)*, pages 513–520. IEEE, 2018.

[74] I. IAMSAR. International aeronautical and maritime search and rescue manual. *Mission coordination*, 2, 2007.

[75] W. International. 3W-28i HFE FI test data. http://3w-international.com/Drone_Engines_Sale/engine-details-test-data/engine-data-3W-28i-HFE-FI.php, 2016.

[76] M. Jakob, E. Semsch, D. Pavlicek, and M. Pechoucek. Occlusion-aware multi-uav surveillance of multiple urban areas. In *6th Workshop on Agents in Traffic and Transportation (ATT 2010)*, pages 59–66. Citeseer, 2010.

[77] A. L. Jennings, R. Ordonez, and N. Ceccarelli. An ant colony optimization using training data applied to UAV way point path planning in wind. In *Swarm Intelligence Symposium, 2008. SIS 2008. IEEE*, pages 1–8. IEEE, 2008.

[78] D. Johansen, J. Hall, R. Beard, and C. Taylor. Stabilization of video from miniature air vehicles. In *AIAA Guidance, Navigation and Control Conference and Exhibit*, page 6862, 2007.

[79] T. A. Johansen, A. Zolich, T. Hansen, and A. J. Sørensen. Unmanned aerial vehicle as communication relay for autonomous underwater vehicle—field tests. In *Globecom Workshops (GC Wkshps), 2014*, pages 1469–1474. IEEE, 2014.

[80] P. J. Kennedy and R. L. Kennedy. Direct versus indirect line of sight (los) stabilization. *IEEE Transactions on control systems technology*, 11(1):3–15, 2003.

[81] S. Kim, P. Silson, A. Tsourdos, and M. Shanmugavel. Dubins path planning of multiple unmanned airborne vehicles for communication relay. *Proceedings of the Institution of Mechanical Engineers, Part G: Journal of Aerospace Engineering*, 225(1):12–25, 2011.

[82] S. Kim, H. Oh, J. Suk, and A. Tsourdos. Coordinated trajectory planning for efficient communication relay using multiple UAVs. *Control Engineering Practice*, 29:42–49, 2014.

[83] *Maritime Broadband Radio - MBR*. Kongsberg, (accessed March 23, 2018). URL https://www.km.kongsberg.com/ks/web/nokbg0240.nsf/AllWeb/BCCBAC3EA4EA6785C1257E280039BD63.

[84] J. D. Kraus and R. J. Marhefka. Antennas for all applications. *Antennas for all applications, by Kraus, John Daniel; Marhefka, Ronald J. New York: McGraw-Hill, c2002.*, 2002.

[85] J. W. Langelaan, N. Alley, and J. Neidhoefer. Wind field estimation for small unmanned aerial vehicles. *Journal of Guidance, Control, and Dynamics*, 34 (4):1016–1030, 2011. doi: 10.2514/1.52532.

[86] H.-W. Lee. *Advanced Control for Power Density Maximization of The Brushless Dc Generator*. PhD thesis, Texas A&M University, 2003.

[87] F. S. Leira, T. A. Johansen, and T. I. Fossen. Automatic detection, classification and tracking of objects in the ocean surface from UAVs using a thermal camera. In *2015 IEEE aerospace conference*, pages 1–10. IEEE, 2015.

[88] G. J. Leishman. *Principles of helicopter aerodynamics*. Cambridge university press, 2006.

[89] C. Li and F. Tan. Effect of uav vibration on imaging quality of binary optical elements. In *2018 IEEE International Conference on Mechatronics and Automation (ICMA)*, pages 1693–1698. IEEE, 2018.

[90] S. Li, X. Sun, and Y. Xu. Particle swarm optimization for route planning of unmanned aerial vehicles. In *Information Acquisition, 2006 IEEE International Conference on*, pages 1213–1218. IEEE, 2006.

[91] T.-H. S. Li, C.-C. Chen, and Y.-T. Su. Optical image stabilizing system using fuzzy sliding-mode controller for digital cameras. *IEEE Transactions on Consumer Electronics*, 58(2):237–245, 2012.

[92] Z. Li, Y. Yan, Y. Jing, and S. Zhao. The design and testing of a lidar platform for a uav for heritage mapping. *The International Archives of Photogrammetry, Remote Sensing and Spatial Information Sciences*, 40(1):17, 2015.

[93] F. T. Lynch and A. Khodadoust. Effects of ice accretions on aircraft aerodynamics. *Progress in Aerospace Sciences*, 37(8):669–767, 2001.

[94] H. Ma and J. Wu. Analysis of positioning errors caused by platform vibration of airborne lidar system. In *Instrumentation and Control Technology (ISICT), 2012 8th IEEE International Symposium on*, pages 257–261. IEEE, 2012.

[95] M. Marwa, S. M. Martin, B. C. Martos, and R. P. Anderson. Analytic and numeric forms for the performance of propeller-powered electric and hybrid aircraft. In *55th AIAA Aerospace Sciences Meeting*. American Institute of Aeronautics and Astronautics, Jan. 2017.

[96] M. Masten. Inertially stabilized platforms for optical imaging systems. *IEEE Control Systems Magazine*, 28(1):47–64, feb 2008.

[97] M. J. Mears. Energy harvesting for unmanned air vehicle systems using dynamic soaring. *50th AIAA Aerospace Sciences Meeting Including the New Horizons Forum and Aerospace Exposition*, January 2012. doi: 10.2514/6.2012-851.

[98] K. Merical, T. Beechner, and P. Yelvington. Hybrid-electric, heavy-fuel propulsion system for small unmanned aircraft. *International Journal of Aerospace*, 7:126–134, 2014. doi: 10.4271/2014-01-2222.

[99] R. Miller, G. Mooty, and J. M. Hilkert. Gimbal system configurations and line-of-sight control techniques for small uav applications. In *Airborne Intelligence, Surveillance, Reconnaissance (ISR) Systems and Applications X*, volume 8713, 2013. doi: 10.1117/12.2015777.

[100] M. Mizui, I. Yamamoto, and R. Ohsawa. Effects of propeller-balance on sensors in small-scale unmanned aerial vehicle. *IOSRJEN*, 2(8):23–27, 2012.

[101] M. Müller, M. Homleid, K.-I. Ivarsson, M. A. Køltzow, M. Lindskog, K. H. Midtbø, U. Andrae, T. Aspelien, L. Berggren, D. Bjørge, et al. AROME-MetCoOp: A nordic convective-scale operational weather prediction model. *Weather and Forecasting*, 32(2):609–627, 2017.

[102] D. R. Nelson, D. B. Barber, T. W. Mclain, and R. W. Beard. Vector field path following for miniature air vehicles. *IEEE Transactions on Robotics*, 23: 519–529, 2007. doi: 10.1109/TRO.2007.898976.

[103] N. Nigam. The multiple unmanned air vehicle persistent surveillance problem: A review. *Machines*, 2(1):13–72, 2014.

[104] I. K. Nikolos, K. P. Valavanis, N. C. Tsourveloudis, and A. N. Kostaras. Evolutionary algorithm based offline/online path planner for UAV navigation. *IEEE Transactions on Systems, Man, and Cybernetics, Part B (Cybernetics)*, 33(6):898–912, 2003.

[105] N. Omar, M. Daowd, P. van der Bossche, and O. Hegazy. Rechargeable energy storage systems for plug-in hybrid electric vehicles—assessment of electrical characteristics. *Energies*, 5:2952–2988, 2012. doi: 10.3390/en5082952.

[106] I. C. A. Organization. *Manual of the ICAO Standard Atmosphere: Extended to 80 Kilometres (262 500 Feet)*, volume 7488. International Civil Aviation Organization, 1993.

[107] D. Palma, A. Zolich, Y. Jiang, and T. A. Johansen. Unmanned aerial vehicles as data mules: An experimental assessment. *IEEE Access*, 2017.

[108] J. Pinto, P. S. Dias, R. Martins, J. Fortuna, E. Marques, and J. Sousa. The LSTS toolchain for networked vehicle systems. In *2013 MTS/IEEE OCEANS-Bergen*, pages 1–9. IEEE, 2013.

[109] I. Prodan, S. Olaru, R. Bencatel, J. B. de Sousa, C. Stoica, and S.-I. Niculescu. Receding horizon flight control for trajectory tracking of autonomous aerial vehicles. *Control Engineering Practice*, 21(10):1334–1349, 2013.

[110] D. Raymer. *Aircraft Design: A Conceptual Approach 5e and RDSWin STUDENT*. American Institute of Aeronautics and Astronautics, Inc., 2012.

[111] K. Reddy, H. Lokesha, and S. Akhila. Video stabilization for micro air vehicles. *International Journal of Advanced Research in Computer and Communication Engineering*, 4(4):442–445, 2015.

[112] A. Richards and J. P. How. Aircraft trajectory planning with collision avoidance using mixed integer linear programming. In *American Control Conference, 2002. Proceedings of the 2002*, volume 3, pages 1936–1941. IEEE, 2002.

[113] V. Roberge, M. Tarbouchi, and G. Labonté. Comparison of parallel genetic algorithm and particle swarm optimization for real-time UAV path planning. *IEEE Transactions on Industrial Informatics*, 9(1):132–141, 2013.

[114] C. D. Rodin, F. A. A. Andrade, A. R. Hovenburg, T. A. Johansen, and R. Storvold. A survey of design considerations of optical imaging stabilization systems for small unmanned aerial systems. Submitted for publication.

[115] C. D. Rodin, L. N. de Lima, F. A. de Alcantara Andrade, D. B. Haddad, T. A. Johansen, and R. Storvold. Object classification in thermal images using convolutional neural networks for search and rescue missions with unmanned aerial systems. In *2018 International Joint Conference on Neural Networks (IJCNN)*, pages 1–8. IEEE, 2018.

[116] J. Roskam and C. Lan. *Airplane Aerodynamics and Performance*. Design, Analysis and Research Corporation, 1997. ISBN 1-884885-44-6.

[117] A. Rucco, A. P. Aguiar, F. L. Pereira, and J. B. de Sousa. A predictive path-following approach for fixed-wing unmanned aerial vehicles in presence of wind disturbances. In *Robot 2015: Second Iberian Robotics Conference*, pages 623–634. Springer, 2016.

[118] Y. G. Ryu, H. C. Roh, S. J. Kim, K. H. An, and M. J. Chung. Digital image stabilization for humanoid eyes inspired by human vor system. In *IEEE International Conference on Robotics and Biomimetics (ROBIO)*, pages 2301–2306, Dec 2009. doi: 10.1109/ROBIO.2009.5420460.

[119] D. T. Sandwell. Biharmonic spline interpolation of GEOS-3 and SEASAT altimeter data. *Geophysical Research Letters*, 14(2):139–142, 1987. ISSN 1944-8007. doi: 10.1029/GL014i002p00139.

[120] A. Seitz, O. Schmitz, A. Isikveren, and M. Hornung. Electrically powered propulsion: Comparison and contrast to gas turbines. In *Deutscher Luft- und Raumfahrtkongress 2012*, 2012.

[121] R. Sengupta, J. Connors, B. Kehoe, Z. Kim, T. Kuhn, and W. Jared. Final report - autonomous search and rescue with scaneagle, 2010.

[122] H. Shen, Q. Pan, Y. Cheng, and Y. Yu. Fast video stabilization algorithm for uav. In *IEEE International Conference on Intelligent Computing and Intelligent Systems*, volume 4, pages 542–546, Nov 2009. doi: 10.1109/ICICISYS.2009.5357609.

[123] X. Shen, H. Liu, X.-B. Cheng, C. Yan, and J.-Q. Huang. Beyond lithium ion batteries: Higher energy density battery systems based on lithium metal anodes. In *Energy Storage Materials*, pages 161–175, 2018.

[124] R. Siquig. Impact of icing on unmanned aerial vehicle (uav) operations. Technical report, NAVAL ENVIRONMENTAL PREDICTION RESEARCH FACILITY MONTEREY CA, 1990.

[125] E. Skjong and S. Nundal. Tracking objects with fixed-wing uav using model predictive control and machine vision. Master's thesis, Norwegian University of Science and Technology (NTNU), 09 2014.

[126] E. Skjong, S. A. Nundal, F. S. Leira, and T. A. Johansen. Autonomous search and tracking of objects using model predictive control of unmanned aerial vehicle and gimbal: Hardware-in-the-loop simulation of payload and avionics. In *2015 International Conference on Unmanned Aircraft Systems (ICUAS)*, pages 904–913. IEEE, 2015.

[127] K. L. Sørensen. Autonomous icing protection solution for small unmanned aircraft: An icing detection, anti-icing and de-icing solution. 2016.

[128] K. L. Sørensen, M. Blanke, and T. A. Johansen. Diagnosis of wing icing through lift and drag coefficient change detection for small unmanned aircraft. In *International Federation of Automatic Control*, 2015.

[129] K. Szilder and S. McIlwain. In-flight icing of uavs-the influence of reynolds number on the ice accretion process. Technical report, SAE Technical Paper, 2011.

[130] K. Szilder and W. Yuan. The influence of ice accretion on the aerodynamic performance of a uas airfoil. In *53rd AIAA Aerospace Sciences Meeting*, page 0536, 2015.

[131] A. Team. Ardupilot. ardupilot.org, 2019. [Online; accessed 10-July-2019].

[132] M. Team. MAVLink micro air vehicle protocol. mavlink.io/en, 2019. [Online; accessed 10-July-2019].

[133] R. Thillainayagi and K. S. Kumar. Video stabilization technique for thermal infrared aerial surveillance. In *2016 Online International Conference on*

Green Engineering and Technologies (IC-GET), pages 1–6, Nov 2016. doi: 10.1109/GET.2016.7916630.

[134] G. Thompson, B. E. Nygaard, L. Makkonen, and S. Dierer. Using the weather research and forecasting (WRF) model to predict ground/structural icing. In *13th International Workshop on Atmospheric Icing on Structures, METEOTEST, Andermatt, Switzerland*, 2009.

[135] M. Tico. *Digital Image Stabilization*, chapter 1, pages 1 – 14. 11 2009. ISBN 978-953-307-002-5. doi: 10.5772/7458.

[136] L. Traub. Range and endurance estimates for battery-powered aircraft. *Journal of Aircraft*, pages 703–707, 2011. ISSN 0021-8669. doi: 10.2514/1.C031027.

[137] L. Traub. Optimal battery weight fraction for maximum aircraft range and endurance. *Journal of Aircraft*, 53(4):3–5, 2016. doi: 10.2514/1.C033416.

[138] O. Tremblay, L.-A. Dessaint, and A.-I. Dekkiche. A generic battery model for the dynamic simulation of hybrid electric vehicles. In *2007 IEEE Vehicle Power and Propulsion Conference*, pages 284–289. Ieee, 2007.

[139] P. Trodden and A. Richards. Multi-vehicle cooperative search using distributed model predictive control. In *AIAA Guidance, Navigation and Control Conference and Exhibit*, page 7138, 2008.

[140] B. Uragun and I. N. Tansel. The noise reduction techniques for unmanned air vehicles. In *Unmanned Aircraft Systems (ICUAS), 2014 International Conference on*, pages 800–807. IEEE, 2014.

[141] K. P. Valavanis and G. Vachtsevanos. *Handbook of unmanned aerial vehicles*. Springer Science+Business Media, 2011. ISBN 9789048197071. doi: 10.1007/978-90-481-9707-1.

[142] A. Valenzuela and D. Rivas. Analysis of wind-shear effects on optimal aircraft cruise. *Journal of Guidance, Control and Dynamics*, 39(9):2148–2155, 9 2016. ISSN 0731-5090. doi: 10.2514/1.G000251.

[143] B. van Dijk. Notes of prestatieleer. `intra.techniek.hva.nl/avi/`, 2014.

[144] J. Verbeke and S. Debruyne. Vibration analysis of a uav multirotor frame. In *Proceedings of ISMA 2016 International Conference on Noise and Vibration Engineering*, pages 2401–2409, 2016.

[145] F. Veroustraete. The rise of the drones in agriculture. In *EC Agriculture 2.2*, pages 325–327, 2015.

[146] D. Wei, N. Junxiang, W. Miao, Z. Jishun, Y. Yanan, and L. Yuanyuan. An analysis model of helicopter and uav in overhead powerline inspection. In *2018 International Conference on Civil and Hydraulic Engineering*, 2018.

[147] L. A. Weitz. *Derivation of a Point-Mass Aircraft Model used for Fast-Time Simulation*. MITRE Corporation, 2015.

[148] E. Whalen, A. Broeren, M. Bragg, and S. Lee. Characteristics of runback ice accretions on airfoils and their aerodynamics effects. In *43rd AIAA Aerospace Sciences Meeting and Exhibit*, page 1065, 2005.

[149] A. Winter, R. Hann, A. Wenz, K. Grytte, and T. A. Johansen. Stability of a flying wing uav in icing conditions. In *Stability of a Flying Wing UAV in Icing Conditionsl*, 2019.

[150] W. Wright. User's manual for lewice version 3.2. 2008.

[151] W. Wright and A. Rutkowski. Validation results for lewice 2.0" and cd-rom, 1999.

[152] D. Wulich and N. Kopeika. Image resolution limits resulting from mechanical vibrations. *Optical engineering*, 26(6):266529, 1987.

[153] K. Yang and S. Sukkarieh. 3D smooth path planning for a UAV in cluttered natural environments. In *Intelligent Robots and Systems, 2008. IROS 2008. IEEE/RSJ International Conference on*, pages 794–800. IEEE, 2008.

[154] T. Yechout. *Introduction to Aircraft Flight Mechanics*. American Institute of Aeronautics and Astronautics, Inc., 2014.

[155] D. Yeom. Optical image stabilizer for digital photographing apparatus. *IEEE Transactions on Consumer Electronics*, 55(3), 2009.

[156] Z. Zhenming Li, M. Lao, S. K. Phang, M. R. A. Hamid, K. Z. Tang, and F. Lin. Development and Design Methodology of an Anti-Vibration System on Micro-UAVs. In *International Micro Air Vehicle Conference and Flight Competition (IMAV)*, Toulouse, 2017.

[157] A. Zolich, A. Sœgrov, E. Vågsholm, V. Hovstein, and T. A. Johansen. Coordinated maritime missions of unmanned vehicles—network architecture and performance analysis. In *Communications (ICC), 2017 IEEE International Conference on*, pages 1–7. IEEE, 2017.

ISBN 978-82-326-4548-0 (printed version)
ISBN 978-82-326-4549-7 (electronic version)
ISSN 1503-8181

Doctoral theses at NTNU, 2020:98

Anthony Reinier Hovenburg

Flight Performance Optimization for Small Unmanned Aerial Vehicles Using Path Planning Methods

NTNU
Norwegian University of
Science and Technology
Faculty of Information Technology
and Electrical Engineering
Department of Engineering Cybernetics

NTNU
Norwegian University of
Science and Technology

Doctoral Thesis
Anthony Reinier Hovenburg
Doctoral theses at NTNU, 2020:98
NTNU